HOKKAIDO UNIVERSITY

Title	Analog Quantum Computation and Communication with Digitized Continuous Variables
Author(s)	福井, 浩介
Degree Grantor	北海道大学
Degree Name	博士(工学)
Dissertation Number	甲第13299号
Issue Date	2018-09-25
DOI	https://doi.org/10.14943/doctoral.k13299
Doc URL	https://hdl.handle.net/2115/90468
Type	doctoral thesis
File Information	Kosuke_Fukui.pdf

Analog Quantum Computation
and Communication
with Digitized Continuous Variables

Kosuke Fukui

Hokkaido University

August 2018

Acknowledgements

First and foremost, I would like to thank my PhD supervisor Akihisa Tomita. He has continually provided a valuable guidance and wonderful opportunities to participate in domestic and international conferences in my doctoral course in the Laboratory of Optical Processing and Networking.

I would like to thank Atsushi Okamoto for helpful comments and advices regarding this thesis. I would like to thank Kazuhisa Ogawa and Fumiaki Matsuoka for having insightful discussions in the course of this work. I also wish to thank to all members in laboratory for providing me nice environment for my Ph.D research.

I would like to deeply thank Keisuke Fujii who introduces me to the numerical techniques needed for a part of main results and encourages me to advance my research. I am very grateful to reseaech collabortors Raf Alexander, Shuntaro Takeda, and Akira Furusawa. I also thank Nick Menicucci and Peter van Loock for making time to collaborate.

Finally, I would like to express my gratitude to my parent for constant support.

Contents

Chapter 1

Introduction

Big data analytics is valuable for text analytics, machine learning, predictive analytics, data mining, statistics, businesses, and so on. Nowadays size of world's data in is growing exponentially. The exploding volume of data growth has led to several challenges: data center power, cooling, storage, data movement, and management complexity, and so on. Quantum computation is an attractive tool to perform faster processing speed for big data analytics, since quantum computation has been shown to solve efficiently some hard problems for conventional computers.

For the conventional (classical) computers, the computer memory to simulate the physical systems is required exponentially in proportion to the increasing dimension of the state space with the size of the physical systems. Accordingly, a simulation of the physical systems is generally inefficient using the conventional computers. In 1982, Richard Feynman came up with the idea of a quantum computer that bring out the advantage of quantum mechanics, which can simulate quantum systems efficiently. In 1985, David Deutsch proposed the quantum Turing machine. In the quantum Turing machine, a "*qubit*", which can hold a quantum superposition of 0 and 1, enable us to encode many inputs to a logic circuit simultaneously, and then it can make calculations on all the inputs at the same time. In 1994, Peter Shor showed that his proposed algorithm for integer factorization can be performed exponentially less operations than the most efficient known algorithm[1]. Shor's algorithm, processing on a quantum computer, can factorize even integers of orders exceeding 1000 used for RSA-encryption in reasonable time. In 1996, Grover proposed a database search algorithm to perform a polynomial speedup over the best classical algorithm. In Grover's algorithm, amplitude amplification of the intended quantum state is employed, which is an important techique in quatum algorithm [2].

Today, in several candidates for a element of quantum computer, the accuracy of quantum gates have made progress toward a goal of the threshold value required by large scale quantum computation. For example, in the superconducting and trapped-ion qubit, the error probability of a two-qubit gate has been less than 1%. However, these prototype

systems of quantum computer are small; none of them contain as many as 20 qubits, since cracking RSA Encrypt that requires a 100-million-qubit system can not be achievable in presence technology. Nonetheless, quantum computer composed of small number of qubits can reach so-called "quantum supremacy"; that is, quantum computing can outperform classical computing by quantum computer expected to arrive around the much more modest 50-100 qubits. In 2017, major corporation such as IBM and Google claim that they will perform quantum supremacy within years.

Unlike quantum supremacy, a large-scale quantum circuit that requires scalable entangled states is still a significant experimental challenge for most candidates of qubits. In quantum computation with the continuous variables, squeezed vacuum states with the optical setting have shown great potential to generate scalable entangled states because the entanglement is generated by only beam splitter coupling between two squeezed vacuum states [3]. However, scalable computation with squeezed vacuum states has been shown to be difficult to achieve because of the accumulation of errors during the quantum computation process, even though the states are created with perfect experimental apparatus [4]. Therefore, fault-tolerant protection from noise is required that uses the quantum error correcting code. Because noise accumulation originates from the "continuous" nature of the continuous variable, it can be circumvented by encoding continuous variables into digitized variables using an appropriate code, such as Gottesman–Kitaev–Preskill (GKP) code [5], which are referred to as GKP qubits. In 2014, Menicucci showed that fault-tolerant quantum computation (FTQC) with continuous variables is possible within the framework of measurement-based quantum computation using squeezed vacuum states with GKP qubits [4]. Moreover, GKP qubits keep the advantage of squeezed vacuum states on optical implementation that they can be entangled by only BS coupling. Hence, GKP qubits offer a promising element for the implementation of FTQC with continuous variables.

To be practical, the squeezing level required for large scale quantum computation should be experimentally achievable. Unfortunately, the required squeezing level is still high. Thus, another twist is necessary to reduce the required squeezing level. It is analog information contained in the GKP qubit that has been overlooked. The effect of noise on continuous variable states is observed as a deviation in an analog measurement outcome, which includes beneficial information for quantum error correction. Despite this, the analog information from the GKP qubit has been wasted because the GKP qubit has

2

been treated as only a discrete variable qubit, for which the measurement outcomes are described by bits, when we identify the bit value. Harnessing the wasted information for the QEC will improve the error tolerance compared with using the conventional method based on only bit information.

In this thesis, toward large scale quantum computation with the GKP qubtis, we propose the analog quantum error correction and high-threshold fault-tolerant quantum computation, where the analog quantum error correction is applied to the surface code and the resource state for quantum computation is constructed with a low error accumulation with the help of analog information. In addition to the implementation of large-scale quantum computation, the GKP qubits will be recognized as an important technological element to implement quantum communication with continuous variables. We also present several novel methods that offer the way of secure and high-fidelity quantum computation and quantum communication. Hence, our works will pave the way for constructing a practical quantum computations and communication with continuous variables.

In this thesis based on the works in Refs. [6, 7, 8] and the works in preparation. The outline of this thesis is as follows:

Chapter 2

In chapter 2 we review quantum computation based on discrete variables, continuous variables, and digitized continuous variable states including the GKP qubit. This comparison between discrete variables and digitized variables is aid to understand the key concepts of quantum system of continuous variables. Our introduction to digitized continuous variables concludes with the threshold of the squeezing level of the GKP qubits for large-scale quantum computation based on the measurement-based quantum computation, and necessity of reducing this threshold required. We give a method to alleviate this requirement in later chapters.

Chapter 3

Chapter 3 is devoted to a analog quantum error correction. The analog information obtained by measuring continuous variable states (including GKP qubits) reflects the effect of noise as a deviation in the measurement outcome. Therefore, it contains beneficial information to improve the error tolerance. We propose a method to use analog information

for quantum error correction to improve the quantum error correction performance. Then, we apply the method to various quantum error correcting codes, such as the three-qubit bit-flip code, the Knill's C_4/C_6 code, and the surface code. We numerically investigate validity of analog quantum error correction for the C_4/C_6 code and the surface code against the Gaussian quantum channel with ideal syndrome measurements, and show that the analog quantum error correction achieves close to the lower bound of the quantum capacity of the Gaussian quantum channel. This implies that the analog quantum error correction with the C_4/C_6 code and the surface code provides an optimal performance against Gaussian quantum channel.

Chapter 4

In Chapter 4, we present a method to implement large-scale quantum computation with the GKP qubit harnessing analog information. The proposed high-threshold fault-tolerant quantum computation consists of two parts. One is to apply analog quantum error correction [6] to the surface code under realistic error conditions, which allows us to implement the high-threshold fault-tolerant quantum computation. The other is a construction of the cluster state for topologically protected measurement-based quantum computation [9, 10, 11, 12] with a low error accumulation by using the highly-reliable measurement with the help of analog information. We numerically show that the required squeezing level for topologically protected measurement-based quantum computation with the 3D cluster state constructed by our method can be reduced to 9.8 dB. By achieving the requirement of the squeezing level around 10 dB, the proposed method can considerably take a step closer to the realization of large-scale quantum computation with digitized continuous variables and will be indispensable to construct fault-tolerant quantum computation with continuous variables.

Chapter 5

This chapter describes the tracking quantum error correction to reduce the number of qubits required for the quantum error correction during large scale quantum computation, where the logical-qubit level quantum error correction is partially substituted for the single-qubit level quantum error correction. The numerical results shows that the tracking quantum error correction with analog quantum error correction is effective way to reduce

the required number of the qubits, since the tracking quantum error correction with analog quantum error correction can reduce the number of physical qubits required. To the best of our knowledge, this approach is the first practical attempt to utilize both the single- and logical standard qubit quantum error corrections to alleviate the requirement of the number of qubits. Hence, the proposed method has a great advantage in using fault-tolerant quantum computation with continuous variables and will open a new way to practical quantum computers.

Chapter 6

In this chapter, we propose the entanglement distillation protocol with the GKP qubit using analog information to improve the entanglement distillation performance. In the proposed method, the highly-reliable measurement is applied to the conventional entanglement distillation protocol. To provide an insight into our method, we apply the highly-reliable measurement to a quantum privacy amplification protocol with the ideal and approximate GKP qubit.

Chapter 7

In chapter 7, we present a method to implement a long-distance quantum communication with GKP qubits. In this chapter, we propose the method to implement resource-efficient quantum repeater protocol using analog information contained in the GKP qubit. In the proposed method, we apply the highly-reliable measurement using GKP qubits to "all photonic quantum repeater protocol" based on photon qubits to enhance tolerance against photon loss. Numerical results show that our method can achieve the comparative performance with the conventional method based on photon qubits. Furthermore, our method can reduce the number of the GKP qubits required for quantum communication by several orders of magnitude less than the conventional method.

Chapter 8

Chapter 8 is devoted to summary and conclusions.

Chapter 2

Quantum computation with digitized continuous variables

In this chapter, we review the quantum computation with continuous variable states. Quantum computation with the discrete variables, continuous variables, and digitized continuous variables are described to make it easy to compare them. In the end of this chapter, we will introduce a way of calculation of the squeezing level required for fault-tolerant quantum computation.

2.1 Quantum computation with the discrete variable states

2.1.1 Qubit

In quantum information processing, the information of a binary bit value is described by a quantum bit, which is so-called qubit. Qubit is quantum counterpart of a classical bit that takes a bit value 0 or 1. The obvious difference between a qubit and a classical bit is that qubit can exist in a superposition of states of a bit. This can be attributed to the parallelism of computation, since qubits can exist in a superposition of 0 and 1 states. Consequently, n-qubits can store all the 2^n states in a quantum register at the same time. In general, the state of the qubit $|\psi\rangle$ is described by

$$|\psi\rangle = \alpha |0\rangle + \beta |1\rangle, \tag{2.1}$$

where α and β are an arbitrary complex value, and satisfy the condition, $|\alpha|^2 + |\beta|^2 = 1$. The states of the qubits $|0\rangle$ and $|1\rangle$ can be defined by the standard basis as

$$|0\rangle = \begin{pmatrix} 1 \\ 0 \end{pmatrix}, \quad |1\rangle = \begin{pmatrix} 0 \\ 1 \end{pmatrix}, \tag{2.2}$$

respectively. Examples of candidates of a qubit for the two level quantum systems include the polarization of a photon, trapped ion, superconducting exhibiting quantized states of electronic charge, magnetic flux, or Josephson junction phase, and so on.

2.1.2 Quantum gate

Quantum gate and Pauli matrices

Like classical logic gates for a circuit of a classical computer, a quantum circuit is composed of the quantum gates.

The Pauli matrices form a basis of unitary operators and are defined in the standard basis by

$$I = \begin{pmatrix} 1 & 0 \\ 0 & 1 \end{pmatrix}, \quad X = \begin{pmatrix} 0 & 1 \\ 1 & 0 \end{pmatrix}, \quad Y = \begin{pmatrix} 0 & -i \\ i & 0 \end{pmatrix}, \quad Z = \begin{pmatrix} 1 & 0 \\ 0 & -1 \end{pmatrix}, \quad (2.3)$$

where X, Y, and Z are also described as $X = \sigma x = \sigma_1$, $Y = \sigma y = \sigma_2$, and $Z = \sigma z = \sigma_3$, respectively. The Pauli matrices act on a qubit as

$$X|0\rangle = |1\rangle, \quad X|1\rangle = |0\rangle, \quad Z|0\rangle = |0\rangle, \quad Z|1\rangle = -|1\rangle, \quad (2.4)$$

respectively. Therefore, X and Z operators are interpreted as a bit and phase operators, respectively. Also, Y operator satisfy $Y = iXZ$. The Pauli group P consists of tensor products of Pauli operators and the Pauli group on n-qubits is described as

$$P = \{1, i, -1, -i\} \times \{I, X, Y, Z\}^{\otimes n}. \quad (2.5)$$

The Hadamard gate H, the $\frac{\pi}{4}$ rotation about the Z axis T, and the phase gate P that is the $\frac{\pi}{2}$ rotation about the Z axis are given by

$$H = \frac{1}{\sqrt{2}} \begin{pmatrix} 1 & 1 \\ 1 & -1 \end{pmatrix}, \quad P = \begin{pmatrix} 1 & 0 \\ 0 & i \end{pmatrix}, \quad T = \begin{pmatrix} 1 & 0 \\ 0 & e^{i\pi/4} \end{pmatrix}, \quad (2.6)$$

where T is also known as the $\frac{\pi}{8}$ gate.

Universal set

The gate set U_C, $\{X, Y, Z, H, S\}$, are normalizers of the Pauli group, which generate a group of single-qubit Clifford operations as $U_C \sigma_i U_C^\dagger$. To generate arbitrary single-qubit unitary operations, a non-Clifford operation such as T gate is required. Then, to generate arbitrary n-qubit unitary operations, two-qubit gate is inevitable. The controlled-Not

(CNOT) gate and the controlled-Z (CZ) gate are well known as a two-qubit gate and defined as

$$U_{\text{CNOT}} = \begin{pmatrix} 1 & 0 & 0 & 0 \\ 0 & 1 & 0 & 0 \\ 0 & 0 & 0 & 1 \\ 0 & 0 & 1 & 0 \end{pmatrix}, \quad U_{\text{CZ}} = \begin{pmatrix} 1 & 0 & 0 & 0 \\ 0 & 1 & 0 & 0 \\ 0 & 0 & 1 & 0 \\ 0 & 0 & 0 & -1 \end{pmatrix}. \tag{2.7}$$

The CNOT gate and CZ gate are acted on the controlled qubit c and the target qubit t as

$$U_{\text{CNOT}} = |0\rangle\langle 0|_c \otimes I_t + |1\rangle\langle 1|_c \otimes X_t, \quad U_{\text{CZ}} = |0\rangle\langle 0|_c \otimes I_t + |1\rangle\langle 1|_c \otimes Z_t, \tag{2.8}$$

respectively. In Eq. (2.8) a symbol $\otimes$ is called the tensor product that represents in n-quantum systems, e.g.

$$H \otimes I = \frac{1}{\sqrt{2}} \begin{pmatrix} 1 & 0 & 1 & 0 \\ 0 & 1 & 0 & 1 \\ 1 & 0 & -1 & 0 \\ 0 & 1 & 0 & -1 \end{pmatrix}, \tag{2.9}$$

$$U_{\text{CNOT}} \cdot X \otimes I = \begin{pmatrix} 0 & 0 & 1 & 0 \\ 0 & 1 & 0 & 1 \\ 0 & 1 & 0 & 0 \\ 1 & 0 & 0 & 0 \end{pmatrix} = X \otimes X \cdot U_{\text{CNOT}}. \tag{2.10}$$

Since the gate set $\{H, P, T, U_{\text{CNOT}}\}$ or $\{H, P, T, U_{\text{CZ}}\}$ can construct any unitary operation, these gate set is called a universal set.

Quantum noise

To describe the quantum noise, we consider an data qubit system D and external (environmental) system E. Quantum noise can be modeled as interaction between the systems D and E. The joint state of systems D and E is given by

$$\rho_D \otimes \rho_E \tag{2.11}$$

The quantum noise transform $\rho_D \otimes \rho_E$ as

$$U(\rho_D \otimes \rho_E)U^\dagger \tag{2.12}$$

Since the environmental system after the noise will be needed to be accessible, the data qubit system can be obtained by the partial trace of Eq. (2.12) as

$$\mathscr{E}(\rho_D) = \mathrm{tr}_E\left[U(\rho_D \otimes \rho_E)U^\dagger\right], \tag{2.13}$$

where $\mathscr{E}$ is superoperator (trace-preserving completely positive map) acting on a density operator ρ_D. This operation of the quantum noise $\mathscr{E}(\rho_D)$ can be also described by

$$\mathscr{E}(\rho_D) = \sum_k E_k \rho_D E_k^\dagger, \tag{2.14}$$

where the operation elements E_k satisfy $\sum_k E_k E_k^\dagger = I$. In the case of the depolarizing channel acting on qubits, the channel in the high temperature limit can be described by stochastic Pauli errors with probabilities p_i as

$$\mathscr{E}(\rho_D) = \left[1 - p_1 - p_2 - p_3\right]\rho + \sum_3 p_i \sigma_i \rho_D \sigma_i, \tag{2.15}$$

where $\sigma_1 = X$, $\sigma_2 = Y$, and $\sigma_3 = Z$ are Pauli matrices.

2.1.3 Entangled states and stabilizer

Bell state and GHZ state

An entangled states refer to a quantum state which cannot be decomposed into two independent subsystems. The Bell state, $|\mathrm{Bell}\rangle$, and GHZ state, $|\mathrm{GHZ}\rangle$, are typical examples of entangled states in two- and three-qubit system:

$$|\mathrm{Bell}\rangle = \frac{1}{\sqrt{2}}\left(|0\rangle_A |0\rangle_B + |1\rangle_A |1\rangle_B\right), \tag{2.16}$$

$$|\mathrm{GHZ}\rangle = \frac{1}{\sqrt{3}}\left(|0\rangle_A |0\rangle_B |0\rangle_C + |1\rangle_A |1\rangle_B |1\rangle_C\right), \tag{2.17}$$

respectively. These entangled states cannot be decomposed by a tensor product of a state in the subsystem and another state in the subsystem. The Bell state and GHZ state are depicted in Fig. 2.1 (a) and (b), respectively.

Cluster state

(a)　　　　　(b)　　　　　(c)

············· CNOT gate　　　　── CZ gate
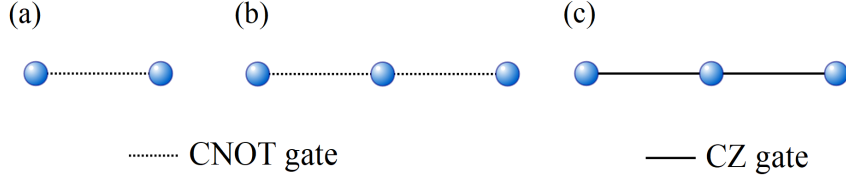
Figure 2.1: Entangled states. (a) Bell state (b) GHZ state (c) Cluster state

The cluster state is used for measurement-based quantum computation (or one-way quantum computation), which is generated as follows. Firstly, we prepare the a qubit composed of graph G in the state $|+\rangle = (|0\rangle + |1\rangle)/\sqrt{\pi}$. Next, we perform the CZ gate between the two qubits corresponding to every edge E. For example, the 3-linear cluster state $|3l\rangle$ and 4-tree cluster state $|4t\rangle$ described in Fig. 2.1 (c) are written as

$$
\begin{aligned}
|3l\rangle &= (|+\rangle_1 |0\rangle_2 |+\rangle_3 + |-\rangle_1 |1\rangle_2 |-\rangle_3)/\sqrt{2}, & (2.18)\\
|4t\rangle &= \{|+\rangle_1 (|0\rangle_2 |0\rangle_3 |0\rangle_4 + |1\rangle_2 |1\rangle_3 |0\rangle_4 + |1\rangle_2 |0\rangle_3 |1\rangle_4 + |0\rangle_2 |1\rangle_3 |1\rangle_4) \\
&\quad + |-\rangle_1 (|0\rangle_2 |0\rangle_3 |1\rangle_4 + |0\rangle_2 |1\rangle_3 |0\rangle_4 + |1\rangle_2 |0\rangle_3 |0\rangle_4 + |1\rangle_2 |1\rangle_3 |1\rangle_4)\}/2\sqrt{2}, & (2.19)
\end{aligned}
$$

respectively.

Stabilizer

The stabilizer formalism [13, 14] offers a elegant way to represent any graph state. For a n-qubit $|\psi\rangle$ is stabilized by

$$
S|\psi\rangle = |\psi\rangle \qquad \text{for all} \quad S \in \mathscr{S}, \tag{2.20}
$$

where $\mathscr{S}$ represents a stabilizer group. For the Bell state and GHZ state, the stabilizer groups are given by

$$
\begin{aligned}
S_{\text{Bell}} &= \langle X \otimes X, Z \otimes Z \rangle, & (2.21)\\
S_{\text{GHZ}} &= \langle X \otimes X \otimes X, Z \otimes Z \otimes I, I \otimes Z \otimes Z \rangle, & (2.22)
\end{aligned}
$$

The cluster states associated to a graph $G = (V, E)$, where G consists of a vertex set

$V = \{v_i\}_{i=1}^n$ and a set of edges E, is *stabilized* by operators K_j as

$$K_i = X_i \prod_{j \in N_i} Z_j, \qquad (2.23)$$

where the Pauli operators X_i and Z_j act on the qubits associated to the vertices i and j, respectively, and N_i denotes the set of indices defined as the set of vertices neighboring v_i. For the 4-tree cluster state $|4t\rangle$ in Eq. (2.19), the qubit 1 corresponds to the vertice i.

2.1.4 Measurement-based quantum computation with discrete variable states

Measurement-based quantum computation is an alternative to the standard quantum circuit model. In measurement-based quantum computation, quantum computation is implemented by single-qubit measurements on a large-scale cluster state. Since the resource state to implement quantum computation is prepared in off-line processing, there is no need to generate the on-demand entangled state during quantum computation. In Fig. 2.2(a), the schematic view of measurement-based quantum computation for single-qubit gates is described with the two qubit state $U_{CZ} \cdot |\psi\rangle |+\rangle$. In particular, we consider the gate defined by

$$M_{\theta,m} = X^m H Z_\theta \qquad (m = 0,1), \qquad (2.24)$$

where $M_{\theta = n\pi/2,m}$ and $M_{\theta = n\pi/4,m}$ are used to implement the gates for the single-qubit Clifford group and universal for single-qubit quantum computation, respectively. In Fig. 2.2 (a), the data qubit 1 is measured in the basis X and the qubit 2 transform into $X^m H |\psi\rangle$, where m denotes the measurement outcome, 0 or 1. In the case of the gate $M_{\theta \neq 0,m}$, the qubit 1 is measured in the basis $Z_\theta^\dagger X Z_\theta$, and the qubit 2 transform into $X^m H Z_\theta |\psi\rangle$, where the Z_θ is the single qubit rotation regarding to Z axis. By repeatedly performing this procedure, we can implement a sequence of single qubit rotations

$$M_{\theta_n,m_n} M_{\theta_{n-1},m_{n-1}} \cdots M_{\theta_1,m_0}. \qquad (2.25)$$
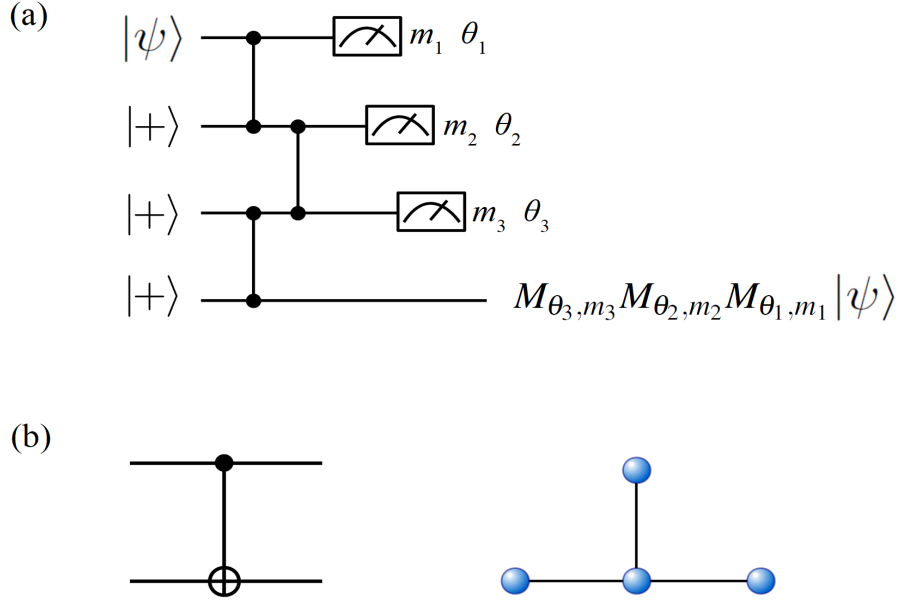
Figure 2.2: Introduction of measurement-based quantum computation.

In the case of $n = 3$ in Fig. 2.2(a), the gate $M_{\theta_3, m_3} M_{\theta_2, m_2} M_{\theta_1, m_1}$ can transform as

$$M_{\theta_3, m_3} M_{\theta_2, m_2} M_{\theta_1, m_1} = M_{(-1)^{m_3}\theta_3, 0} M_{(-1)^{m_2}\theta_2, 0} M_{(-1)^{m_1}\theta_1, 0}. \tag{2.26}$$

by using a commutation relation $X Z_\theta X = Z_{(-\theta)}$. Two qubit gate is also performed by measurement based quantum computation model as shown in Fig. 2.2 (b). The CNOT gate based on a circuit model in Fig. 2.2 (b) to the left is equal to the sequence of the measurement in Fig. 2.2 (b) to the right. Therefore, the cluster states enable universal quantum computation, since cluster states realize the measurement based implementation of a single (for Clifford and universal) and two qubit gate.

2.1.5 Quantum error correcting codes

Three-qubit bit flip code

We describe the simplest quantum error correcting code, the three-qubit bit flip code. The three-qubit bit flip code has generators

$$S_1 = Z \otimes Z \otimes I, \quad S_2 = I \otimes Z \otimes Z. \tag{2.27}$$

The stabilizer subspace is spanned by the logical states

$$|0\rangle_{\rm L} = |000\rangle, \quad |1\rangle_{\rm L} = |111\rangle. \tag{2.28}$$

The logical operator for X is given by

$$X_L = X \otimes X \otimes X, \tag{2.29}$$

acting on the logical states as $X_L|0\rangle_{\rm L} = |1\rangle_{\rm L}$ and $X_L|1\rangle_{\rm L} = |0\rangle_{\rm L}$. This quantum error correcting code is a quantum analogue of the classical there-bit repetition code, and can correct the single bit flip error X with the probability p on the qubit i described by super-operator as

$$\mathcal{E}\rho = (1-p)\rho + pX_i\rho X_i. \tag{2.30}$$

In quantum error correction (QEC), it is necessary that the measurements on the logical qubit to determine the location of errors are performed indirectly on the code state, to avoid destructing the superposition of quantum states. To avoid the destruction of quantum information of the logical qubit, by using ancilla qubits, we need to determine the location of errors without measurement of the logical qubit. For the three-qubit flip code, the circuit, two ancilla qubits are initialized to the state $|0\rangle$, interacted with the data qubit through the CNOT gate, and measured in the computational (Z) basis. From the measurement outcomes, the syndrome to determine the location of the single X error is extracted. To see the way of the QEC, we consider that the logical state $|\psi\rangle$ is $|b_1b_2b_3\rangle$ ($b_1 = b_2 = b_3 = 0$ or 1), and the measurement outcomes of the two ancilla qubits are x and y, respectively. Since the X error occurs on the three qubit as

$$|\psi\rangle = X^{l_1} \otimes X^{l_2} \otimes X^{l_3}(\alpha|000\rangle + \beta|111\rangle), \tag{2.31}$$

measurement outcomes x and y are equal to $l_1 + l_2$ and $l_1 + l_3$, respectively. In the case of no error, both x and y are 0. On the other hand, the $x = 0$ and $y = 1$ shows the single X error on the qubit 3. Therefore, we can determine the location of the X error.

Steane 7-qubit code

The class of quantum error correcting codes, so-called the Calderbank-Shor-Steane (CSS) codes, are particularly well suited for use in quantum computation, since these codes are an important element to make quantum computation *fault-tolerant*. The Steane 7-qubit code is the smallest CSS code and has the stabilizer generators

$$
\begin{aligned}
S_1 &= I \otimes I \otimes I \otimes X \otimes X \otimes X \otimes X, & S_2 &= I \otimes X \otimes X \otimes I \otimes I \otimes X \otimes X, & (2.32) \\
S_3 &= X \otimes I \otimes X \otimes I \otimes X \otimes I \otimes X, & S_4 &= I \otimes I \otimes I \otimes Z \otimes Z \otimes Z \otimes Z, & (2.33) \\
S_5 &= I \otimes Z \otimes Z \otimes I \otimes I \otimes Z \otimes Z, & S_6 &= Z \otimes I \otimes Z \otimes I \otimes Z \otimes I \otimes Z. & (2.34)
\end{aligned}
$$

The logical operator for X and Z are given by

$$
X_{\mathrm{L}} = X \otimes X \otimes X \otimes X \otimes X \otimes X \otimes X, \quad Z_{\mathrm{L}} = Z \otimes Z \otimes Z \otimes Z \otimes Z \otimes Z \otimes Z. \tag{2.35}
$$

By using the stabilize generators, the Steane 7-qubit code is described as

$$
|i\rangle_{\mathrm{L}} \propto \prod_{j=1}^{6} \frac{I + S_j}{2} |i\rangle^{\otimes 7} \qquad (i = 0, 1), \tag{2.36}
$$

where $|i\rangle^{\otimes 7}$ means $|i\rangle |i\rangle |i\rangle |i\rangle |i\rangle |i\rangle |i\rangle$. A quantum error correcting code is referred to as an $[n, k, d]$ code indicating that k logical qubits of information are encoded into n physical qubits and t arbitrary errors can be corrected, where d denotes the distance of the code and satisfies the condition $d \geq 2t + 1$. For the Steane 7-qubit code, the code is referred to as an $[7, 4, 3]$ code.

Surface code

In 1997 Alexei Kitaev proposed surface codes [15]. For general surface code, we can define a simultaneous +1 eigenstate of check operators (stabilizer generators) for vertex V and plaquette P as

$$
A_i = \prod_{j \in V} X_i, \qquad B_i = \prod_{j \in P} Z_i, \tag{2.37}
$$

respectively. We check the measurement outcomes A_i and B_i for a syndrome extraction to detect errors, where A_i and B_i are I with no errors. If measurement outcome give a value

of -1, we can detect an error on the lattice. Since a single *X* error occurs on the lattice that is anti-commutes with B_i, the error can be detected by the measurement of the $B_i = -1$ around each check operators. In addition, among all error correction codes, a surface code is one of the best candidates to be the chosen protocol to implement fault-tolerant quantum computation because of their simple architecture and high error threshold value.

2.1.6 Fault-tolerant quantum computation with discrete variable states

Fault-tolerance

To implement large-scale and reliable quantum computation, fault-tolerance is an essential procedure that realize quantum computation on logical qubits without any error propagating between logical qubits; that is, in a fault-tolerant operation a single error introduces at most a single error per block of the code. Hence, by using the fault-tolerant operation, we can perform the *X* syndrome extraction of the CSS code , where the logical code states $|0\rangle_{\text{L}}$ is used as ancilla qubits to detect errors, By contrast, the syndrome extraction without fault-tolerance , where the single error on the ancilla qubit, introduces to two or more physical qubits.

Fault-tolerant quantum computation

There are various methods for fault-tolerant quantum computation using different error correcting codes. To implement fault-tolerant quantum computation, the transversal gates are used for universal gates and syndrome measurements in a fault-tolerant manner. By using a fault-tolerance manner, the QEC for the logical qubit encoded by the quantum error correcting code is performed so that the single error leads to just a single error in the output logical qubit. Similarly, a logical operation using transversal gates between the logical qubits can be performed transversally to introduce the errors into any other logical qubits.
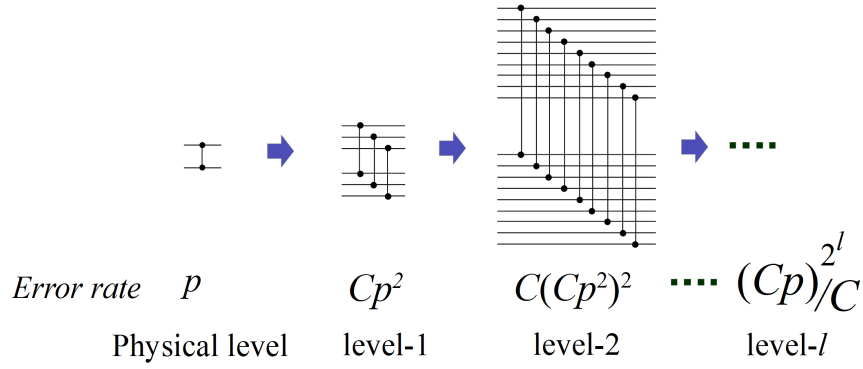
Figure 2.3: Introduction of a concatenated code.

Threshold theorem

To realize reliable quantum computation, the logical error probability should be substantially low so as to obtain a solution of quantum computation with a high-accuracy. This can be done by the concatenation of the quantum error correcting code or surface codes with fault-tolerant manner. This is called threshold theorem, which is defined as

"*If the noise per elementary operation is below a constant non-zero threshold then an arbitrarily long quantum computation can be performed with arbitrary accuracy and small operational overhead* ".

Concatenation

Suppose a quantum error correcting code can reduce the logical error probability from p to Cp^2 by using the QEC, where p denotes the error probability on the single qubit and C is constant. Then, we define the logical error probability Cp^2 as $p^{(1)}$, and we perform repeatedly the QEC to reduce the level-2 logical error probability to $p^{(2)} = C\left(p^{(1)}\right)^2 = C(Cp^2)^2$ as shown in Fig 2.3. By repeating this procedure, the logical error probability can be reduced to

$$p^l = C\left(p^{(l-1)}\right)^2 = \frac{(Cp)^{2^l}}{C},\tag{2.38}$$

where l is the concatenation level. Hence, if the error probability p satisfies the condition $p < 1/C$, the level-l logical error probability can be super exponentially reduced as l becomes large, that is threshold theorem.

16

2.2 Quantum computation with continuous variable states

2.2.1 Qumode

In quantum information processing with discrete variable systems, a discrete and finite number of quantum states are utilized as a basis. By contrast, in quantum information processing with continuous variable systems, a continuous and infinite number of quantum states are utilized as a basis, where the basis is continuously varying quantum states, such as eigenstates of the position and the momentum operators. In continuous variable systems, the individual physical state is referred to as a *qumode*.

Electromagnetic field

The electric and magnetic field in the vacuum state, where there are no charge, is formulated by the Maxwell Equations:

$$\nabla \cdot \mathbf{E} = 0, \quad \nabla \cdot \mathbf{B} = 0, \quad \nabla \times \mathbf{E} + \frac{\partial \mathbf{B}}{\partial t} = 0, \quad \nabla \times \mathbf{B} - \mu_0 \varepsilon_0 \frac{\partial \mathbf{E}}{\partial t} = 0, \tag{2.39}$$

where μ_0 and ε_0 are the magnetic permeability and electric permittivity for free space, respectively, and satisfy the relation with the free space speed of light c as $\sqrt{\mu_0 \varepsilon_0} = c$. Then, the time dependent electric field $E(r,t)$ is obtained from the equation as

$$\left(\nabla^2 - \frac{\partial^2}{\partial t^2} \right) E = 0. \tag{2.40}$$

From the equation, $E(r,t)$ is described as

$$E(r,t) = \sum_k \sqrt{\frac{h\omega_k}{2\varepsilon_0}} \left(\alpha_k v_k(r) e^{-i\omega kt} - \alpha_k^* v_k(r)^* e^{i\omega kt} \right) = 0, \tag{2.41}$$

where *hbar*, k, ω_k, α_k, and v are the reduced Planck constant, the index of the mode, the angular frequency of the mode k, the electric field complex amplitude for the mode k, and a mode function, respectively.

Quantized electromagnetic field

$E(r,t)$ in Eq. (2.42) is quantized by replacing the electric field complex amplitude by the annihilation $\hat{a}_k$ and creation operators $\hat{a}_k^\dagger$ as

$$\hat{E}(r,t) = \sum_k \sqrt{\frac{\hbar\omega_k}{2\varepsilon_0}} \left(\hat{a}_k v_k(r)e^{-i\omega kt} - \hat{a}_k^\dagger v_k(r)^* e^{i\omega kt} \right) = 0. \tag{2.42}$$

The Hamiltonian for the electromagnetic field H is also quantized as

$$H = \sum_k \hbar\omega_k \left(\hat{a}_k^\dagger \hat{a}_k + \frac{1}{2} \right). \tag{2.43}$$

For the operators $\hat{a}_k$ and $\hat{a}_k^\dagger$, the commutation relations become

$$[\hat{a}_k, \hat{a}_{k'}] = [\hat{a}_k^\dagger, \hat{a}_{k'}^\dagger] = 0, \quad [\hat{a}_k^\dagger, \hat{a}_{k'}^\dagger] = \delta_{kk'}. \tag{2.44}$$

The quadrature operators of the position $\hat{q}$ and the momentum $\hat{p}$ are described as

$$\hat{q} = \sqrt{\frac{\hbar}{2}}(\hat{a} + \hat{a}^\dagger), \quad \hat{p} = -i\sqrt{\frac{\hbar}{2}}(\hat{a} - \hat{a}^\dagger), \tag{2.45}$$

respectively, and also described as

$$\hat{a} = \sqrt{\frac{\hbar}{2}}(\hat{q} + i\hat{p}), \quad \hat{a}^\dagger = \sqrt{\frac{\hbar}{2}}(\hat{q} - i\hat{p}^\dagger). \tag{2.46}$$

Uncertainty principle for quadratures

The quadrature operators $\hat{q}$ and $\hat{p}$ obey the relation $[\hat{q}, \hat{p}] = i$, and by applying the uncertainty principle to $\hat{q}$ and $\hat{p}$ the variances of quadrature operators obey the Heisenberg uncertainty principle as

$$\Delta^2\hat{q}\,\Delta^2\hat{p} \geq \frac{1}{2}\hbar, \tag{2.47}$$

where the variances $\Delta^2\hat{x}$ and $\Delta^2\hat{p}$ are given as

$$\Delta^2\hat{q} = \langle \hat{q}^2 \rangle - \langle \hat{q} \rangle^2, \quad \Delta^2\hat{p} = \langle \hat{p}^2 \rangle - \langle \hat{p} \rangle^2. \tag{2.48}$$

Eq. (2.47) means that $\hat{q}$ and $\hat{p}$ cannot be determined simultaneously.

Coherent state

Suppose the state $|\alpha\rangle$ is representing a coherent state. The state $|\alpha\rangle$ is described using the annihilation operator $\hat{a}$ as

$$\hat{a}|\alpha\rangle = \alpha|\alpha\rangle, \tag{2.49}$$

where $|\alpha\rangle$ is the eigenvalue of the annihilation operator acting on the coherent state. The vacuum state $|0\rangle$ is represented by a coherent state with $\alpha = 0$. The coherent state can be also described by photon number state (Fock state) as follows:

$$|\alpha\rangle = e^{-\frac{1}{2}|\alpha|^2} \sum_n \frac{\alpha^n}{\sqrt{n!}} |n\rangle, \tag{2.50}$$

where $|n\rangle$ is photon number states.

Squeezed vacuum state

A squeezed vacuum state is defined as

$$\hat{S}(r)|0\rangle, \tag{2.51}$$

where $\hat{S}(r)$ is a squeezing operator described as $\hat{S}(r) = e^{\frac{r}{2}(\hat{a}^2 - \hat{a}^2\dagger)}$, and r is a squeezing parameter. The squeezing operator transforms $\hat{a}$ and $\hat{a}^\dagger$:

$$\hat{S}^\dagger(r)\hat{a}\hat{S} = \hat{a}\cosh r - \hat{a}^\dagger\sinh r, \quad \hat{S}^\dagger(r)\hat{a}^\dagger\hat{S} = \hat{a}^\dagger\cosh r - \hat{a}\sinh r, \tag{2.52}$$

$$\hat{S}^\dagger(r)\hat{q}\hat{S} = e^{-r}\hat{q}, \quad \hat{S}^\dagger(r)\hat{p}\hat{S} = e^r\hat{p}. \tag{2.53}$$

From Eq. (2.53), we obtain $\langle\hat{q}\rangle = \langle\hat{p}\rangle = 0$, $\langle\hat{q^2}\rangle = \frac{\hbar}{2}e^{-2r}$, and $\langle\hat{p^2}\rangle = \frac{\hbar}{2}e^{2r}$, respectively. Hence, we get

$$\langle\Delta^2\hat{q}\rangle = \frac{\hbar}{2}e^{-2r}, \quad \langle\Delta^2\hat{p}\rangle = \frac{\hbar}{2}e^{2r}, \quad \langle\Delta\hat{q}\rangle = \sqrt{\frac{\hbar}{2}}e^{-r}, \quad \langle\Delta\hat{p}\rangle = \sqrt{\frac{\hbar}{2}}e^r, \tag{2.54}$$

respectively. We notice that $\langle \Delta \hat{q} \rangle$ and $\langle \Delta \hat{p} \rangle$ satisfy the relation $\langle \Delta \hat{q} \rangle \langle \Delta \hat{p} \rangle = \hbar/2$.

Homodyne detection

The continuous variables in quantum optics are generally detected by using the homodyne detection. In this thesis, we assume that the homodyne measurement is used to measure on quantum states in the quadrature. The annihilation operator of the signal mode and the complex amplitude of the local oscillator are given by $\hat{a}$ and $|\alpha|e^{i\phi}$, respectively. A beam splitter coupling implemented between the signal and the local oscillator modes by using a 50:50 beam splitter (half beam splitter). This operation leads to the operators as

$$\hat{a}_1 = \frac{1}{\sqrt{2}}(\hat{a} + \alpha), \qquad \hat{a}_2 = \frac{1}{\sqrt{2}}(-\hat{a} + \alpha), \tag{2.55}$$

where the $\hat{a}_1$ and $\hat{a}_2$ are the annihilation operator for the mode 1 and 2 coupled by the beam splitter.

2.2.2 Quantum gate

In the continuous variables, the analog for the computational basis states $|0\rangle$ ($|1\rangle$) and the conjugate basis states $|+\rangle$ ($|-\rangle$) are given by a continuum of orthogonal states $|s\rangle_q$ and $|s\rangle_p$:

$$|s\rangle_p = \frac{1}{\sqrt{2\pi}} \int_{-\infty}^{\infty} dr e^{irs} |r\rangle_q = F |s\rangle_q, \tag{2.56}$$

$$|s\rangle_q = \frac{1}{\sqrt{2\pi}} \int_{-\infty}^{\infty} dr e^{-irs} |r\rangle_p = F^\dagger |s\rangle_p, \tag{2.57}$$

where $|s\rangle_q$ and $|s\rangle_p$ related by a Fourier transform operation F. The $|s\rangle_q$ and $|s\rangle_p$ are also defined by $\hat{q}|s\rangle_q = s|s\rangle_q$ and $\hat{p}|s\rangle_p = s|s\rangle_p$, respectively. These basis states satisfy

$$\int_{\infty}^{\infty} dq |q\rangle \langle q| = 1, \quad \int_{\infty}^{\infty} dp |p\rangle \langle p| = 1, \quad \langle q|q'\rangle = \delta(q - q'), \quad \langle p|p'\rangle = \delta(p - p'). \tag{2.58}$$

Displacement operation

The displacement operation is represented by $X(s) = e^{-is\hat{p}}$ ($\hbar = 1$) for the q quadrature and $Z(s) = e^{is\hat{q}}$ for the p quadrature, where this operations act on the states $|0\rangle_q$ and $|0\rangle_p$ as

$$|s\rangle_q = X(s)|0\rangle_q, \quad |s\rangle_p = Z(s)|0\rangle_p, \tag{2.59}$$

respectively. By using $\hat{a} = (\hat{q} + i\hat{p})/\sqrt{\pi}$, the coherent state $|\alpha\rangle$ is represented by the displacement operation $\hat{D}(\alpha)$ acting on the vacuum state as

$$|\alpha\rangle = \hat{D}(\alpha)|0\rangle, \tag{2.60}$$

where $\hat{D}(\alpha) = e^{\alpha\hat{a}^\dagger - \alpha^*\hat{a}}$. As shown in Eq. (2.59), the displacement operation $X(s) = e^{-is\hat{p}}$ and $Z(s) = e^{is\hat{q}}$ are referred to as Gaussian transformation in terms of the quadrature:

$$\begin{pmatrix} \hat{q} \\ \hat{p} \end{pmatrix} \rightarrow \begin{pmatrix} \hat{q} + s \\ \hat{p} \end{pmatrix}, \quad \begin{pmatrix} \hat{q} \\ \hat{p} \end{pmatrix} \rightarrow \begin{pmatrix} \hat{q} \\ \hat{p} + s \end{pmatrix}, \tag{2.61}$$

respectively.

Rotation operation

A rotation (phase shift) operation is defined as $R(\theta) = ei\theta(\hat{q}^2 + \hat{p}^2)/2$, which rotates a state in phase space by an angle θ:

$$\begin{pmatrix} \hat{q} \\ \hat{p} \end{pmatrix} \rightarrow \begin{pmatrix} \cos\theta & -\sin\theta \\ \sin\theta & \cos\theta \end{pmatrix} \begin{pmatrix} \hat{q} \\ \hat{p} \end{pmatrix}. \tag{2.62}$$

In the case of $\theta = \pi/2$, the rotation operation $R(\pi/2)$ is equal to Fourier transformation F.

Squeezing operation

The squeezing operation $\hat{S}(r) = e^{\frac{r}{2}(\hat{a}^2 - \hat{a}^2\dagger)}$ is also represented as $R(\theta) = e^{-ir2(\hat{q}\hat{p} + \hat{p}\hat{q})}$:

$$\begin{pmatrix} \hat{q} \\ \hat{p} \end{pmatrix} \rightarrow \begin{pmatrix} e^r & 0 \\ 0 & e^{-r} \end{pmatrix} \begin{pmatrix} \hat{q} \\ \hat{p} \end{pmatrix}. \tag{2.63}$$

Shearing operation

The shearing operation, which is so-called the phase gate, $P(s) = e^{\frac{s}{2}\hat{q}^2}$ with respect to the q quadrature by a gradient of s:

$$\begin{pmatrix} \hat{q} \\ \hat{p} \end{pmatrix} \rightarrow \begin{pmatrix} 1 & 0 \\ s & 1 \end{pmatrix} \begin{pmatrix} \hat{q} \\ \hat{p} \end{pmatrix}. \tag{2.64}$$

CZ gate

The CZ gate operation is defined as $U_{CZ} = e^{ig\hat{q}_1 \cdot \hat{q}_2}$ with the weighted parameter (interaction strength) g, which interacts between the two qumodes 1 and 2:

$$\begin{pmatrix} \hat{q}_1 \\ \hat{p}_1 \\ \hat{q}_2 \\ \hat{p}_2 \end{pmatrix} = \begin{pmatrix} 1 & 0 & 0 & 0 \\ 0 & 1 & g & 0 \\ 0 & 0 & 1 & 0 \\ g & 0 & 0 & 1 \end{pmatrix} \begin{pmatrix} \hat{q}_1 \\ \hat{p}_1 \\ \hat{q}_2 \\ \hat{p}_2 \end{pmatrix}. \tag{2.65}$$

In the case of the weighted parameter $g=1$, the CZ gate transforms the quadrature as

$$\begin{pmatrix} \hat{q}_1 \\ \hat{p}_1 \\ \hat{q}_2 \\ \hat{p}_2 \end{pmatrix} \rightarrow \begin{pmatrix} \hat{q}_1 \\ \hat{p}_1 - \hat{q}_2 \\ \hat{q}_2 \\ \hat{p}_2 - \hat{q}_1 \end{pmatrix}. \tag{2.66}$$

2.2.3 Entangled states and stabilizer

Cluster state

In a continuous variable system with squeezed vacuum states, the cluster states is generated by the CZ gate between the squeezed vacuum states in the p quadrature. For ex-

ample, the two-mode cluster state (the 2-linear cluster state) $|2l\rangle = U_{CZ_{12}} |0\rangle_{p,1} |0\rangle_{p,2} = e^{\frac{i}{\hbar}\hat{q}_1\hat{q}_2} |0\rangle_{p,1} |0\rangle_{p,2}$, is described as

$$|2l\rangle = \frac{1}{\sqrt{2\pi\hbar}} \int_{-\infty}^{\infty} du |u\rangle_{q,1} |u\rangle_{p,2} = \frac{1}{\sqrt{2\pi\hbar}} \int_{-\infty}^{\infty} dv |v\rangle_{p,1} |v\rangle_{q,2}. \qquad (2.67)$$

The relations in terms of the quadrature are $\hat{p}_1 - \hat{q}_2 = 0$ and $\hat{p}_2 - \hat{q}_1 = 0$, satisfied $(\hat{p}_1 - \hat{q}_2)|2l\rangle = 0$ and $(\hat{p}_2 - \hat{q}_1)|2l\rangle = 0$. Similarly, the three-mode cluster state (the 3-linear cluster state), $|3l\rangle = U_{CZ_{12}} U_{CZ_{23}} |0\rangle_{p,1} |0\rangle_{p,2} |0\rangle_{p,3} = e^{\frac{i}{\hbar}\hat{q}_1\hat{q}_2} e^{\frac{i}{\hbar}\hat{q}_2\hat{q}_3} |0\rangle_{p,1} |0\rangle_{p,2} |0\rangle_{p,3}$, is described as

$$|3l\rangle = \frac{1}{\sqrt{2\pi\hbar}} \int_{-\infty}^{\infty} du \int_{-\infty}^{\infty} dv |u\rangle_{q,1} |u+v\rangle_{p,2} |v\rangle_{q,3} = \frac{1}{\sqrt{2\pi\hbar}} \int_{-\infty}^{\infty} du |u\rangle_{p,1} |u\rangle_{q,2} |u\rangle_{p,3}. \qquad (2.68)$$

The relations in terms of the quadrature are $\hat{p}_1 - \hat{q}_2 = 0$, $\hat{p}_2 - \hat{q}_1 - \hat{q}_3 = 0$, and $\hat{p}_3 - \hat{q}_2 = 0$.

2.2.4 Measurement-based quantum computation with continuous variable states

We here explain measurement-based quantum computation with squeezed vacuum states. In a similar fashion with the discrete variables, quantum computation is implemented by the measurement of the qumodes and the feedforward operation depending on the measurement results. For example of measurement-based quantum computation in continuous variables, suppose that the input state is

$$U_{CZ}(|\phi\rangle_{\text{in}} |0\rangle_p) = U_{CZ}\left(\int_{-\infty}^{\infty} ds f(s) |s\rangle_q |0\rangle_q\right) = \int_{-\infty}^{\infty} ds f(s) |s\rangle_q |s\rangle_q. \qquad (2.69)$$

The first mode of the 2-linear cluster is measured in the p quadrature with associated result m , and then the output state, teleporting to the second mode , is given

$$|\phi\rangle_{\text{out}} \quad \propto \quad \int_{-\infty}^{\infty} ds f(s) \left(\langle m|_p |s\rangle_q\right) |s\rangle_p \propto \int_{-\infty}^{\infty} ds f(s) e^{-ism} |s\rangle_p \qquad (2.70)$$

$$= \quad e^{-is\hat{p}} \int_{-\infty}^{\infty} ds f(s) |s\rangle_p = X(m) F |\phi\rangle_{\text{in}}. \qquad (2.71)$$

The arbitrary single-mode Gaussian unitary operation is implemented by the measurement on the 4-linear cluster state. We define a sequence of measurement on the 4-linear cluster in the $(\hat{p} + m_j\hat{q})$ quadrature as (m_1, m_2, m_3, m_4), where j denotes the j-th qumode. By

using this definition, the quantum gates I, F, and P on the input state $|\phi\rangle_{\text{in}}$ is given by (0, 0, 0, 0), (1, 1, 1, 0), and (1, 0, 0, 0), respectively.

2.2.5 Fault-tolerant quantum computation with continuous variable states

Unfortunately, it is impossible to implement fault-tolerant quantum computation with only the squeezed vacuum states, since the squeezed vacuum state does not offer the QEC with a fault-tolerant manner. Hence, to implement QEC with a fault-tolerant manner, the continuous variable state should be digitized using the appropriate code states such as the GKP qubit and the cat code. Then, the digitized continuous variable states can be applied to the standard quantum error correcting code used for fault-tolerant quantum computation with the discrete variables. In the next section, we explain the fault-tolerant quantum computation with the GKP qubit.

2.3 Quantum computation with the GKP qubit

In this section, we firstly explain the GKP qubit and the noise model in this thesis. Then, we describe measurement-based quantum computation with the GKP qubit. Finally, fault-tolerant quantum computation regarding the threshold of the squeezing level of the GKP qubit is described.

2.3.1 GKP qubit

Gottesman, Kitaev, and Preskill proposed a method to encode a qubit in an oscillator's q and p quadratures to correct errors caused by a small deviation (displacement) in the q and p quadratures.

Ideal GKP qubit

The basis of the ideal GKP qubit is composed of a series of Gaussian peaks of a Dirac comb and separation $\sqrt{\pi}$ embedded in a infinite phase space. The code words of the GKP qubit code are coherent superpositions of infinitely squeezed states (up to normalization)

and are defined as

$$
|\widetilde{0}\rangle_{\text{ideal}} = \sum_{t=-\infty}^{\infty} |2t\sqrt{\pi}\rangle_q = \sum_{t=-\infty}^{\infty} |t\sqrt{\pi}\rangle_p , \tag{2.72}
$$

$$
|\widetilde{1}\rangle_{\text{ideal}} = \sum_{t=-\infty}^{\infty} |2(t+1)\sqrt{\pi}\rangle_q = \sum_{t=-\infty}^{\infty} (-1)^t |t\sqrt{\pi}\rangle_p . \tag{2.73}
$$

Also, we can construct the GKP qubit as

$$
\Big(\sum_{s=-\infty}^{\infty} e^{-isp\alpha} \Big) \Big(\sum_{t=-\infty}^{\infty} e^{2\pi itq/\alpha} \Big) |\psi\rangle = \sum_{s,t=} \exp\big[i(-sp\alpha + 2\pi tq/\alpha + \pi st)\big] |\psi\rangle . \tag{2.74}
$$

Approximate GKP qubit
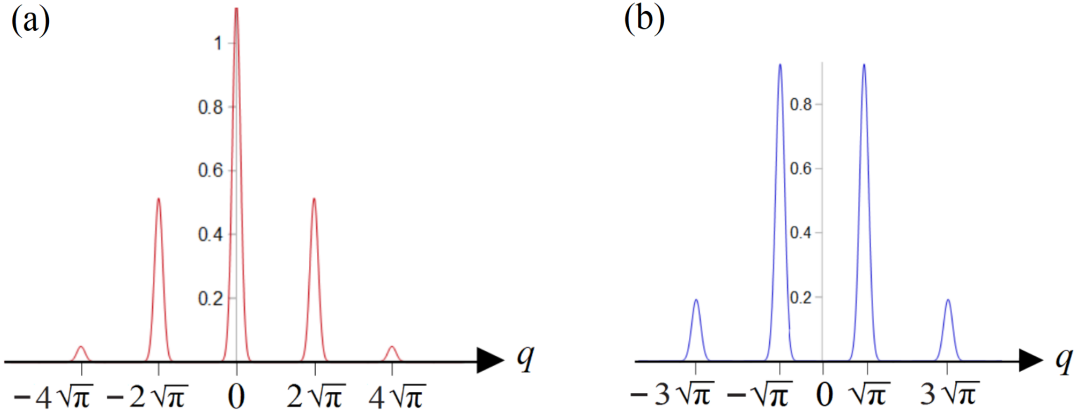
Figure 2.4: Absolute value of the wave function of the approximate GKP qubit (a) $|\widetilde{0}\rangle$ state and (b) $|\widetilde{1}\rangle$ state.

The ideal GKP qubit is clearly unphysical, since they they have an infinite squeezing that requires infinite energy expectation value. Hence, we must consider the approximation of the ideal GKP qubit that are physically realizable. The basis of the approximate GKP qubit is composed of a series of Gaussian peaks of width σ and separation $\sqrt{\pi}$ embedded in a larger Gaussian envelope of width $1/\sigma$. Although in the case of infinite squeezing ($\sigma \to 0$) the GKP qubit bases become orthogonal, in the case of finite squeezing, the approximate code states are not orthogonal. The approximate GKP qubit $|\widetilde{0}\rangle$ and $|\widetilde{1}\rangle$ (up
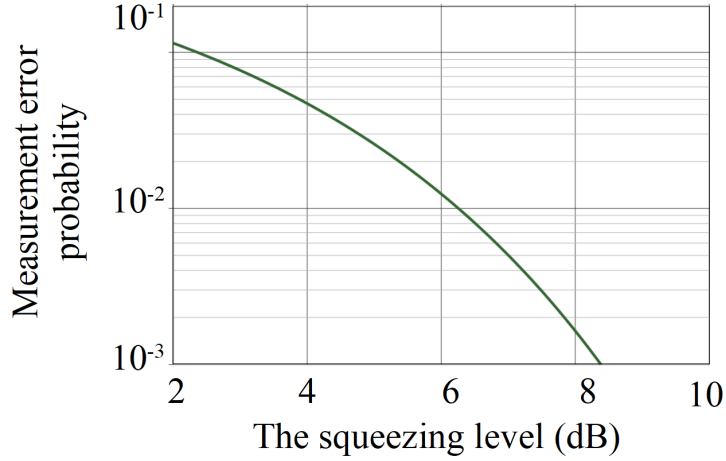
Figure 2.5: Measurement error probabilities of the GKP qubit with the finite squeezing.

to normalization) are defined as

$$|\widetilde{0}\rangle \propto \sum_{t=-\infty}^{\infty} \int e^{-2\pi\sigma^2 t^2} e^{-(q-2t\sqrt{\pi})^2/(2\sigma^2)} |q\rangle \, dq, \tag{2.75}$$

$$|\widetilde{1}\rangle \propto \sum_{t=-\infty}^{\infty} \int e^{-\pi\sigma^2(2t+1)^2/2} e^{-(q-(2t+1)\sqrt{\pi})^2/(2\sigma^2)} |q\rangle \, dq. \tag{2.76}$$

Measurement error of the approximate GKP qubit

Since the approximate GKP qubits are not orthogonal, there is a probability of misidentifying $|\widetilde{0}\rangle$ as $|\widetilde{1}\rangle$, and vice versa. Provided the measured magnitude deviates less than $\sqrt{\pi}/2$ from the peak value, the decision of the bit value from the measurement of the GKP qubit is correct. The probability p_{corr} that we identify the correct bit value is the portion of a normalized Gaussian of a variance σ^2 that lies between $-\sqrt{\pi}/2$ and $\sqrt{\pi}/2$ [4]:

$$p_{\mathrm{corr}} = \int_{-\frac{\sqrt{\pi}}{2}}^{\frac{\sqrt{\pi}}{2}} dx \frac{1}{\sqrt{2\pi\sigma^2}} \exp(-x^2/2\sigma^2). \tag{2.77}$$

The probability of the misidentification of the bit value is calculated as $1 - p_{\mathrm{corr}}$. In Fig. 2.8, measurement error probability $1 - p_{\mathrm{corr}}$ is plotted as a function of the squeezing level, where the squeezing level is equal to $-10\log_{10}(2\sigma^2)$. In addition to the imperfection that originates from the finite squeezing of the initial states, we consider the Gaussian quantum channel and a photon loss channel.

Gaussian quantum channel

The Gaussian quantum channel is a natural generalization of the Gaussian classical channel. The Gaussian quantum channel [5, 16] leads to a displacement in the q and p quadratures independently. The channel is described by superoperator ζ acting on density operator ρ as follows:

$$\rho \to \zeta(\rho) = \frac{1}{\pi\xi^2} \int d^2\alpha e^{-|\alpha|^2/\xi^2} D(\alpha)\rho D(\alpha)^\dagger, \tag{2.78}$$

where $D(\alpha)$ is a displacement operator in the phase space. The position q and momentum p are displaced independently as follows:

$$q \to q+v, \quad p \to p+u, \tag{2.79}$$

where v and u are real Gaussian random variables with mean zero and variance ξ^2. The Gaussian quantum channel conserves the position of the Gaussian peaks in the probability density function on the measurement outcome of the GKP qubit, but increases the variance as ξ^2. Therefore, we evaluate the performance under a code capacity noise model, where the noise is parameterized by a single variance σ^2 that includes the squeezing level of the initial GKP qubit and the degradation via the Gaussian quantum channel.

Photon loss channel

In addition to the Gaussian quantum channel, we consider the transmission loss channel $\mathscr{L}$, i.e. photon loss channel. The transmission loss channel $\mathscr{L}$ transforms the variables in the q and p quadrature

$$\hat{q} \to \sqrt{\eta}\hat{q}, \quad \hat{p} \to \sqrt{\eta}\hat{p}, \tag{2.80}$$

where $\sqrt{\eta}$ is the transmittance coefficient. The variances in the q and p quadrature,

$$\sigma^2_{\text{in},q} \quad \to \quad \sigma^2_{\text{out},q} = \eta\sigma^2_{\text{in},q} + (1-\eta)/2, \tag{2.81}$$

$$\sigma^2_{\text{in},p} \quad \to \quad \sigma^2_{\text{out},p} = \eta\sigma^2_{\text{in},p} + (1-\eta)/2, \tag{2.82}$$

where $\sigma^2_{\text{in},q}$ and $\sigma^2_{\text{in},p}$ are the variances before the transmission loss channel $\mathscr{L}$, respectively. In this work, we assume that the $\sigma^2_{\text{in},q}$ and $\sigma^2_{\text{in},p}$ of the single GKP qubit are equal to $(1/2)e^{-2r}$, where r is the squeezing parameter.

Single-qubit level quantum error correction

In Ref. [5], the single-qubit level QEC has been proposed to correct a displacement (deviation) error derived from the finite squeezing of the GKP qubit or the Gaussian quantum channel. We here explain the single-qubit level QEC to correct the displacement error in the p quadrature in detail. In this single-qubit level QEC in the p quadrature as shown in Fig. 2.6(a), an additional single ancilla qubit is entangled with the data qubit by a CNOT gate, where the data qubit is the target qubit. The ancilla qubit is prepared in the state $|\widetilde{0}\rangle$ to prevent us from identifying the bit value of the data qubit. The CNOT gate, which corresponds to the operator $\exp(-i\hat{q}_{\mathrm{a}}\hat{p}_{\mathrm{D}})$ for continuous variables, transforms

$$\hat{q}_{\mathrm{a}} \quad \rightarrow \quad \hat{q}_{\mathrm{a}}, \tag{2.83}$$

$$\hat{p}_{\mathrm{a}} \quad \rightarrow \quad \hat{p}_{\mathrm{a}} - \hat{p}_{\mathrm{D}}, \tag{2.84}$$

$$\hat{q}_{\mathrm{D}} \quad \rightarrow \quad \hat{q}_{\mathrm{D}} + \hat{q}_{\mathrm{a}}, \tag{2.85}$$

$$\hat{p}_{\mathrm{D}} \quad \rightarrow \quad \hat{p}_{\mathrm{D}}, \tag{2.86}$$

where $\hat{q}_{\mathrm{D}}(\hat{p}_{\mathrm{D}})$ and $\hat{q}_{\mathrm{a}}(\hat{p}_{\mathrm{a}})$ are the quadrature operators of the data and ancilla qubits in the position q (momentum p), respectively. Regarding the deviation, the CNOT gate operation displaces the deviation of the q and p quadratures as

$$\overline{\Delta}_{q,\mathrm{a}} \quad \rightarrow \quad \overline{\Delta}_{q,\mathrm{a}}, \tag{2.87}$$

$$\overline{\Delta}_{p,\mathrm{a}} \quad \rightarrow \quad \overline{\Delta}_{p,\mathrm{a}} - \overline{\Delta}_{p,\mathrm{D}}, \tag{2.88}$$

$$\overline{\Delta}_{q,\mathrm{D}} \quad \rightarrow \quad \overline{\Delta}_{q,\mathrm{D}} + \overline{\Delta}_{q,\mathrm{a}}, \tag{2.89}$$

$$\overline{\Delta}_{p,\mathrm{D}} \quad \rightarrow \quad \overline{\Delta}_{p,\mathrm{D}}, \tag{2.90}$$

where $\overline{\Delta}_{q,\mathrm{D}}(\overline{\Delta}_{p,\mathrm{D}})$ and $\overline{\Delta}_{q,\mathrm{a}}(\overline{\Delta}_{p,\mathrm{a}})$ are the true deviation values of the data and ancilla qubits in the position q (momentum p), respectively. We assume that the deviations of the data qubit in the q and p quadratures obey the Gaussian distribution with the variance $\sigma_{\mathrm{D},q}^2$ and $\sigma_{\mathrm{D},p}^2$, and the deviations of the ancilla qubit in the q and p quadratures obey the Gaussian distribution with the variance $\sigma_{\mathrm{a},q}^2$ and $\sigma_{\mathrm{a},p}^2$, respectively. After the CNOT gate, we
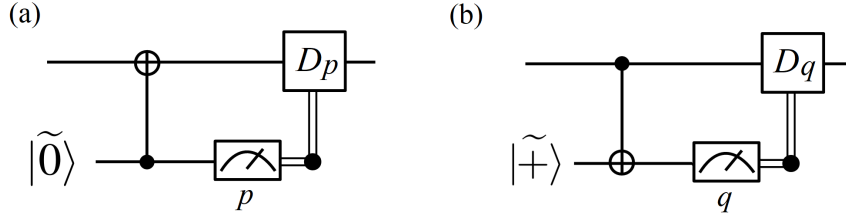
Figure 2.6: A circuit for the single-qubit level QEC for (a) the p quadrature and (b) the q quadrature .

measure the ancilla qubit in the p quadrature, and obtain the deviation of the ancilla qubit $\Delta_{mp,a}$ that obeys the Gaussian distribution with the variance $\sigma^2_{D,p} + \sigma^2_{a,p}$. Then, we perform the displacement $|\Delta_{mp,a}|$ on the p quadrature of the data qubit to correct by shifting back in the direction to minimize the deviation. If $|\Delta_{mp,a}| = |\overline{\Delta}_{p,a} - \overline{\Delta}_{p,D}|$ is less than $\sqrt{\pi}/2$, the true deviation value of the data qubit in the p quadrature changes from $\overline{\Delta}_{p,D}$ to $\overline{\Delta}_{p,a}$ after the displacement operation, which displaces $\overline{\Delta}_{p,D}$ by $\Delta_{mp,a}(= \overline{\Delta}_{p,a} - \overline{\Delta}_{p,D})$. On the other hand, if $|\overline{\Delta}_{p,a} - \overline{\Delta}_{p,n}|$ is more than $\sqrt{\pi}/2$, the bit error in the p quadrature occurs after the displacement operation. Therefore, the single-qubit level QEC for the data qubit in the p quadrature can reduce the variance of the data qubit in the p quadrature from $\sigma^2_{D,p}$ to $\sigma^2_{a,p}$. The variance of the data qubit in the q quadrature after the single-qubit level QEC increases from $\sigma^2_{D,q}$ to $\sigma^2_{D,q} + \sigma^2_{a,q}$, since the true deviation $\overline{\Delta}_{q,D}$ and $\overline{\Delta}_{q,a}$ obey the Gaussian distribution with the variance $\sigma^2_{D,q}$ and $\sigma^2_{a,q}$, respectively, where the $\overline{\Delta}_{q,D}$ and $\overline{\Delta}_{q,a}$ are the true deviation of the data qubit and the ancilla qubit, respectively. Similarly, the single-qubit level QEC in the q quadrature can be performed using the second ancilla qubit. As shown in Fig. 2.6(b), the ancilla is prepared in the state $|\widetilde{+}\rangle$ and the data qubit is assumed to be the control qubit. Regarding the deviation, the CNOT gate operation displaces the deviation of the q and p quadratures as

$$\overline{\Delta}_{q,a2} \;\; \rightarrow \;\; \overline{\Delta}_{q,a2} + \overline{\Delta}_{q,D} + \overline{\Delta}_{q,a}, \tag{2.91}$$

$$\overline{\Delta}_{p,a2} \;\; \rightarrow \;\; \overline{\Delta}_{p,a2}, \tag{2.92}$$

$$\overline{\Delta}_{q,D} + \overline{\Delta}_{q,a} \;\; \rightarrow \;\; \overline{\Delta}_{q,D} + \overline{\Delta}_{q,a}, \tag{2.93}$$

$$\overline{\Delta}_{p,a} \;\; \rightarrow \;\; \overline{\Delta}_{p,a} - \overline{\Delta}_{p,a2}, \tag{2.94}$$

where $\overline{\Delta}_{q,a2}(\overline{\Delta}_{p,a2})$ is the true deviation value of the second ancilla qubit in the position q (momentum p). After the CNOT gate, we measure the ancilla qubit in the q quadrature, and obtain the deviation of the ancilla qubit $\Delta_{mq,a2}$. Then, we perform

the displacement $|\Delta_{\mathrm{m}q,\mathrm{a2}}|$ on the q quadrature of the data qubit to correct by shifting back in the direction to minimize the deviation. If $|\Delta_{\mathrm{m}q,\mathrm{a2}}| = |\overline{\Delta}_{q,\mathrm{a2}} + \overline{\Delta}_{q,\mathrm{D}} + \overline{\Delta}_{q,\mathrm{a}}|$ is less than $\sqrt{\pi}/2$, the true deviation value of the data qubit in the q quadrature changes from $\overline{\Delta}_{q,\mathrm{D}} + \overline{\Delta}_{q,\mathrm{a}}$ to $-\overline{\Delta}_{q,\mathrm{a2}}$ after the displacement operation, which displaces $\overline{\Delta}_{q,\mathrm{D}} + \overline{\Delta}_{q,\mathrm{a}}$ by $-\Delta_{\mathrm{m}p,\mathrm{a}}(= -\overline{\Delta}_{q,\mathrm{a2}} - \overline{\Delta}_{q,\mathrm{D}} - \overline{\Delta}_{q,\mathrm{a}})$. On the other hand, if $\overline{\Delta}_{q,\mathrm{a2}} + \overline{\Delta}_{q,\mathrm{D}} + \overline{\Delta}_{q,\mathrm{a}}$ is more than $\sqrt{\pi}/2$, the bit error in the q quadrature occurs after the displacement operation. To summarize, after the sequential single-qubit level QECs in the p and q quadrature, the variances of the data qubit in the q and p quadratures become σ^2 and $2\sigma^2$, respectively, where the variance of ancilla qubits is σ^2. Although the single-qubit level QEC works well for the small deviation, we need to operate the logical-qubit level QEC to correct the deviation greater than $\sqrt{\pi}/2$.

2.3.2 Fault-tolerant quantum computation with the GKP qubit

To implement FTQC with continuous variables, Menicucci adopted the squeezed vacuum states as a resource for measurement-based quantum computation and GKP ancilla qubits for the single-qubit level QEC for small deviation in phase space. In this model an ancilla's noise in the q quadrature propagates in the data qubit and is teleported to squeezed vacuum states. In this thesis, since we consider mainly quantum computation with the $full$-GKP qubits, we adopt the GKP qubits as a resource for not only error correction, but also measurement-based quantum computation.

Measurement-based quantum computation with the squeezed vacuum state and the GKP qubit

Firstly, we describe the FTQC with the squeezed vacuum state and the GKP qubits. Fig. 2.7 shows a quantum circuit based on the measurement-based quantum computation to perform an arbitrary single-mode quantum gate and the single-qubit level QECs in the q and p quadratures. The sequential single-qubit level QECs correct the deviation on the data qubit $|\widetilde{\psi}\rangle$ in both the q and p quadratures, where the deviation is accumulated during the single-mode quantum gate. This deviation in the p quadrature, s_p, is an added-up value of the deviation of both the data qubit and first ancilla GKP qubit $|\widetilde{0}\rangle$ as shown in Fig. 2.7 (a), which is based on a circuit model. The ancilla is measured to perform
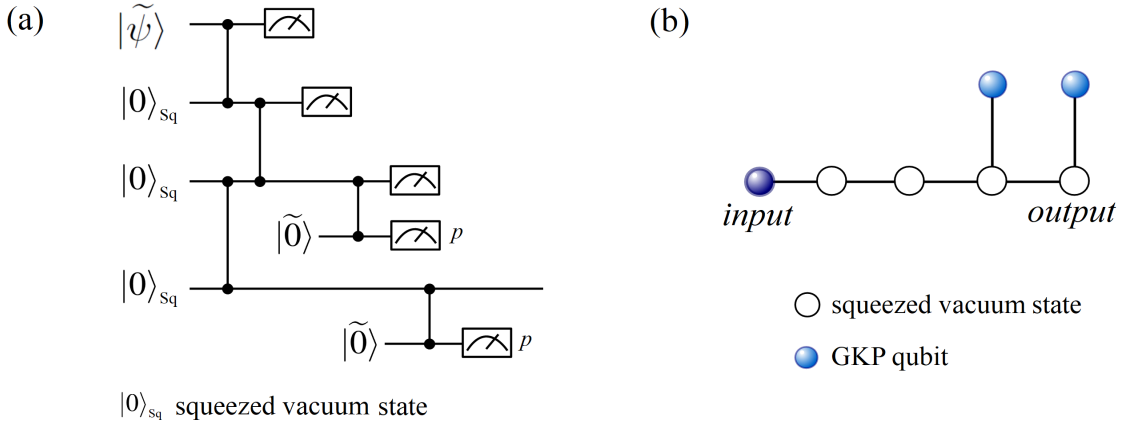
Figure 2.7: A quantum circuit for the arbitrary single-mode quantum gate with the single-qubit level QEC on the data (input) qubit $|\widetilde{\psi}\rangle$ in the q and p quadratures.

the single-qubit level QEC in q quadrature. To correct the deviation in the p quadrature, second $|\widetilde{0}\rangle$ and two Fourier transforms on the data are used. This is because that 0 and 1 states in the computational basis $\{|\widetilde{0}\rangle, |\widetilde{1}\rangle\}$, and + and - states in the conjugate basis states $\{|\widetilde{+}\rangle, |\widetilde{-}\rangle\}$ are related by the Fourier transform F. Hence, we can correct the deviation in the q and p quadratures in the sequential single-qubit level QEC using two ancilla GKP qubits $|\widetilde{0}\rangle$. The circuits depicted in Fig.2.7 (a) can be written by cluster states with squeezed vacuum cluster states in Fig. 2.7 (b), where the blank nodes represent squeezed vacuum states. After the measurement on the squeezed vacuum states and GKP qubits except for last blank node of the squeezed vacuum state, the data qubit $|\widetilde{\psi}\rangle$ is teleported to the last blank node after the feedforward operation according to the measurement outcome. Therefore, we can perform any single mode gate with the single-qubit level QECs in the q and p quadratures, since the arbitrary single mode gate is implemented by the measurement on the linear cluster states composing the four squeezed vacuum states. The failure probability of the qubit-level error is determined by the initial variance (squeezing level) of the data and the ancilla qubits. When the qubit-level errors occur, we must correct these errors by using the quantum error correcting code such as the steane 7-qubit code, the Knill's C_4/C_6 code, the surface code, and so on, which is referred as a logical-qubit level QEC.

Measurement-based quantum computation with the full-GKP qubit

31

In the above model, the noise of ancilla qubits (squeezed vacuum states) in the q quadrature propagate in data qubit and teleported to the subsequent ancilla qubit. To remove this propagation of noise, we can consider the model to eliminate necessity for using the ancilla qubits to correct the deviation on the data qubit by using the quantum teleportation between the only GKP qubits. A quantum circuit for the single-qubit level QEC cab be implemented by quantum teleportation with the Bell state using only the GKP qubits. Quantum teleportation for the single-qubit level QEC works as follows: the data qubit $|\widetilde{\psi}\rangle = \alpha|\widetilde{0}\rangle + \beta|\widetilde{1}\rangle$ is prepared, along with a Bell pair $|\widetilde{\psi}\rangle = (|\widetilde{00}\rangle + |\widetilde{11}\rangle)/\sqrt{2}$. Then $|\widetilde{\psi}\rangle$ and one qubit of the Bell pair are measured together in the q and p quadrature, respectively, which is called the Bell measurement. From the Bell measurement, we obtain a random bit values $q\ (=0\text{ or }1)$, $p\ (=0\text{ or }1)$. The output qubit teleporting to the other qubit of the Bell pair becomes in the initial data qubit $|\widetilde{\psi}\rangle$ after the feedforward operation depending on measurement results. In the case of the GKP qubit, note that we can obtain two bit and deviation values, and the single-qubit level QEC succeeds when quantum teleportation succeeds. Hence, the single-qubit level QEC succeeds, when the magnitude of the deviations of the data and one of the Bell pair for the q and p quadrature are both less than $\sqrt{\pi}/2$. Here, the Bell measurement implicitly works as the CZ gate between the data qubit and one of the Bell pair, . Therefore, measurement-based quantum computation with the error correction of the deviation can be implemented by a series of single-qubit measurements on a cluster states composed of GKP states without squeezed vacuum states.

Threshold of the squeezing level of the GKP qubits

To calculate the squeezing level required for FTQC in the model composed of squeezed vacuum states and GKP qubits, Ref. [4] calculate the error probability for the CZ gate with the sequence of the single-qubit level QEC as shown in Fig. 2.8. In Fig. 2.8, the model with squeezed vacuum states and GKP qubits implements the CZ gate on the input states $|\widetilde{\psi}\rangle$ and $|\widetilde{\phi}\rangle$, followed by two single-qubit level QEC after with the identity gate. The error probability for the CZ gate is the probability that any four single-qubit level QECs fail, considering the operations including the CZ gate. The reason why we focus on the CZ gate is that the CZ gate between the two data qubits is the noisiest gate among the universal gate sets. The thresholds of the squeezing level for FTQC based on the
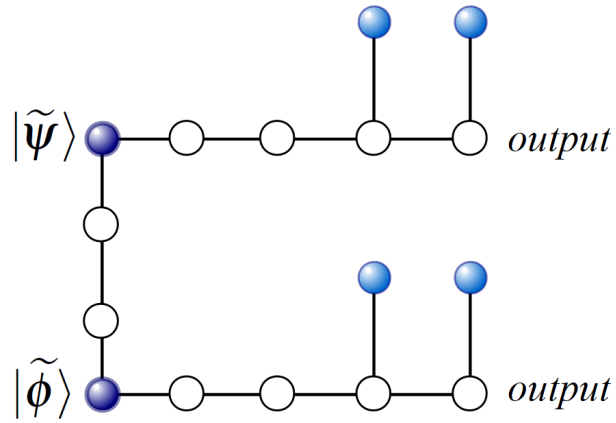
Figure 2.8: A quantum circuit to implement the CZ gate between the data qubits $|\widetilde{\psi}\rangle$ and $|\widetilde{\phi}\rangle$

circuit model are calculated to be about 10^{-6} [17, 18, 15] -10^{-2} [19, 20, 21] depending on the QEC protocols and noise models, which corresponds to the squeezing level 14.8–20.5 dB [4]. When we adopt the 3D cluster state to topologically protected measurement based quantum computation, the threshold squeezing for the model with the squeezed vacuum and GKP qubits is obtained as 16.0 dB.

Chapter 3

Analog quantum error correction

This chapter contains an introduction to the analog quantum error correction and the application for several quantum error correcting codes such as the repetition codes, the concatenated code, and the surface code.

3.1 Analog information and likelihood function

Because quantum states has intrinsically continuous nature, the measurement outcome is also analog information using an appropriate detector such as homodyne and hetelodyne detectors. In the measurement of the GKP qubit using a homodyne detector, we make a decision on the bit value $k(=0,1)$, digital information, from the measurement outcome of the GKP qubit $q_\mathrm{m} = q_k + \Delta_\mathrm{m}$ to minimize the deviation $|\Delta_\mathrm{m}|$, where $q_k(k=0,1)$ is defined as $(2t+k)\sqrt{\pi}(t=0,\pm 1,\pm 2,\cdots.)$ as shown in Fig. 3.1(a). . If we consider only digital information k, as in conventional QEC, we waste the analog information contained in Δ_m. To utilize the analog information, in this chapter, we consider a likelihood function and propose a maximum-likelihood method to improve the QEC performance.

We here define the true deviation $|\bar{\Delta}|$ as the difference between the measurement outcome and true peak value $\bar{q}_k$, that is, $|\bar{\Delta}| = |\bar{q}_k - q_m|$. We consider the following two possible events: one is the correct decision, where the true deviation value $|\bar{\Delta}|$ is less than $\sqrt{\pi}/2$ and equals to $|\Delta_\mathrm{m}|$ as shown in Fig. 3.1(b). The other is the incorrect decision, where $|\bar{\Delta}|$ is greater than $\sqrt{\pi}/2$ and satisfies $|\bar{\Delta}| + |\Delta_m| = \sqrt{\pi}$, as shown in Fig. 3.1(c). Because the true deviation value obeys the Gaussian distribution function $f(\bar{\Delta})$, we can evaluate the probabilities of the two events by

$$f(\overline{\Delta}) = \frac{1}{\sqrt{2\pi\sigma^2}}e^{-\overline{\Delta}^2/(2\sigma^2)}. \tag{3.1}$$

In our method, we regard function $f(\overline{\Delta})$ as a likelihood function. Using this function, the
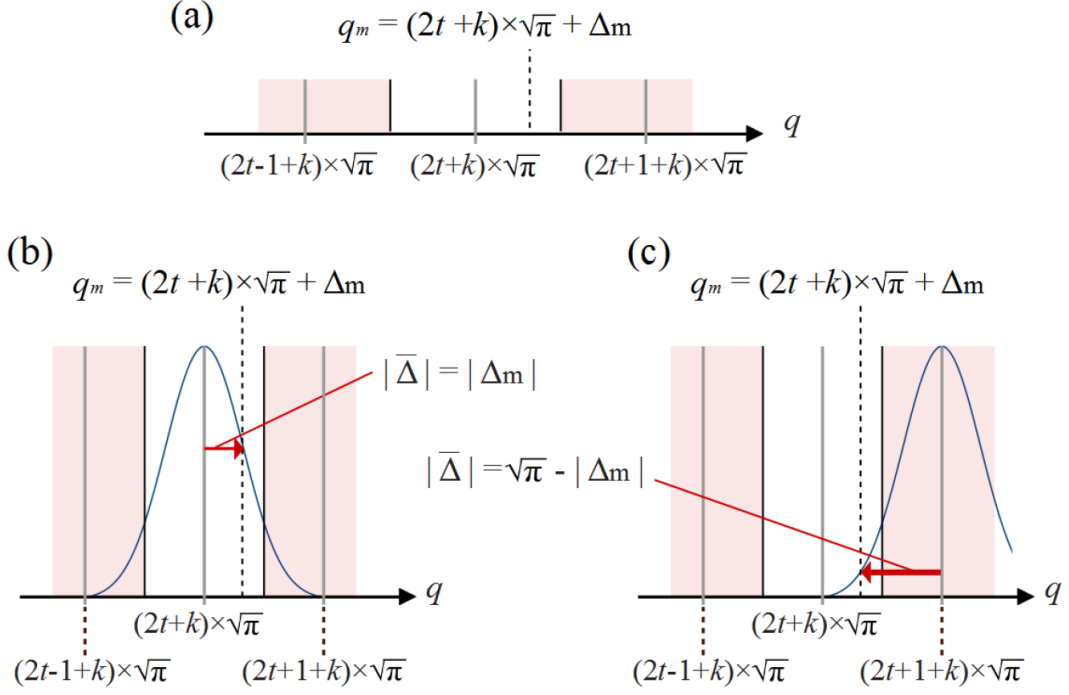
Figure 3.1: Introduction of a likelihood function. (a) Measurement outcome and deviation from the peak value in q quadrature. The dotted line shows the measurement outcome q_{m} equal to $(2t + k)\sqrt{\pi} + \Delta_{\mathrm{m}}$ ($t = 0, \pm 1, \pm 2, \cdots$, $k = 0, 1$), where k is defined as the bit value that minimizes the deviation Δ_{m}. The red areas indicate the area that yields code word $(k + 1) \bmod 2$, whereas the white area denotes the area that yields the codeword k. (b) and (c) Gaussian distribution functions as likelihood functions of the true deviation value $\overline{\Delta}$ represented by the arrows. (b) refers to the case of the correct decision, where the amplitude of the true deviation value is $|\overline{\Delta}| < \sqrt{\pi}/2$, whereas (c) the case of the incorrect decision $\sqrt{\pi}/2 < |\overline{\Delta}| < \sqrt{\pi}$.

likelihood of the correct decision is calculated by

$$f(\overline{\Delta}) = f(\Delta_{\mathrm{m}}). \tag{3.2}$$

The likelihood of the incorrect decision, whose $|\overline{\Delta}|$ is $\sqrt{\pi} - |\Delta_{\mathrm{m}}|$, is calculated by

$$f(\overline{\Delta}) = f(\sqrt{\pi} - |\Delta_{\mathrm{m}}|). \tag{3.3}$$

We can reduce the decision error on the entire code word by considering the likelihood of the joint event and choosing the most likely candidate. Strictly speaking, the likelihood function should be the periodic function including the sum of the Gaussian functions, considering the superposition of the Gaussian states. In this thesis, the likelihood function

is approximated by simple Gaussian functions given by Eqs. (3.2) and (3.3) since the tail of the Gaussian function next to the measurement outcome is small enough to ignore. For example, in the case of the squeezing levels of 1-2 dB and 10 dB, the probabilities that lies between 0 and $\sqrt{\pi}/2$ are about 10^2 and 10^{12} times as large as the probability that lies between 0 and $3\sqrt{\pi}/2$, respectively.

3.2 Introduction to analog quantum error correction

3.2.1 Three-qubit bit-flip code

To provide an insight into our method, we apply the analog QEC to the repetition code. As a simple example, we focus on the three-qubit bit-flip code. In this code, a single logical qubit $|\widetilde{\psi}\rangle_{\mathrm{L}} = \alpha |\widetilde{0}\rangle_{\mathrm{L}} + \beta |\widetilde{1}\rangle_{\mathrm{L}}$, where $|\alpha|^2 + |\beta|^2 = 1$, is encoded into three GKP qubits. The two logical basis states $|\widetilde{0}\rangle_{\mathrm{L}}$ and $|\widetilde{1}\rangle_{\mathrm{L}}$ are defined as

$$|\widetilde{0}\rangle_{\mathrm{L}} = |\widetilde{0}\rangle_1 |\widetilde{0}\rangle_2 |\widetilde{0}\rangle_3 , \quad |\widetilde{1}\rangle_{\mathrm{L}} = |\widetilde{1}\rangle_1 |\widetilde{1}\rangle_2 |\widetilde{1}\rangle_3 , \tag{3.4}$$

respectively. In the QEC with the three-qubit bit-flip code, the error identification for the GKP qubits is substantially different from that for DV-QEC. While the parity of the code qubits is transcribed on the ancilla qubit in DV-QEC, the deviation of the physical GKP qubits is projected onto the deviation of the ancillae.

We explain how the deviation of the physical GKP qubits is projected onto the deviation of the ancillae in the following. Fig.3.2 shows a quantum circuit for the QEC with the three-qubit bit-flip code. This circuit looks almost the same as the circuit for DV apart from the third ancilla qubit. However, the error identification for the GKP qubits is substantially different from that for DV-QEC. In this circuit, the sum of deviations of the physical GKP qubits i and $i+1$ ($i = 1, 2$) are projected onto the ancilla i. The deviation of the physical GKP qubit 3 is projected onto ancilla 3. First, a single logical qubit $|\widetilde{\psi}\rangle_{\mathrm{L}}$ is prepared by two controlled-not (CNOT) gates acting on the data qubit $|\widetilde{\psi}\rangle_1$ $= \alpha |\widetilde{0}\rangle_1 + \beta |\widetilde{1}\rangle_1$ and two ancillae $|\widetilde{0}\rangle_i$ ($i = 2, 3$). The CNOT gate, which corresponds to the operator $\exp(-i\hat{q}_{\mathrm{L}}\hat{p}_{\mathrm{A}})$, transforms

$$\hat{q}_{\mathrm{L}} \quad \rightarrow \quad \hat{q}_{\mathrm{L}}, \qquad \hat{p}_{\mathrm{L}} \rightarrow \hat{p}_{\mathrm{L}} - \hat{p}_{\mathrm{A}} , \tag{3.5}$$

$$\hat{q}_{\mathrm{A}} \quad \rightarrow \quad \hat{q}_{\mathrm{A}} + \hat{q}_{\mathrm{L}}, \quad \hat{p}_{\mathrm{A}} \rightarrow \hat{p}_{\mathrm{A}}, \tag{3.6}$$
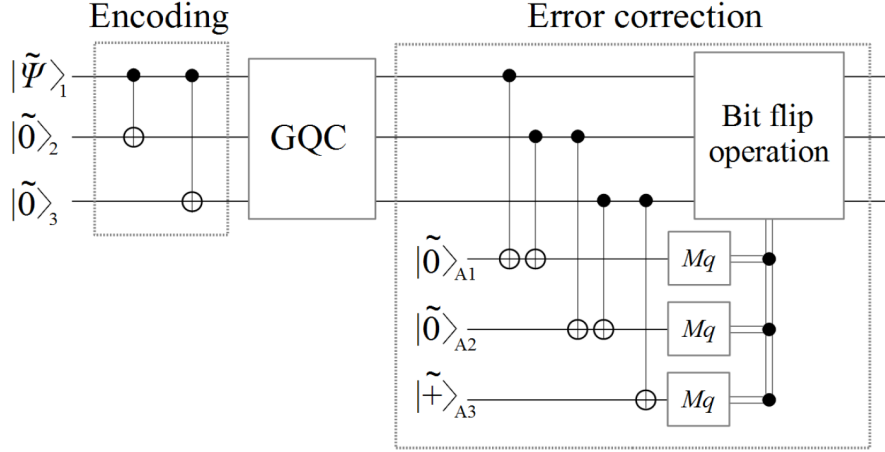
Figure 3.2: A quantum circuit of the QEC for the three-qubit bit-flip code with GKP qubits using the proposed method. The data qubit $|\widetilde{\psi}\rangle_1$ and two GKP qubits $|\widetilde{0}\rangle_2$ and $|\widetilde{0}\rangle_3$ encode a single logical qubit. $|\widetilde{0}\rangle_{A1}, |\widetilde{0}\rangle_{A2},$ and $|\widetilde{+}\rangle_{A3}$ denote ancilla qubits for the QEC. The Gaussian quantum channel and M_q denote the Gaussian quantum channel and measurements of ancillae in q quadrature, respectively.

where $\hat{q}_{\mathrm{L}}$ ($\hat{q}_{\mathrm{A}}$) and $\hat{p}_{\mathrm{L}}$ ($\hat{p}_{\mathrm{A}}$) are the q and p quadrature operators of the logical (ancilla) qubit, respectively. Then, the Gaussian quantum channel displaces the q and p quadratures randomly and independently, and increases the variance of the three physical GKP qubits. After the Gaussian quantum channel, the bit-flip error correction is implemented using the three ancillae $|\widetilde{0}\rangle_{Aj}$ (j=1, 2) and $|\widetilde{+}\rangle_{A3}$. Before the CNOT gates in the error correction circuit, the true deviation values of the physical GKP qubits and ancillae in the q quadrature, which obey Gaussian distribution with mean zero, are denoted by $\overline{\Delta}_j$ and $\overline{\Delta}_{Aj}$ (j=1, 2, 3), respectively. For simplicity, because the ancilla qubits are fresh, we assume that the initial variance is much smaller than that of the physical qubits of the logical qubit. Then, the CNOT gates change the true deviation values of three ancillae $\overline{\Delta}_{Aj}$ in q quadrature as follows:

$$
\begin{aligned}
\overline{\Delta}_{A1} &\rightarrow \overline{\Delta}_{A1} + \overline{\Delta}_1 + \overline{\Delta}_2 = \overline{\Delta}_1 + \overline{\Delta}_2 , \\
\overline{\Delta}_{A2} &\rightarrow \overline{\Delta}_{A2} + \overline{\Delta}_2 + \overline{\Delta}_3 = \overline{\Delta}_2 + \overline{\Delta}_3 , \\
\overline{\Delta}_{A3} &\rightarrow \overline{\Delta}_{A3} + \overline{\Delta}_3 = \overline{\Delta}_3 .
\end{aligned}
\tag{3.7}
$$

Therefore, the sum of deviations of the physical GKP qubits i and $i+1$ ($i = 1,2$) are projected onto the ancilla i. The deviation of physical GKP qubit 3 is projected onto ancilla 3.

From the measurement of the three ancillae in q quadrature, we obtain the outcome $q_{\mathrm{m,A}i} = q_0 + \Delta_{\mathrm{m,A}i}$ ($i = 1, 2$) from ancillae 1 and 2, and $q_{\mathrm{m,A3}} = q_k + \Delta_{\mathrm{m,A3}}$ ($k = 0, 1$) from ancilla 3, under the conditions $\Delta_{\mathrm{m,A}i} \in [-\sqrt{\pi}, \sqrt{\pi}]$ and $\Delta_{\mathrm{m,A3}} \in [-\sqrt{\pi}/2, \sqrt{\pi}/2]$. We then define the values $\delta_1 = \Delta_{\mathrm{m,A1}} - \Delta_{\mathrm{m,A2}} + \Delta_{\mathrm{m,A3}}$ and $\delta_2 = \Delta_{\mathrm{m,A2}} - \Delta_{\mathrm{m,A3}}$. For $i = 1, 2$, if $\delta_i \in [-\sqrt{\pi}, \sqrt{\pi}]$, then we define the values $M_i = \delta_i$. Otherwise, if $\delta_i \in [\sqrt{\pi}, 2\sqrt{\pi}]$, we define the values $M_i = \delta_i - 2\sqrt{\pi}$, and if $\delta_i \in [-2\sqrt{\pi}, -\sqrt{\pi}]$, we define the values $M_i = 2\sqrt{\pi} + \delta_i$. Error identification is executed from M_1 and M_2 as follows. If both $|M_1|$ and $|M_2|$ are smaller than $\sqrt{\pi}/2$, we decide that no error occurs on the logical qubits. Otherwise, we consider two error patterns: one containing a single error, and the other containing double errors. For the first pattern, we presume that the true deviation values $\overline{\Delta}_i$ ($i = 1, 2$) and $\overline{\Delta}_3$ of the qubits in the logical qubit are M_i and $\Delta_{\mathrm{m,A3}}$, respectively. Then, the likelihood of the first pattern F_1 is given by

$$F_1 = f(M_1) f(M_2) f(\Delta_{\mathrm{m,A3}}). \tag{3.8}$$

For the second pattern, if $M_i \in [0, \sqrt{\pi}]$, we presume that $\overline{\Delta}_i$ is $M_i^* = M_i - \sqrt{\pi}$, and if $M_i \in [-\sqrt{\pi}, 0]$, we presume that $\overline{\Delta}_i$ is $M_i^* = M_i + \sqrt{\pi}$. If $\Delta_{\mathrm{m,A3}} \in [0, \sqrt{\pi}/2]$, we presume $\overline{\Delta}_3$ to be $\Delta_{\mathrm{m,A3}}^* = \Delta_{\mathrm{m,A3}} - \sqrt{\pi}$, and if $\Delta_{\mathrm{m,A3}} \in [-\sqrt{\pi}/2, 0]$, we presume that $\overline{\Delta}_3$ is $\Delta_{\mathrm{m,A3}}^* = \Delta_{\mathrm{m,A3}} + \sqrt{\pi}$. Then, the likelihood of the second pattern F_2 is given by

$$F_2 = f(M_1^*) f(M_2^*) f(\Delta_{\mathrm{m,A3}}^*). \tag{3.9}$$

Hence, we can use the likelihood functions $f(|\Delta_{\mathrm{m}}|)$ and $f(\sqrt{\pi} - |\Delta_{\mathrm{m}}|)$ to compare the two error patterns and decide the more likely pattern. For example, if M_1 is in the range $[\sqrt{\pi}/2, \sqrt{\pi}]$, and both M_2 and $\Delta_{\mathrm{m,A3}}$ are in the range $[0, \sqrt{\pi}/2]$, we consider the first error pattern as a single error on qubit 1 of the logical qubit and the second error pattern as double errors on qubits 2 and 3. If $F_1 > F_2$, we decide that the first error pattern occurs, and vice versa. In error identification, the likelihood that $|\overline{\Delta}_i|$ is greater than $\sqrt{\pi}$ is not taken into account because it is always less than $\sqrt{\pi}$ provided $|\overline{\Delta}_i|$ is less than $\sqrt{\pi}$. In the conventional manner, based on majority voting with binary measurement outcomes, the first error pattern is invariably selected because an estimation using only digital information yields a larger probability for a single error than that for double errors.
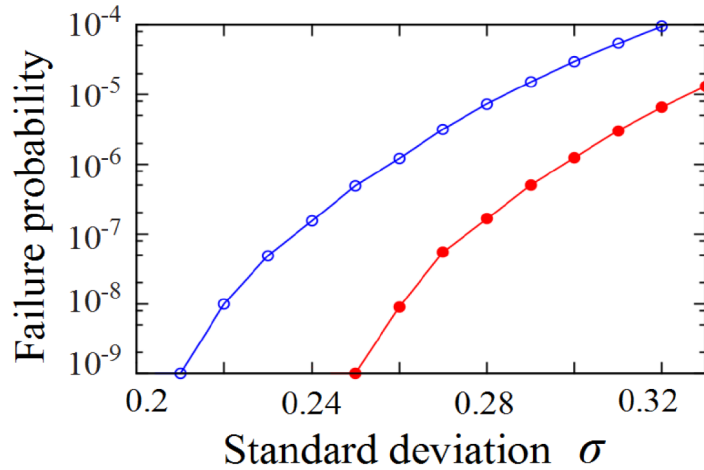
Figure 3.3: Simulation results for the failure probabilities of the three-qubit bit-flip code using the conventional (blue line with open circles) and proposed methods (red line with filled circles).

3.2.2 Numerical results for the three-qubit bit-flip code

We numerically simulated the QEC for the three-qubit bit-flip code using the Monte Carlo method. In this simulation, it is assumed that the encoded data qubit is prepared perfectly, that is, the initial variances of the data qubit and ancillae are zero, and the variances of the GKP qubits of the encoded data qubit increase independently in the Gaussian quantum channel. These assumptions are set to allow a clear comparison between the conventional and proposed methods. In Fig. 3.3, the failure probabilities of the QEC are plotted as a function of the standard deviation of the data qubit after the Gaussian quantum channel. The failure occurs when the assumed error pattern is incorrect. The results confirm that our method suppresses errors more effectively than the conventional method that uses only digital information. To obtain a failure probability less than 10^{-9}, the standard deviation should be less than 0.25 for the proposed method, whereas it needs to be less than 0.21 for the conventional method, which corresponds to the squeezing level of 9.0 dB and 10.6 dB, respectively. This improvement comes from the fact, as mentioned before, that our method can correct double errors, whereas the conventional method corrects only a single error.

3.3 Analog quantum error correction for the concatenated code

3.3.1 C_4/C_6 code

In the following, we demonstrate that the proposed likelihood method improves the error tolerance on a concatenated code, which is indispensable for achieving FTQC. The use of a maximum likelihood method for a concatenated code was proposed with a message-passing algorithm by Poulin [22], and later Goto and Uchikawa [23] for Knill's C_4/C_6 code [19]. However, because previous proposals have been based on the probability of the correct decision given by Eq. (1), the error correction provides a suboptimal performance against the Gaussian quantum channel, as shown later using a numerical calculation.

We apply our method to the C_4/C_6 code modified with a message-passing algorithm proposed by Goto and Uchikawa [23]. The QEC in the C_4/C_6 code is based on quantum teleportation, where the logical qubit $|\widetilde{\psi}\rangle_{\mathrm{L}}$ encoded by the C_4/C_6 code is teleported to the fresh encoded Bell state. The quantum teleportation process refers to the outcome of the Bell measurement on the encoded qubits and determines the amount of displacement. If this feedforward is performed correctly, the error is successfully corrected. From Bell measurement, we obtain the outcomes of both bit values and deviation values for the physical GKP qubits of the encoded data qubit and encoded qubit of the encoded Bell state. Therefore, we can improve the error tolerance of the code by introducing the likelihood method to the Bell measurement.

The error correction in the C_4/C_6 code is based on quantum teleportation, where the logical qubit $|\widetilde{\psi}\rangle_{\mathrm{L}}$ encoded by the C_4/C_6 code is teleported to the fresh encoded Bell state, as shown in Fig.3.4. The quantum teleportation process refers to the outcomes M_p and M_q of the Bell measurement on the encoded qubits, and determines the amount of displacement. We obtain the Bell measurement outcomes of bit values m_{pi} and m_{qi} for the i-th physical GKP qubit of the encoded data qubit and encoded qubit of the encoded Bell state, respectively. In addition to bit values, we also obtain deviation values $\Delta_{p\mathrm{m}i}$ and $\Delta_{q\mathrm{m}i}$ for the i-th physical GKP qubit. Therefore, the proposed likelihood method can improve the error tolerance of the Bell measurement.

As a simple example to explain our method for the Bell measurement, we describe the level-1 C_4/C_6 code, that is, the C_4 code. The C_4 code is the $[[4, 2, 2]]$ code and consists of

four physical GKP qubits to encode a level-1 qubit pair; thus, it is not the error-correcting code but the error-detecting code in the conventional method. The logical bit value of the C_4 code is k (=0,1) when the bit value of the level-1 qubit pair is $(k,0)$ or $(k,1)$, that is, the bit value of the first qubit k defines a logical bit value of a qubit pair. As the parity check of the Z operator for the first and second qubits $ZIZI$ and $IIZZ$ indicates, the bit value of the level-1 qubit pair $(0,0)$ corresponds to the bit value of the physical GKP qubits $(m_{q1}, m_{q2}, m_{q3}, m_{q4})$ = (0,0,0,0) or (1,1,1,1) [19]. The bit values of the pairs (0,1), (1,0), and (1,1) correspond to the bit values of the physical GKP qubits (0,1,0,1) or (1,0,1,0), (0,0,1,1) or (1,1,0,0), and (0,1,1,0) or (1,0,0,1), respectively. Therefore, if the measurement outcome of the physical GKP qubits is (0,0,1,0) for the Z basis, then we consider two error patterns, assuming the level-1 qubit pair (0,0). The first pattern is a single error on the physical qubit 3 and the second pattern is the triple errors on the physical qubits 1, 2, and 4. We then calculate the likelihood for the level-1 qubit pair (0,0) $F_{0,0}$, $F_{0,1}$, $F_{1,0}$, and $F_{1,1}$ as

$$
\begin{aligned}
F_{0,0} &= f(\sqrt{\pi} - |\Delta_{qm1}|)f(\sqrt{\pi} - |\Delta_{qm2}|)f(\Delta_{qm3})f(\sqrt{\pi} - |\Delta_{qm4}|) \\
&+ f(\Delta_{qm1})f(\Delta_{qm2})f(\sqrt{\pi} - |\Delta_{qm3}|)f(\Delta_{qm4}), \quad (3.10)
\end{aligned}
$$

$$
\begin{aligned}
F_{0,1} &= f(|\Delta_{qm1}|)f(\sqrt{\pi} - |\Delta_{qm2}|)f(\sqrt{\pi} - \Delta_{qm3})f(\sqrt{\pi} - |\Delta_{qm4}|) \\
&+ f(\sqrt{\pi} - \Delta_{qm1})f(\Delta_{qm2})f(\sqrt{\pi})f(\Delta_{qm4}), \quad (3.11)
\end{aligned}
$$

$$
\begin{aligned}
F_{1,0} &= f(\sqrt{\pi} - |\Delta_{qm1}|)f(\sqrt{\pi} - |\Delta_{qm2}|)f(\sqrt{\pi} - \Delta_{qm3})f(|\Delta_{qm4}|) \\
&+ f(\Delta_{qm1})f(\Delta_{qm2})f(|\Delta_{qm3}|)f(\sqrt{\pi} - \Delta_{qm4}), \quad (3.12)
\end{aligned}
$$

$$
\begin{aligned}
F_{1,1} &= f(|\Delta_{qm1}|)f(\sqrt{\pi} - |\Delta_{qm2}|)f(\Delta_{qm3})f(\sqrt{\pi} - |\Delta_{qm4}|) \\
&+ f(\sqrt{\pi} - \Delta_{qm1})f(\Delta_{qm2})f(\sqrt{\pi} - |\Delta_{qm3}|)f(\sqrt{\pi} - \Delta_{qm4}), \quad (3.13)
\end{aligned}
$$

respectively. Finally, we determine the level-1 logical bit value for the Z basis by comparing $F_{0,0} + F_{0,1}$ with $F_{1,0} + F_{1,1}$, which refer to the likelihood functions for the logical bit values zero and one, respectively. If $F_{0,0} + F_{0,1} > F_{1,0} + F_{1,1}$, then we determine that the level-1 logical bit value for the Z basis is zero, and vice versa. The level-1 logical bit value for the X basis can be determined by the parity check of the X operator for the first and second qubits $XXII$ and $IXIX$ in a similar manner. In the conventional likelihood method [22, 23] $F_{0,0}$, $F_{0,1}$, $F_{1,0}$, and $F_{1,1}$ are given by the same joint probability

$$
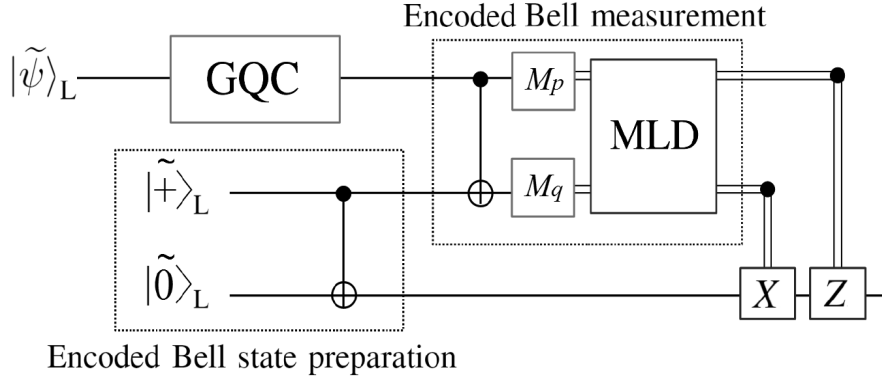p_{\text{corr}}^3(1 - p_{\text{corr}}) + p_{\text{corr}}(1 - p_{\text{corr}})^3, \quad (3.14)
$$

41

Figure 3.4: Error correction by quantum teleportation. The encoded data qubit $|\widetilde{\psi}\rangle_L$, two encoded qubits $|\widetilde{+}\rangle_L$, and $|\widetilde{0}\rangle_L$ are encoded by C_4/C_6 code. Gaussian quantum channel and MLD denote the Gaussian quantum channel and a maximum-likelihood decision, respectively.

where the probability p_{corr} is defined by Eq. (2.77) in Chap. 2. Because $F_{0,0} + F_{0,1} = F_{1,0} + F_{1,1}$, the C_4 code is not error-correcting code but error-detecting code in the conventional method, whereas it is the error-correcting code in our method. For higher levels of concatenation, the likelihood for the level-l ($l \geq 2$) bit value can be calculated by the likelihood for the level-$(l-1)$ bit value in a similar manner.

3.3.2 Numerical calculations for the C_4/C_6 code

We simulated the quantum teleportation process for the C_4/C_6 code with the conventional [23] and proposed method using the Monte Carlo method. In this simulation, it is assumed that the encoded data qubit and encoded Bell state are prepared perfectly, and the variance of the GKP qubits of the encoded data qubit σ^2 increases only by the Gaussian quantum channel. In Fig.3.5, the failure probabilities up to level-5 of the concatenation are plotted as a function of the data qubit's deviation. The results confirm that our method suppresses errors more effectively than the conventional method. It is also remarkable that our method achieves the hashing bound of the standard deviation for the quantum capacity of the Gaussian quantum channel ~ 0.607, which corresponds to the squeezing level of 1.3 dB and has been conjectured to be an attainable value using the optimal method [5, 16]. The quantum capacity is defined as the supremum of all achievable rates at which quantum information can be transmitted over the quantum channel and the hashing bound of the standard deviation is the maximum value of the condition that yields the non-zero positive quantum capacity. By contrast, the concatenated code with only
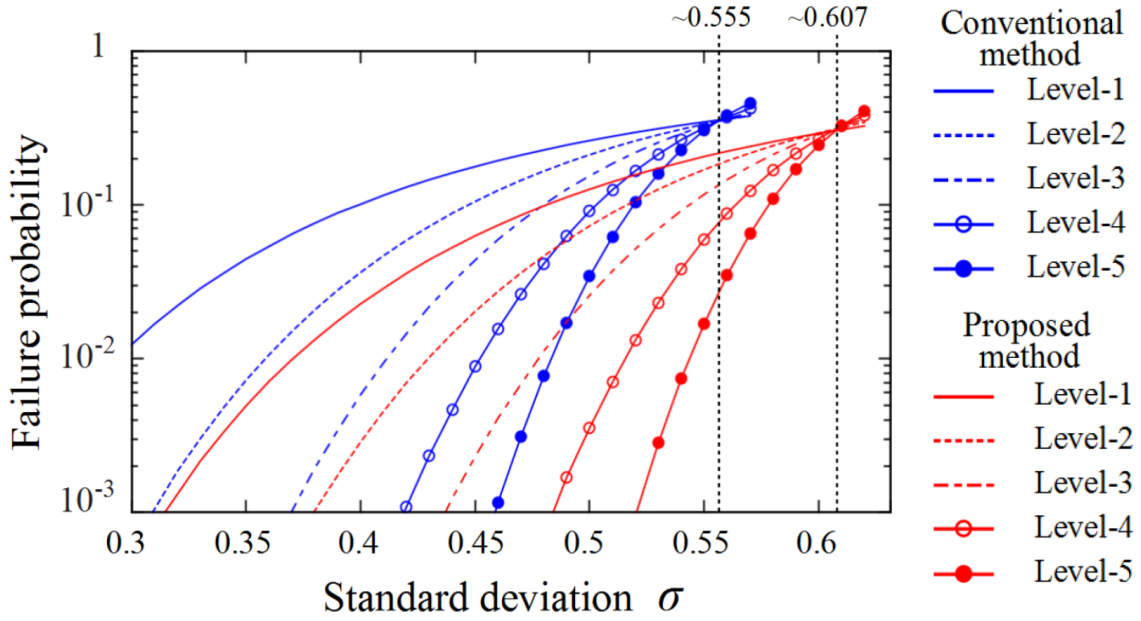
Figure 3.5: Simulation results for the failure probabilities of the C_4/C_6 code using the conventional and proposed method. The failure probabilities using the conventional method (blue line) and proposed method (red line) are represented for the concatenated level-1 (solid), level-2 (dashed), level-3 (dashed-dotted), level-4 (open circles), and level-5 (filled circles).

digital information achieves the hashing bound ~ 0.555 [5, 16], which corresponds to the squeezing level of 2.1 dB. This fact shows our method can lead to reduce the squeezing level required for FTQC.

3.4 Analog error correction with the surface code

3.4.1 Surface code

While the analog QEC has been investigated by using the three-qubit bit-flip code and C_4/C_6 code, its validity on the surface code, which is one of the important candidate for scalable fault-tolerant quantum computation, is still unknown. Here we first investigate the QEC process of a surface code under a code capacity noise model, where the QEC is operated with ideal syndrome measurements. In the code capacity noise model, the encoded state is constructed from the single GKP qubit of an infinite squeezing, and after the construction process the Gaussian quantum channel decreases the squeezing level of the GKP qubits except for the syndrome qubits. Later we will extend to the phenomeno-logical noise model, where the encoded state is constructed from the single GKP qubit of an infinite squeezing, and the Gaussian quantum channel decreases the squeezing level of not only the data qubits but the syndrome qubits.

We here investigate the QEC process of a surface code with the code capacity model to verify whether analog QEC with the surface code can provide an optimal perfor-mance against the Gaussian quantum channel, since we employ topologically protected measurement-based quantum computation to implement FTQC. For the QEC, we employ the minimum distance decoding, which can be done by finding a minimum path connect-ing pairs of vertices. In the numerical simulations of the QEC process of a surface code with the $L \times L$ lattice, we use a minimum-weight perfect matching algorithm [24, 25]. In the minimum-weight perfect matching algorithm, we estimate the most likely location of the errors from the possible locations provided by vertices on the graph. In the digital QEC, the weight is calculated from a distance of the vertices. On the other hand, in the anlog QEC, a weight is calculated by using a likelihood as

$$l_{\mathrm{in}} \quad = \quad -\log\left[f(|\Delta_{\mathrm{m}}|)/f(\sqrt{\pi} - |\Delta_{\mathrm{m}}|)\right], \tag{3.15}$$

where and l_{in} is a likelihood for the incorrect decision. In Fig.2, the logical error proba-bilities are plotted as a function of the standard deviation of the GKP qubits for the code distances $d = 5, 7, 9, \cdots$.

3.4.2 Surface code with a code capacity noise model

To obtain the threshold value of the surface codes with the digital QEC and the analog QEC, the finite-size scaling ansatz similar to Ref. [26, 27] was used. In the scaling, the logical error probability $P_L = A + B(p - p_{th})L^{1/v}$ was used for the fitting function, where A, B, p_{th}, and v are the fitting parameters. The results in Fig. 3.6 confirm that our method can reduce the logical error probability. This indicates that the analog QEC also achieves ~ 0.607 close to the hashing bound of the quantum capacity of the Gaussian quantum channel. On the other hand, the digital QEC with only binary information achieves ~ 0.540. This implies that the analog QEC with the surface code provides an optimal performance against Gaussian quantum channel.

3.4.3 Surface code with a phenomenological noise model

Next, we simulate the QEC process of topologically protected measurement-based quantum computation with the surface code [10, 11, 28, 29] under a phenomenological noise model. We here investigate the QEC process on the 3D cluster state. There are the primal and dual cubes, faces, and edges in a unit cell of the 3D cluster state. In topological QEC on the 3D clsuter state, if there is no error, the parity of each six X-basis measurement outcomes on the primal cube is always even. The errors are described by using a dual 1-chain and we estimate the location of errors from a set of odd parity cubes. In Fig. 3.7, the logical error probabilities are plotted as a function of the standard deviation. The results confirm that our method can also suppress errors with the phenomenological noise model, and the threshold for the standard deviation can be improved from 0.41 to 0.47, which corresponds to improvement of the squeezing level from 4.7 dB to 3.5 dB. Hence, analog QEC with the phenomenological noise model can reduce the required squeezing level by 1.2 dB in comparison to the digital QEC.

3.5 Discussion and conclusion

We have proposed a maximum likelihood method which used not only digital information but also analog information for an efficient QEC based on GKP qubits. Numerical results showed our method improved the QEC performance for the three-qubit bit-flip code and concatenated codes. In particular, we provide the first method to achieve the hashing

bound for the quantum capacity of the Gaussian quantum channel. Such a use of analog information has been developed in classical error correction against the disturbance such as an additive white Gaussian noise [30] and identified as an important tool for qubit readout [31, 32]. However, the use of analog information has been left unexploited to improve the QEC performance.

Furthermore, our method can be also applied to various other codes [9, 10, 33, 34, 35]. Therefore, the squeezing level required for FTQC with a non-concatenated code such as surface code which is used to implement topological quantum computation [9, 10] can be reduced using our method. In addition, our method provide highly versatile quantum error correction with continuous variables, because our method can be applied to GKP code, cat code, and other various codes used to digitize continuous variables.

Although several methods to implement GKP qubits have been proposed [36, 37, 38, 39, 40, 41, 42] and the achievable squeezing level of a squeezed vacuum state is 15 dB [43], it is still difficult to experimentally generate GKP qubits with the squeezing level required for FTQC. Our method can alleviate this requirement, and will encourage experimental developments.

Figure 3.6: Simulation results for the logical error probabilities of the surface code with ideal syndrome measurements using (a) the digital QEC and (b) the analog QEC for several distance d which is size of the 3D cluster state. The simulation results for the digital QEC are obtained from 50000 samples. The simulation results for the analog QEC are obtained from 50000 samples (for $d = 5 - 15$) and 10000 samples (for $d = 17 - 25$) .
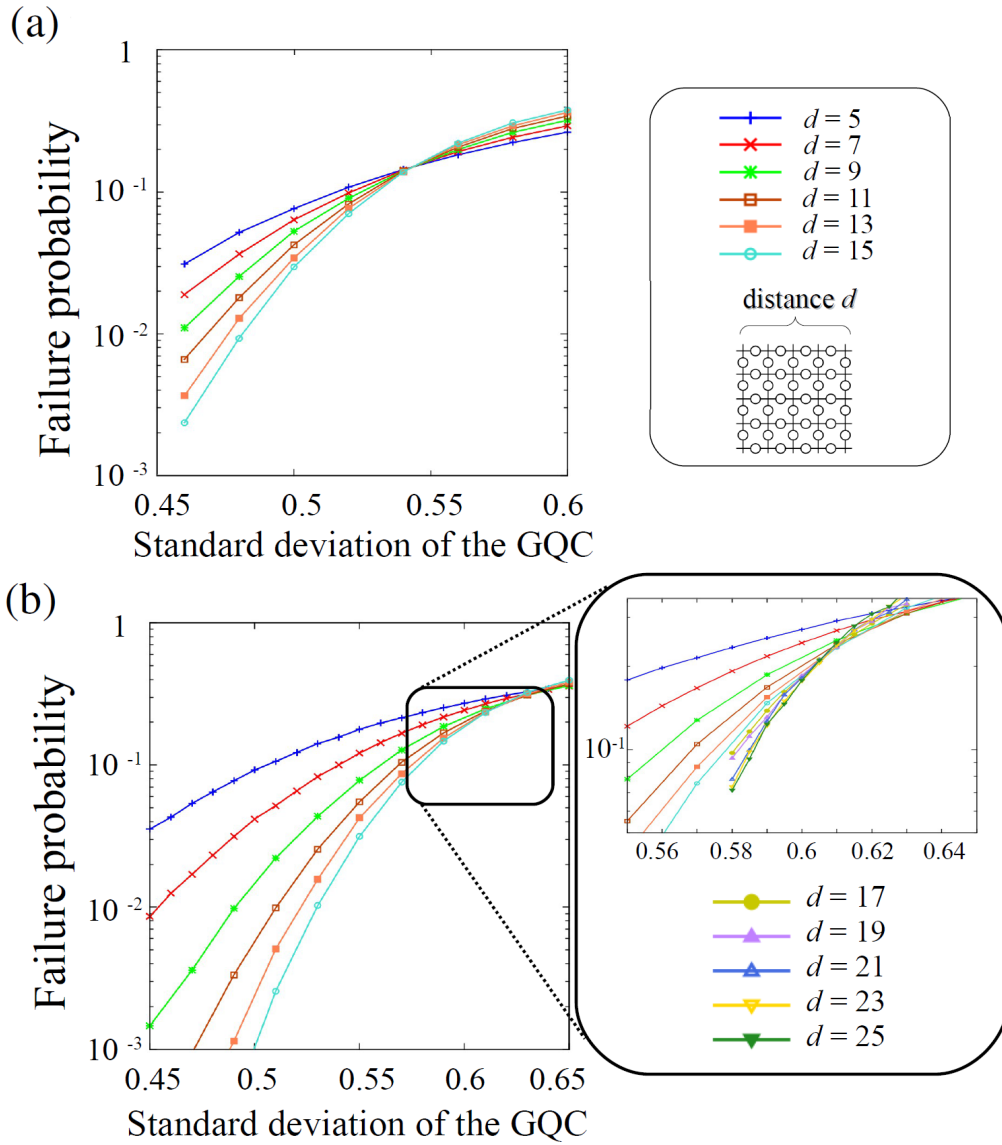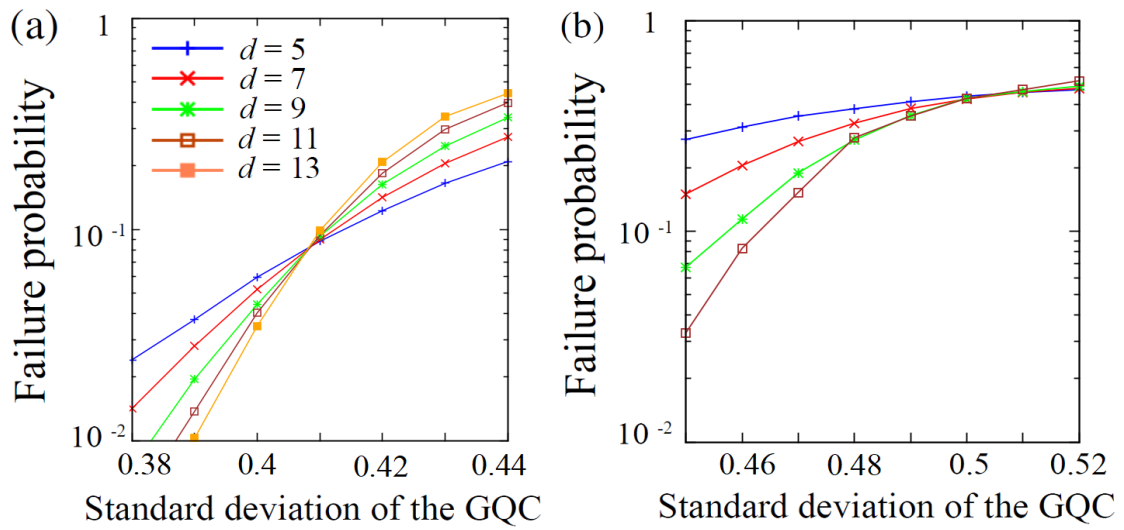
Figure 3.7: Simulation results for the logical error probabilities of the surface code with noisy syndrome measurements using (a) the digital QEC and (b) the analog QEC. The simulation results for the digital QEC are obtained from 50000 samples. The simulation results for the analog QEC are obtained from 10000 samples.

Chapter 4

Toward large-scale quantum computation

Although small-scale quantum computation with various physical systems has been demonstrated, large-scale quantum computation is still a significant experimental challenge for most candidates of physical systems. In this chapter, we propose a method to realize high-threshold FTQC wih the GKP qubits by harnessing analog information contained in the GKP qubit, which can alleviate the required squeezing level for FTQC.

In Sec. 4.1, we briefly review large-scale quantum computation with continuous variable stastes. In Sec. 4.2, we explain the accumulation of errors during the construction of the large-scale cluster states. In Secs. 4.3 and 4.4, we propose the highly-reliable measurement, and present a high-threshold FTQC on the 3D cluster state constructed by using the highly-reliable measurement, respectively. In Sec. 4.5, the required squeezing level is calculated. In the calculation, we first calculate the unheralded error in the leading order for simplicity and then we simulate the analog QEC on the 3D cluster states constructed by using the fusion gate with the highly-reliable measurement. Section 4.6 is devoted to a discussion and conclusion.

4.1 Large-scale quantum computation

Among the candidates, squeezed vacuum states in an optical system have shown great potential for large scale continuous variable quantum computation; in fact, more than one million-mode continuous variable cluster state has been achieved already in an experiment [3]. This ability of entanglement generation comes from the fact that squeezed vacuum states can be entangled by using the time-domain multiplexing approach by only beam splitter coupling to miniaturize optical circuits [44, 45].

Since continuous variable quantum computation itself has an analog nature, it is dif-

ficult to handle the accumulation of analog errors caused, for example, by photon loss during quantum computation [46, 47]. This can be circumvented by encoding digitized variables into continuous variables using an appropriate code, such as Gottesman–Kitaev–Preskill (GKP) code [5]. By digitizing continuous variables, the standard quantum error correcting code can be applied to implement FTQC with continuous variables. Moreover, GKP qubits inherit the advantage of squeezed vacuum states on optical implementation; they can be entangled by only beam splitter coupling. Furthermore, qubit-level Clifford gates on the GKP qubits in measurement-based quantum computation are implemented by Gaussian operation achieved simply by a homodyne measurement on continuous variable cluster states [48]. Menicucci showed that continuous variable-FTQC is possible within the framework of measurement-base quantum com using squeezed vacuum cluster states with GKP qubits [4]. A promising architecture for a scalable quantum circuit has been proposed recently [49, 50], where the GKP qubits are incorporated to perform FTQC. Hence, the GKP qubits will play an indispensable role in implementing continuous variable-FTQC.

Regarding the generation of the GKP qubit, a promising proposal [37] exists to prepare a good GKP qubit in circuit quantum electrodynamics with the squeezing level around 10 dB [51] within the reach of near-term experimental set-up. This implies that large scale quantum computation is possible, if the required squeezing level of the initial single qubit for FTQC is less than 10 dB. Yet, there is a large gap between the experimentally achievable squeezing level and theoretical requirement squeezing level. For example, the existing continuous variable-FTQC requires the squeezing level of both squeezed vacuum state and GKP qubit 14.8–20.5 dB [4] to achieve the fault-tolerant threshold 2×10^{-2} [19, 20, 21] -10^{-6} [17, 18, 15]. Therefore, it is highly desirable to reduce the required squeezing level to around 10 dB to realize the large scale continuous variable-FTQC.

In this work, we propose a high-threshold FTQC to alleviate the required squeezing level for FTQC by harnessing analog information contained in the GKP qubit. The analog information obtained by measuring continuous variable states (including GKP qubits) reflects the effect of noise as a deviation in the measurement outcome. Therefore, it contains beneficial information to improve the error tolerance. The proposed high-threshold FTQC consists of two parts. One is to apply analog QEC [6] to the surface code, which allows us to implement the high-threshold FTQC. The other is a construction of the clus-

ter state for topologically protected measurement-base quantum com [9, 10, 11, 12] with a low error accumulation by using the highly-reliable measurement with the help of analog information. In general, the accumulation of errors on a qubit, which causes degradation of the threshold, increases as the number of the entangling gate increases. In this work, we develop a novel method to avoid this accumulation of errors by using the proposed highly-reliable measurement which harnesses analog information. Accordingly, the required squeezing level for topologically protected measurement-base quantum com with the 3D cluster state constructed by our method can be reduced to 9.8 dB. By contrast, the required squeezing level in the existing continuous variable-FTQC scheme [4] combined with the fault-tolerant scheme with the threshold 0.67×10^{-2} [12] is 16.0 dB. This improvement results from the reduction from 16.0 dB to 9.8 dB corresponds to the reduction of the error probability to misidentify the single GKP qubit in q and p quadrature from 2.7×10^{-15} to 7.4×10^{-5}. By achieving the requirement of the squeezing level around 10 dB, we believe this work can considerably take a step closer to the realization of large-scale quantum computation with digitized continuous variable states and will be indispensable to construct continuous variable-FTQC.

4.2 Accumulation of errors during the construction of the large-scale cluster states

We have investigated the QEC process of topologically protected measurement-base quantum com on the 3D cluster state prepared by the infinitely squeezed GKP qubits in the previous section. In this section, we consider more realistic condition, where the 3D cluster state is constructed from the single GKP qubits of a finite squeezing level by using only the CZ gate. In the following, we refer this noise model to the correlated error model. In the construction of the 3D cluster state by using only the CZ gate, the accumulation of errors on the qubit, which causes degradation of the squeezing level, generally increases as the number of the the CZ gate on the qubit increases. The CZ gate for the GKP qubits, which corresponds to the operator $\exp(-i\hat{q}_C\hat{q}_T)$, transforms

$$\hat{q}_C \to \hat{q}_C, \tag{4.1}$$

$$\hat{p}_C \to \hat{p}_C - \hat{q}_T, \tag{4.2}$$

$$\hat{q}_T \to \hat{q}_T, \tag{4.3}$$

$$\hat{p}_\mathrm{T} \to \hat{p}_\mathrm{T} - \hat{q}_\mathrm{C} \ , \tag{4.4}$$

where $\hat{q}_\mathrm{C}$ ($\hat{q}_\mathrm{T}$) and $\hat{p}_\mathrm{C}$ ($\hat{p}_\mathrm{T}$) are the q and p quadrature operators of the control (target) qubit, respectively.

We here consider the error propagation caused by the CZ gate operation. The CZ gate operation displaces the deviation for the q and p quadrature as

$$\overline{\Delta}_{q,\mathrm{C}} \to \overline{\Delta}_{q,\mathrm{C}}, \tag{4.5}$$

$$\overline{\Delta}_{p,\mathrm{C}} \to \overline{\Delta}_{p,\mathrm{C}} - \overline{\Delta}_{q,\mathrm{T}}, \tag{4.6}$$

$$\overline{\Delta}_{q,\mathrm{T}} \to \overline{\Delta}_{q,\mathrm{T}}, \tag{4.7}$$

$$\overline{\Delta}_{p,\mathrm{T}} \to \overline{\Delta}_{p,\mathrm{T}} - \overline{\Delta}_{q,\mathrm{C}}, \tag{4.8}$$

where $\overline{\Delta}_{q,\mathrm{C}}$ ($\overline{\Delta}_{q,\mathrm{T}}$) and $\overline{\Delta}_{p,\mathrm{C}}$ ($\overline{\Delta}_{p,\mathrm{T}}$) are true deviation values in the q and p quadrature of the control and target qubit, respectively. Since the true deviation obeys Gaussian distribution and takes a value randomly and independently, the variance of the control qubit and target qubit in p quadrature changes as

$$\sigma_{p,\mathrm{C}}^2 \to \sigma_{p,\mathrm{C}}^2 + \sigma_{q,\mathrm{T}}^2, \tag{4.9}$$

$$\sigma_{p,\mathrm{T}}^2 \to \sigma_{p,\mathrm{T}}^2 + \sigma_{q,\mathrm{C}}^2, \tag{4.10}$$

where $\sigma_{q,\mathrm{C}}^2$ ($\sigma_{q,\mathrm{T}}^2$) and $\sigma_{p,\mathrm{C}}^2$ ($\sigma_{p,\mathrm{T}}^2$) are the variance of the control and target qubit in the q and p quadrature, respectively. On the other hand, the variance in the q quadrature does not change. Therefore, the CZ gate increases the probability of misidentifying the bit value in p quadrature. In this work, we define the error propagation caused by the CZ gate operation as the correlated error. Assuming that the variance of the single GKP qubit is σ^2, if the 3D cluster state is prepared straightforwardly by only the CZ gates, the variance of the qubits in the p quadrature become $5\sigma^2$, since the qubit of the 3D cluster state is generated by using the CZ gates between four neighboring qubits. This deteriorates the required squeezing level for the surface code from 4.7 dB under the phenomenological noise model to 13.7 dB under the correlated noise model. In the following, we propose the highly-reliable measurement to avoid the accumulation of the errors, which allows us to achieve a high threshold.

(a) Gaussian distribution $\sqrt{\pi}/2$

$(2k+1)\sqrt{\pi}$ $2k\sqrt{\pi}$ $(2k+1/2)\sqrt{\pi}$

(b) $|v_{up}|\ (<\sqrt{\pi}/2)$

The upper limit

$(2k+1)\sqrt{\pi}$ $2k\sqrt{\pi}$ $(2k+1/2)\sqrt{\pi}$

: The probability that we correctly detect a bit value.

: The probability that we incorrectly detect a bit value.

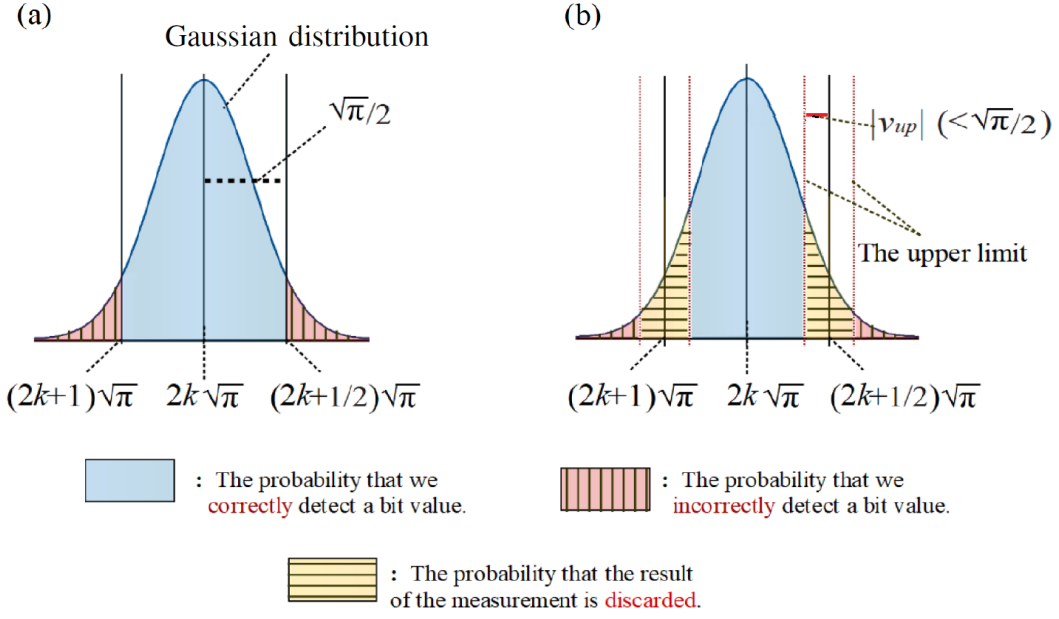: The probability that the result of the measurement is discarded.

Figure 4.1: Introduction of the highly-reliable measurement. (a) The conventional measurement of the GKP qubit, where the Gaussian distribution followed by the deviation of the GKP qubit that has variance σ^2. The plain (blue) region and the region with vertical (red) line represent the different code word $(k-1)\bmod 2$ and $(k+1)\bmod 2$, respectively. The vertical line regions correspond to the probability of incorrect decision of the bit value. (b) The highly-reliable measurement. The shown dot line represents a upper limit v_{up}. The horizontal line areas show the probability that the results of the measurement is discarded by introducing v_{up}. The vertical line areas show the probability that our method fails.

4.3 Highly-reliable measurement

We propose the highly-reliable measurement that utilizes analog information, and explain a method to generate an entanglement between the qubits by using the highly-reliable measurement, avoiding the accumulation of errors during the construction process. Following Ref. [52], we call this entanglement generation with the highly-reliable measurement as the fusion gate. As we mentioned, in the measurement of the GKP qubit, we make a decision on the bit value $k(=0,1)$ from the measurement outcome of the GKP qubit $q_{\mathrm{m}} = q_k + \Delta_{\mathrm{m}}$. The conventional decision sets an upper limit for $|\Delta_m|$ at $\sqrt{\pi}/2$, and assigns the bit value $k = (2t+k)\sqrt{\pi}$. The decision is correct as long as the amplitude of the true deviation $|\overline{\Delta}|$ falls between 0 and $\sqrt{\pi}/2$. The probability to obtain the correct bit value is thus given by p_{corr} in Eq. (2.77). The proposed decision sets an upper limit at $v_{up}(< \sqrt{\pi}/2)$ to give the maximum deviation that will not cause incorrect measurement

of the bit value as shown in Fig. 4.1. If the above condition $|\Delta_m| < v_{up}$ is not satisfied, we discard the result. Since the measurement error occurs when $|\bar{\Delta}|$ exceeds $|\sqrt{\pi}/2 + v_{up}|$, the error probability decreases as increasing v_{up} at the cost of the success probability of the measurement. The probability to obtain the correct bit value with the highly-reliable measurement P_{post} is equal to $P_{post}^{cor}/(P_{post}^{cor} + P_{post}^{in})$, where P_{post}^{cor} is the probability that the true deviation $|\bar{\Delta}|$ falls in the correct area, and P_{post}^{in} is the probability that the true deviation $|\bar{\Delta}|$ falls in the incorrect area. P_{post}^{cor} and P_{post}^{in} for the GKP qubit of the variance σ^2 are given by

$$P_{post}^{cor} = \sum_{k=-\infty}^{+\infty} \int_{2k\sqrt{\pi}-\frac{\sqrt{\pi}}{2}+v_{up}}^{2k\sqrt{\pi}+\frac{\sqrt{\pi}}{2}-v_{up}} dx \frac{1}{\sqrt{2\pi\sigma^2}} e^{-\frac{x^2}{2\sigma^2}} \tag{4.11}$$

and

$$P_{post}^{in} = \sum_{k=-\infty}^{+\infty} \int_{(2k+1)\sqrt{\pi}-\frac{\sqrt{\pi}}{2}+v_{up}}^{(2k+1)\sqrt{\pi}+\frac{\sqrt{\pi}}{2}-v_{up}} dx \frac{1}{\sqrt{2\pi\sigma^2}} e^{-\frac{x^2}{2\sigma^2}}. \tag{4.12}$$

In Fig. 4.2, we plot the probability to misidentify the bit value with the highly-reliable measurement $E_{post} = 1 - P_{post}$ and the success probability of the post-selection $P_{Suc} = P_{post}^{cor} + P_{post}^{in}$ as a function of the squeezing level for several v_{up}. As an example, we described the measurement on the qubit of the variance $3\sigma^2$, which is frequently occurred in the Bell measurement during the construction process. Fig. 4.2 shows that both the error probability E_{post} and the success probability P_{Suc} decrease. In our method, we apply the highly-reliable measurement with $v_{up} = 2\sqrt{\pi}/5$ to the 3D cluster states construction to prevent the deviation of the GKP qubit from propagating the qubit-level error derived from the fusion gate. Because of the highly-reliable measurement, the operation such as the fusion gate becomes nondeterministic. This will be also handled by the so called divide and conquer approach [53, 54] below.

4.4 Construction of the 3D cluster state

We explain how to apply the highly-reliable measurement to prevent the squeezing level from decreasing during the construction of the 3D cluster state. Hereafter, we omit "GKP" of the GKP qubit and simply call it as a qubit. In our method, there are four steps. In step 1, we prepare a node qubit and two leaf qubits of the variance σ^2 in the q and p quadrature (Fig. 4.3 (a)). By using the CZ gate we obtain 3-tree cluster state composed of a node qubit and two leaf qubits, where the the variance of the node and leaf qubits in the p quadrature increase from σ^2 to $3\sigma^2$ and $2\sigma^2$, respectively. On the other hand, the
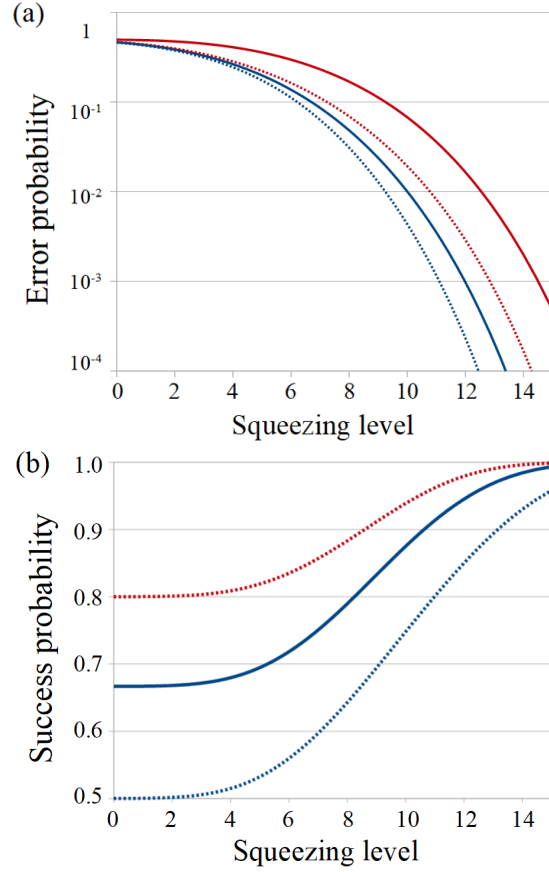
Figure 4.2: The error probabilities of the highly-reliable measurement E_{post} and the success probabilities of the highly-reliable measurement P_{Suc} on the qubit of the variance $3\sigma^2$. (a) The error probabilities with the method using the only CZ gate and our method using the highly-reliable measurement for the upper limit $v_{up} = 0$ (red solid), $v_{up} = \sqrt{\pi}/10$ (red dashed), $v_{up} = \sqrt{\pi}/6$ (blue solid), and $v_{up} = \sqrt{\pi}/4$ (blue dashed), respectively. (b) The success probability for our method. The squeezing level is equal to $-10\log_{10}6\sigma^2$.

variance of the node and leaf qubits in the q quadrature keep the variance σ^2.

In step 2, we operate the single-qubit level QEC [5, 55, 56] by using the CNOT gate with the highly-reliable measurement (Fig. 4.3 (b)). In this single-qubit level QEC, the additional single ancilla qubit is entangled with the node qubit by using the CNOT gate, assuming the node qubit is the target qubit. The ancilla qubit is prepared in the state $|\widetilde{0}\rangle$ to prevent us from identifying the bit value of the node qubit. The CNOT gate, which corresponds to the operator $\exp(-i\hat{q}_C\hat{p}_T)$, transforms

$$\hat{q}_C \rightarrow \hat{q}_C, \tag{4.13}$$

$$\hat{p}_C \rightarrow \hat{p}_C - \hat{p}_T, \tag{4.14}$$

$$\hat{q}_{\mathrm{T}} \to \hat{q}_{\mathrm{T}} + \hat{q}_{\mathrm{C}}, \tag{4.15}$$

$$\hat{p}_{\mathrm{T}} \to \hat{p}_{\mathrm{T}}, \tag{4.16}$$

Regarding the deviation, the CNOT gate operation displaces the deviation for the q and p quadrature as

$$\overline{\Delta}_{q,\mathrm{C}} \to \overline{\Delta}_{q,\mathrm{C}}, \tag{4.17}$$

$$\overline{\Delta}_{p,\mathrm{C}} \to \overline{\Delta}_{p,\mathrm{C}} - \overline{\Delta}_{p,\mathrm{T}}, \tag{4.18}$$

$$\overline{\Delta}_{q,\mathrm{T}} \to \overline{\Delta}_{q,\mathrm{T}} + \overline{\Delta}_{q,\mathrm{C}}, \tag{4.19}$$

$$\overline{\Delta}_{p,\mathrm{T}} \to \overline{\Delta}_{p,\mathrm{T}}. \tag{4.20}$$

After the CNOT gate, we measure the ancilla qubit in the p quadrature and obtain the deviation of the ancilla qubit $\Delta_{\mathrm{m}p,\mathrm{a}}$. In the single-qubit level QEC, if $|\Delta_{\mathrm{m}p,\mathrm{a}}| = |\overline{\Delta}_{p,\mathrm{a}} - \overline{\Delta}_{p,\mathrm{n}}|$ is less than $\sqrt{\pi}/2$, the true deviation value of the node qubit in the p quadrature changes from $\overline{\Delta}_{p,\mathrm{n}}$ to $\overline{\Delta}_{p,\mathrm{a}}$ after the displacement operation, which displaces $\overline{\Delta}_{p,\mathrm{n}}$ by $\Delta_{\mathrm{m}p,\mathrm{a}}(= \overline{\Delta}_{p,\mathrm{a}} - \overline{\Delta}_{p,\mathrm{n}})$. On the other hand, if $|\overline{\Delta}_{p,\mathrm{a}} - \overline{\Delta}_{p,\mathrm{n}}|$ is more than $\sqrt{\pi}/2$, the bit error in the p quadrature occurs after the displacement operation. This error can be reduced by the highly-reliable measurement on the ancilla defined as follows: if $|\Delta_{\mathrm{m}p,\mathrm{a}}|$ is less than v_{up}, we then operate the displacement to the node qubit in the p quadrature by $\Delta_{\mathrm{m}p,\mathrm{a}}$. Otherwise, we discard the resultant 3-tree cluster state and restart the procedure from step 1. The error probability of the single-qubit level QEC E_{SQE} is given by E_{post} defined in the previous section with the variance of $4\sigma^2$, since after the CNOT gate the true deviation of the ancilla qubit in the p quadrature $|\overline{\Delta}_{p,\mathrm{a}} - \overline{\Delta}_{p,\mathrm{n}}|$ obeys Gaussian distribution with the variance $4\sigma^2$, where $4\sigma^2$ comes from the node qubit and σ^2 from the ancilla qubit. To summarize, the single-qubit level QEC can reduce the variance of the node qubit in the p quadrature from $3\sigma^2$ to σ^2, since $\overline{\Delta}_{p,\mathrm{a}}$ and $\overline{\Delta}_{p,\mathrm{n}}$ obey Gaussian distributions with the variances $3\sigma^2$ and σ^2, respectively. The variance of the node qubit in the q quadrature after the single-qubit level QEC increases from σ^2 to $2\sigma^2$, since the true deviation $\overline{\Delta}_{p,\mathrm{n}} + \overline{\Delta}_{q,\mathrm{a}}$ obeys Gaussian distribution with the variance $2\sigma^2$, where the $\overline{\Delta}_{p,\mathrm{n}}$ and $\overline{\Delta}_{q,\mathrm{a}}$ are the true deviation of the node qubit and the ancilla qubit, respectively. This increase in the variance in q quadrature has no effect on the threshold value, whereas the unheralded error in the p quadrature affects it.

In step 3, we increase the number of the leaf qubits of the tree cluster state by using

the fusion gate with the highly-reliable measurement. The fusion gate can avoid the deviation of the qubit from increasing and the highly-reliable measurement can prevent the qubit-level error from propagating during constructing the 6-tree cluster state, which we call the hexagonal cluster state. We describe the construction of the 4-tree cluster state in detail as follows. By using the fusion gate, we construct the 4-tree cluster state from the two 3-tree cluster states, one of which is corrected by the single-qubit level QEC and the other is uncorrected (Fig. 4.3 (c)). In the fusion gate, the Bell measurement with the highly-reliable measurement is implemented by beam splitter coupling and homodyne measurement. Then feedforward is operated according to the homodyne measurement outcomes on the leaf and the node qubits, respectively. If the misidentification of the bit value of the leaf or node qubits occurs, the feedforward operation propagates the qubit-level error in the 4-tree cluster. The probabilities to misidentify the bit value of the leaf and node qubits are the probabilities to misidentify the bit value of the qubit of the variances $3\sigma^2$ and $4\sigma^2$, respectively. This unheralded qubit-level error can be reduced by using the highly-reliable measurement. We define the unheralded errors on the leaf qubits and node qubits with the highly-reliable measurement as $E_{\text{post}}(3\sigma^2)$ and $E_{\text{post}}(4\sigma^2)$, respectively. The error probabilities $E_{\text{post}}(3\sigma^2)$ and $E_{\text{post}}(4\sigma^2)$ are given by E_{post} defined in the previous section with the variance of $3\sigma^2$ and $4\sigma^2$, respectively.

To evaluate the variances of the leaf and node, we describe the process of the beam splitter coupling in the following. The 50:50 beam splitter coupling between the leaf qubit of the 3-tree cluster state after the single-qubit level QEC and the node qubit of the 3-tree cluster state without the single-qubit level QEC transforms the variables of the leaf and node qubits in the q and p quadrature as

$$\hat{q}_{\text{leaf}} \rightarrow (\hat{q}_{\text{leaf}} + \hat{p}_{\text{node}})/\sqrt{2}, \tag{4.21}$$

$$\hat{p}_{\text{leaf}} \rightarrow (\hat{p}_{\text{leaf}} + \hat{q}_{\text{node}})/\sqrt{2}, \tag{4.22}$$

$$\hat{q}_{\text{node}} \rightarrow (\hat{q}_{\text{leaf}} - \hat{p}_{\text{node}})/\sqrt{2}, \tag{4.23}$$

$$\hat{p}_{\text{node}} \rightarrow (\hat{p}_{\text{leaf}} - \hat{q}_{\text{node}})/\sqrt{2}, \tag{4.24}$$

where $\hat{q}_{\text{leaf}}$ ($\hat{q}_{\text{node}}$) and $\hat{p}_{\text{leaf}}$ ($\hat{p}_{\text{node}}$) the variables of the leaf (node) qubit in the q and p quadrature, respectively. After the coupling, the variances of the leaf qubit in the q and p quadrature changes as $\sigma^2 \rightarrow 2\sigma^2$ and $2\sigma^2 \rightarrow 3\sigma^2/2$, respectively. The variances of the node qubit in the q and p quadrature changes as $\sigma^2 \rightarrow 3\sigma^2/2$ and $3\sigma^2 \rightarrow 2\sigma^2$, respec-

tively. After the homodyne measurement on the leaf and node qubit in the p quadrature, the measurement outcome of the leaf and node qubit in the p quadrature are rescaled by multiplying the measurement outcome by $\sqrt{2}$ in a post-process as $(p_{\text{leaf}} + q_{\text{node}})/\sqrt{2} \rightarrow p_{\text{leaf}} + q_{\text{node}}$ and $(p_{\text{leaf}} - q_{\text{node}})/\sqrt{2} \rightarrow p_{\text{leaf}} - q_{\text{node}}$, respectively. The variances of the leaf and node qubits in the p quadrature changes as $3\sigma^2/2 \rightarrow 3\sigma^2$ and $2\sigma^2 \rightarrow 4\sigma^2$, respectively. Therefore, the probabilities to misidentify the bit value of the leaf and node qubits in the p quadrature are the probabilities to misidentify the bit value of the qubit of the variances $3\sigma^2$ and $4\sigma^2$, respectively.

We can reduce the misidentifying error probabilities occurred in the construction of the hexagonal cluster state in the same way. We generate the 5-tree cluster state from the 3-tree cluster states and the 4-tree cluster state by using fusion gate with the highly-reliable measurement on the leaf qubit of the 3-tree cluster state and the node qubit of the 4-tree cluster state with the highly-reliable measurement (Fig. 4.3 (d)). Finally, we construct the hexagonal cluster state from the six 5-tree cluster states with the highly-reliable measurement on the Bell measurement between leaf qubits (Fig. 4.3 (e)).

In step 4, we generate the 3D cluster state deterministically. Hence, the highly-reliable measurement can not be used and the 3D cluster state is generated from the hexagonal cluster states by using the fusion gate with the highly-reliable measurement between the leaf qubits of the neighboring hexagonal cluster states without the highly-reliable measurement (Fig. 4.3 (f)). In this step, the unheralded error, which corresponds to the probability to misidentify the bit value of the qubit of the variance $3\sigma^2$, accumulates on the node qubits. We define this error probability as E_{Bell}. We can eventually obtain the 3D cluster state composed of the node qubits whose variance and squeezing level in the p quadrature are σ^2 and $-10\log_{10}2\sigma^2$, respectively.

By contrast, the conventional method, where the fusion gate with the highly-reliable measurement is not used and the 3D cluster state is generated by using only the CZ gate between neighboring nodes, yields the variance $5\sigma^2$ and the squeezing level $-10\log_{10}10\sigma^2$ of node qubits in the p quadrature, respectively. Therefore, the single-qubit level QEC and the fusion gate with highly-reliable measurement can avoid the degradation of the squeezing level during the construction of the 3D cluster state. This relaxes the requirement on the squeezing level of the initial single qubit considerably as will be calculated in the next section.
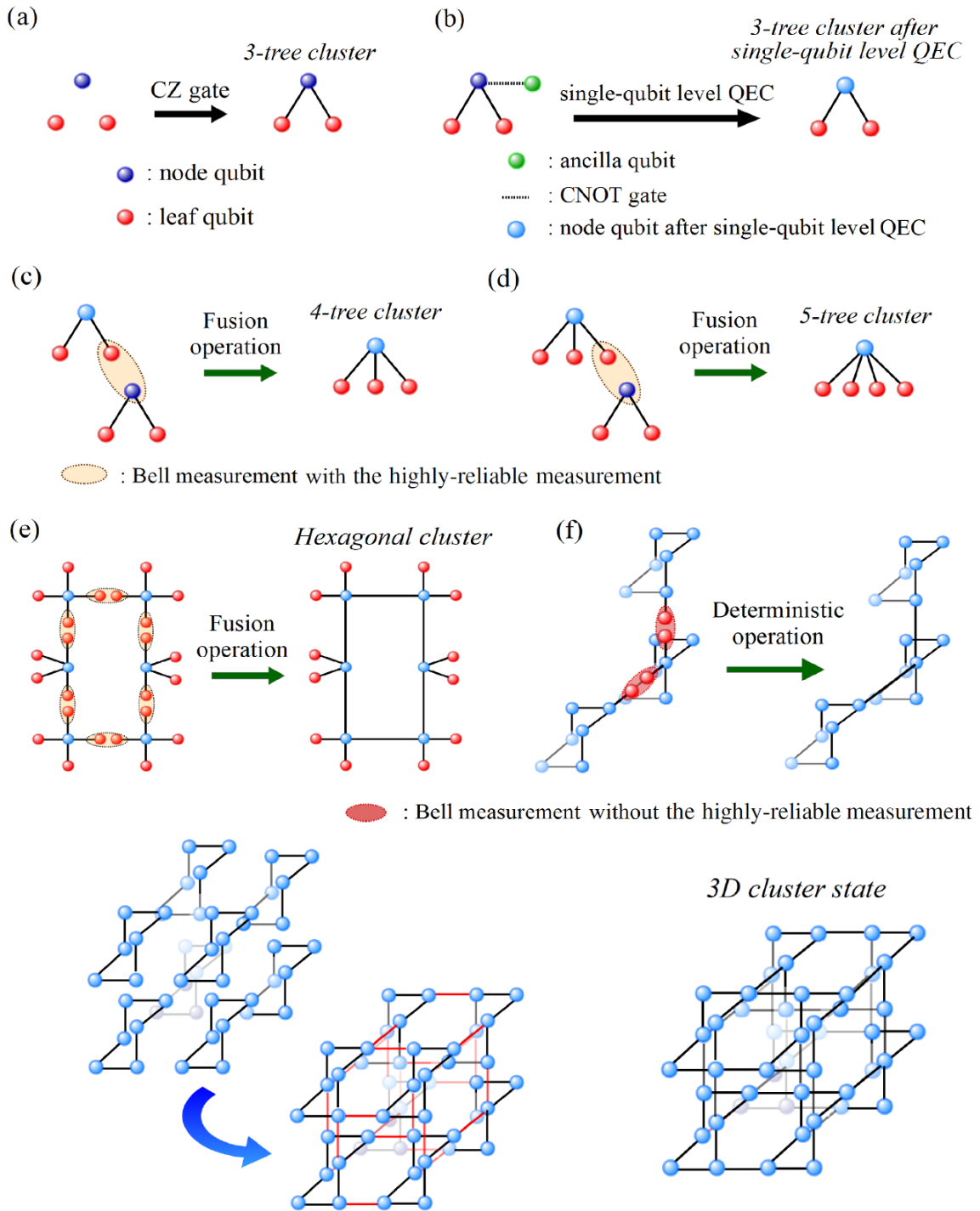
Figure 4.3: The 3D cluster state construction. (a) The preparation of the 3-tree cluster state by using the CZ gate. (b) The single-qubit level QEC using the additional ancilla qubit with the highly-reliable measurement. (c)–(e) The construction of the hexagonal cluster state from the 3-tree qubit with the highly-reliable measurement. (f) The construction of the 3D cluster state from the hexagonal cluster states, where the entanglement is generated between the neighboring hexagonal cluster states without the highly-reliable measurement.

4.5 Threshold calculation for TMBC

In this section, we calculate the threshold value for the 3D cluster state prepared by using the highly-reliable measurement. In this calculation, it is assumed that the 3D cluster state is prepared using the proposed method with the qubit of the variances finite value σ^2 in q and p quadrature, that is, the initial variances of the qubit before the CZ gate in Fig. 4.3 (a) are σ^2 in q and p quadrature.

We define the unheralded error probability E_{tot} per one node qubit of the 3D cluster state in the p quadrature. The E_{tot} results from four causes, which correspond to the error originated from the node qubit itself, the unheralded errors during highly-reliable measurements in steps 2 and 3, and the error during the deterministic fusion gate in step 4. The unheralded error of the node qubit itself E_{node} occurs, when the magnitude of the true deviation value of the node qubit is more than $\sqrt{\pi}/2$. The error probability E_{node} is given by E_{post} with the variance in p quadrature σ^2. The unheralded error probability in the single-qubit level QEC (step 2) E_{SQE} is given by E_{post} with the variance in p quadrature $4\sigma^2$. The unheralded errors during highly-reliable measurements occurs in the two processes of step 3. One is in the 4- and 5-tree cluster states construction by using the Bell measurement shown in Fig. 4.3 (c) and (d). The probabilities of misidentifying the bit value on the node qubit in the Bell measurement are both $E_{\text{post}}(4\sigma^2)$ given by E_{post} with the variance in p quadrature $4\sigma^2$. The other unheralded error process of the highly-reliable measurement in step 3 is the bit value misidentification on the leaf qubits by using the fusion gate in Fig. 4.3 (c)-(e). The error probability $E_{\text{post}}(3\sigma^2)$ is given by E_{post} with the variance in p quadrature $3\sigma^2$. The measurement error in the deterministic entanglement generation between neighboring node qubits occurs in the Bell measurement between the leaf qubits of the hexagonal cluster states without the highly-reliable measurement (Fig. 4.3 (f)). This unheralded error probability E_{Bell} corresponds to the probability of misidentifying the bit value on the qubit of the variance $3\sigma^2$ without the highly-reliable measurement. This process requires two Bell measurements per one node qubit as shown in Fig. 4.3 (f)

For simplicity, we firstly calculate the E_{tot} in the leading order. Later we will take more detailed calculation by the simulation of the QEC for topologically protected measurement-base quantum com by using the minimum-weight perfect matching algorithm.

The error probability E_{tot} in the leading order can be obtained as

$$\begin{aligned}
E_{\text{tot}} &= E_{\text{node}}(\sigma^2) + E_{\text{SQE}} + 6 \times E_{\text{post}}(3\sigma^2) \\
&+ 2 \times E_{\text{post}}(4\sigma^2) + 2 \times E_{\text{Bell}}.
\end{aligned} \tag{4.25}$$

We estimated the required squeezing level for continuous variable-FTQC in the leading order as follows. Let us first consider the case without analog QEC. By virtue of the highly-reliable measurements, the correlated error probability on the 3D cluster state is now very small and can be neglected safely. In fact, for around 10 dB squeezing with $v_{up} = 2\sqrt{\pi}/5$, the unheralded error probability $E_{\text{post}}(3\sigma^2)$ and $E_{\text{post}}(4\sigma^2)$ is order of 10^{-5} and 10^{-4}, which is much smaller than the unheralded error probability E_{Bell} of about 1.5 %. Hence, since we can ignore the correlated errors on the 3D cluster state, the error probability E_{tot} can be fairly well characterized by the single parameter σ^2 under the phenomenological noise model, where the required squeezing level for topologically protected measurement-base quantum com is 2.9-3.3% [27, 57]. We define the required squeezing level as the squeezing level that provides $E_{tot} = 3.0\%$, and the numerical calculation in the leading order without analog QEC yields the required squeezing level of 10.5 dB with $v_{up} = 2\sqrt{\pi}/5$. We can further improve the tolerable standard deviation by using analog QEC. In Chap.3, we numerically simulated the improvement of the topologically protected measurement-base quantum computation performance in the analog QEC with the phenomenological noise model, and obtained the improvement on the required squeezing level by 1.2 dB in comparison to the digital QEC. Hence, we can obtain the required squeezing level 9.3 dB in the leading order with analog QEC.

To proceed to the detailed calculation of E_{tot}, we simulate the QEC for topologically protected measurement-base quantum com by using the minimum-weight perfect matching algorithm. In Fig. 4.4, the logical error probabilities are plotted as a function of the standard deviation. The results confirm that our method can also suppress errors with the independent error model, and the threshold for the standard deviation can be improved from 0.208 to 0.228, which corresponds to squeezing level from 10.6 dB to 9.8 dB. In the numerical calculation, we set the upper limit v_{up} to $2\sqrt{\pi}/5$ in order to adopt the independent error model. Therefore, continuous variable-FTQC with analog QEC and the highly-reliable measurement can improve the required squeezing level for topologically protected measurement-base quantum com by 6.2 dB in comparison to the existing

scheme for continuous variable-FTQC [4].

Resource requirement

Finally, we examined the resource required per node qubit composing the 3D cluster states, namely the average number of the 3-tree cluster states to construct the hexagonal cluster state. The average number of the 3-tree cluster states to construct the 5-tree cluster state can be counted as $R_{5\text{tree}} = (1/P_{\text{SQEC}} + 2)/P_{\text{Bell}}^2$, where P_{SQEC} and P_{Bell} are the success probability of the single-qubit level QEC and of the Bell measurement with highly-reliable measurement, respectively. P_{SQEC} and P_{Bell} are calculated as $P_{\text{Suc}}(4\sigma^2)$ and $P_{\text{Suc}}(3\sigma^2) \times P_{\text{Suc}}(4\sigma^2)$, respectively, where $P_{\text{Suc}}(3\sigma^2)$ ($P_{\text{Suc}}(4\sigma^2)$) is the success probability of the highly-reliable measurement on the qubit of the variance is $3\sigma^2$ ($4\sigma^2$). Similarly, the average number of the 3-tree cluster states to construct the hexagonal cluster state can be counted as $R_{\text{Hexa}} = (1/P_{\text{Bell}-\text{II}}^2 + 1) \times (2/P_{\text{Bell}-\text{II}}^3)$, where $P_{\text{Bell}-\text{II}}$ is equal to $P_{\text{Suc}}^2(3\sigma^2)$. Therefore, the resources per the hexagonal cluster states R_{Hexa} with $v_{up} = 2\sqrt{\pi}/5$ can be estimated as 9.2×10^6 to achieve the required squeezing level 9.8 dB, since $P_{\text{Suc}}(3\sigma^2)$ and $P_{\text{Suc}}(4\sigma^2)$ with the squeezing level 9.8 dB are 34.6 % and 30.2 %, respectively.

Threshold value for the 3D cluster state without the single-qubit level QEC

We would like to mention the threshold value without the single-qubit level QEC for the node qubit. In the single-qubit level QEC, we use the ancilla qubit whose finite squeezing level is equal to that of the node qubit. Even if we do not employed the single-qubit level QEC, the proposed scheme with analog QEC does work well. In such a case, the measurement error probability of the node qubit $E_{\text{node}}(\sigma^2)$ in Eq. (35) increases to $E_{\text{node}}(3\sigma^2)$, which is avoided when the single-qubit level QEC is employed. As a result, the threshold of the squeezing level is degraded from ~ 9.8 dB to ~ 10.3 dB.

4.6 Discussion and conclusion

In this chapter, we have proposed a high-threshold FTQC to alleviate the required squeezing level for continuous variable-FTQC by harnessing analog information contained in the GKP qubits. The proposed method consists of applying analog QEC to the surface code and constructing the cluster state for the topologically protected measurement-base

quantum com with a low error accumulation by using the highly-reliable measurement. We have numerically shown that the required squeezing level can be improved to less than 10 dB with analog QEC on the 3D cluster states prepared by using the fusion gate with the highly-reliable measurement. Furthermore, we have numerically investigated validity of analog QEC for the surface code against the Gaussian quantum channel with ideal syndrome measurements. The numerical results have shown the analog QEC also achieves ~0.607 close to the hashing bound of the quantum capacity of the Gaussian quantum channel. To the best of our knowledge, no method to provide the optimal performance has been reported except for analog QEC.

To generate the GKP qubit, several methods have been proposed [36, 37, 38, 58, 39, 40, 41, 42]. In particular, a promising proposal [37] recently exists to prepare a good GKP qubit in circuit quantum electrodynamics with the squeezing level around 10 dB [51]. This suggests that the GKP qubit with the squeezing level around 10 dB will be able to generate within the reach of near-term experimental set-up. Our method can achieve this experimental requirement for the squeezing level, taking a step closer to the realization of large-scale quantum computation. Hence, this is the novel application of the analog information for the practical large scale measurement-base quantum com.

We would like to mention that the CZ gate in Ref. [4] is performed by the measurement on squeezed vacuum states on a 2D cluster state with ancilla GKP qubits used to implement the single-qubit level QEC. Then, the fault-tolerant threshold of the squeezing level is obtained from the error probability of the the single-qubit level QEC after the CZ gate combining with the conventional fault-tolerant schemes. While in Ref. [4] the threshold value 10^{-6} [17, 18, 15] to calculate the required squeezing level 20.5 dB is employed, here we use the threshold value 0.67% obtained in Ref. [12] to calculate the required squeezing level 16.0 dB to directly compare the existing scheme with the proposed scheme, where the analog QEC is applied. We should note that it is unfair to directly compare the present result with the required squeezing level 20.5 dB in Ref. [4], since optimization of the squeezing level would not be not the main scope of Ref. [4].

We would also like to mention the physical implementation for continuous variable-FTQC with our scheme. In our method, although the fusion gate is nondeterministic, there are a number of studies for the architecture that deal with topologically protected measurement-base quantum com with nondeterministic fusion gate [59, 60, 61]. Our method can be implemented by these architecture straightforwardly. Considering these

architecture, it is assumed that the hexagonal cluster state is prepared from the 3-tree cluster state by a purely linear optical network, composed of beam splitter coupling, an optical switch, and so on, while it is assumed that we can use the on-demand sources of the 3-tree cluster state.

Furthermore, analog QEC and the highly-reliable measurement can be not limited to the GKP qubit but widely applicable measurement-base quantum com using various QEC codes [33, 34, 35], and is a versatile tool for improvement of the QEC performance and the decision error of the bit value, which can incorporate with GKP qubit, cat code, and other various codes used to digitize continuous variable states. Hence, we believe this work will open up a new approach to QEC with digitized continuous variable states, which will be indispensable to construct continuous variable-FTQC.

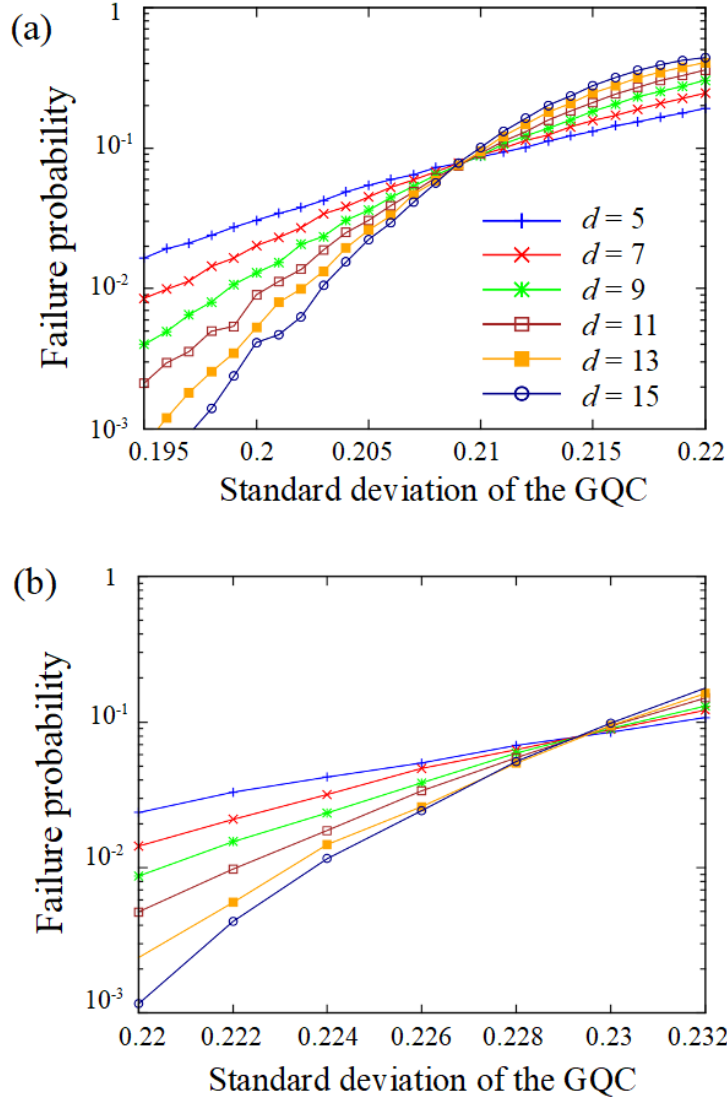Figure 4.4: Simulation results for the logical error probabilities of the surface code by using the 3D cluster state prepared by the proposed method for $v_{up} = 2\sqrt{\pi}/5$ with noisy syndrome measurements using (a) the digital QEC and (b) the analog QEC, respectively. The simulation results for the digital QEC are obtained from 50000 samples. The simulation results for the analog QEC are obtained from 10000 samples.

Chapter 5

Tracking quantum error correction

In large scale quantum computation, a large number of physical qubits is needed to obtain the highly accurate results of quantum computation. This required number of physical qubits is one issue that we should struggle toward the implementation of large scale quantum computation. In this chapter, we propose the method to reduce the number of qubits required for the QEC during large scale quantum computation, where the logical-qubit level QEC is partially substituted for the single-qubit level QEC. Since the single-qubit level QEC can not correct the qubit-level errors, the bit and phase flip errors, we just *track* the measurement outcomes in the single-qubit level QEC. Then, the QEC is performed by using a set of *tracked* measurement outcomes in QECs to correct the qubit-level errors.

In the end of this chapter, we would like to introduce an another method to harness analog information to reduce the error probability derived from the CZ gate using the maximum-likelihood estimation and the highly-reliable measurement. The proposed CZ gate will provide the way to reduce the required squeezing level for FTQC, which leads to realize practical quantum computers.

5.1 Tracking quantum error correction

5.1.1 Logical-qubit level quantum error correction

To implement large scale quantum computation, a number of single (physical) qubits are encoded into the logical qubit to correct errors on the logical qubit. Then, by using a fault-tolerant manner such as a concatenation, the error probability of the logical-qubit level QEC can be reduced to an arbitrary value, if the error probability on a physical qubit is less than the threshold value that varies depending on a variety of the QEC code. Since the logical-qubit level QEC is repeated during the quantum computation process, a large number of physical qubits is needed to obtain the highly accurate results of quantum computation. For example, for the Knill's C_4/C_6 code [19], the required number of physical qubits to prepare the level-l logical qubit and Bell state are $4 \times 12^{l-1}$ and $16 \times 12^{l-1}$,

respectively, where l (≥ 1) is the concatenation level. In general, the QEC is repeatedly performed by the only logical-qubit level QEC during the quantum computation process as shown in Fig. 5.1 (a). Accordingly, this required number of physical qubits is one issue that we should struggle toward the implementation of large scale quantum computation.

5.1.2 Tracking quantum error correction

We explain the method that the logical-qubit level QEC is partially substituted for the single-qubit level QEC [5] in the repeated QEC process as shown in Fig. 5.1 (b). In our method, we apply analog QEC [6] to the tracking QEC to improve the QEC performance. Since the single-qubit level QEC can reduce the error probability and the number of qubits required for the single-qubit level QEC is less than that for the logical-qubit level one, the substitution of the logical-qubit QEC for the single-qubit level one will reduce the required number of qubits.

To provide an insight into our method, we focus on the tracking QEC with the two QECs cycle, where the QEC after the Gaussian quantum channel is repeated twice as shown in Fig. 5.1. As a specific QEC code, we use the Knill's C_4/C_6 code [19], where the error correction in the C_4/C_6 code is based on quantum teleportation (see also [6] for details of analog QEC and the C_4/C_6 code). The quantum teleportation process refers to the outcomes M_p and M_q of the Bell measurement on the encoded qubits, and determines the amount of displacement. We obtain the Bell measurement outcomes of bit values m_{pi} and m_{qi} for the i-th physical GKP qubit of the encoded data qubit and encoded qubit of the encoded Bell state, respectively. In addition to bit values, we also obtain deviation values Δ_{pmi} and Δ_{qmi} for the i-th physical GKP qubit. In our method, the first and second QECs are performed by the single- and logical-qubit level QEC, respectively. Since the single-qubit level QEC can not correct the qubit-level error, we just *track* the measurement outcomes in the first QEC. After the two QECs, we obtain a set of the likelihoods are obtained from the results of the first and second QECs. From the set of the likelihoods in the two QECs, we consider the following two possible events: one is the correct decision, where the no qubit-level error occurs in both QECs. In this case, both true deviation values of the first and second QECs, $|\overline{\Delta}^{(1)}|$ and $|\overline{\Delta}^{(2)}|$, are less than $\sqrt{\pi}/2$ or more than $\sqrt{\pi}/2$. When both true deviation values are less than $\sqrt{\pi}/2$, $|\overline{\Delta}^{(1)}|$ and $|\overline{\Delta}^{(2)}|$ are equal to $|\Delta_m^{(1)}|$ and $|\Delta_m^{(2)}|$, respectively. When both true deviation values are more than $\sqrt{\pi}/2$, $|\overline{\Delta}^{(1)}|$ and $|\overline{\Delta}^{(2)}|$ are equal to $\sqrt{\pi} - |\Delta_m^{(1)}|$ and $\sqrt{\pi} - |\Delta_m^{(2)}|$, respectively. The other is the

(a) The conventional method

| Encoded state | → | Noise Channel | → | Logical-qubit level QEC | → | Noise Channel | → | Logical-qubit level QEC |

(b) The tracking QEC

| Encoded state | → | Noise Channel | → | Single-qubit level QEC | → | Noise Channel | → | Logical-qubit level QEC |

Figure 5.1: Introduction of the tracking QEC. (a) The conventional QEC with the two QECs cycle, where the QECs are performed with the only logical-qubit level QEC. (b) The tracking QEC with the two QECs cycle, where the first logical-qubit level QEC in the conventional method is substituted for the single-qubit level QEC.

incorrect decision, where the single error occurs in one of two QECs. In this case, one of two true deviation values of the first and second QECs are greater than $\sqrt{\pi}/2$, and satisfies $|\bar{\Delta}^{(1)}| = |\Delta_m^{(1)}|$ and $|\bar{\Delta}^{(2)}| + |\Delta_m^{(2)}| = \sqrt{\pi}$, or satisfies $|\bar{\Delta}^{(1)}| + |\Delta_m^{(1)}| = \sqrt{\pi}$ and $|\bar{\Delta}^{(2)}| = |\Delta_m^{(2)}|$, respectively. Hence, the likelihoods for the correct decision without and with analog QEC are calculated by

$$
\begin{aligned}
F_{\text{corr}} &= p_{\text{corr}}^2 + (1 - p_{\text{corr}})^2, & (5.1) \\
F_{\text{corr}}^{\text{ana}} &= f(|\Delta_m^{(1)}|)f(|\Delta_m^{(2)}|) \\
&\quad + f(\sqrt{\pi} - |\Delta_m^{(1)}|)f(\sqrt{\pi} - |\Delta_m^{(2)}|), & (5.2)
\end{aligned}
$$

respectively, where p_{corr} is given by Eq. (2.77). The likelihoods for the incorrect decision without and with analog QEC are calculated by

$$
\begin{aligned}
F_{\text{in}} &= 2(1 - p_{\text{corr}})p_{\text{corr}}, & (5.3) \\
F_{\text{in}}^{\text{ana}} &= f(|\Delta_m^{(1)}|)f(\sqrt{\pi} - |\Delta_m^{(2)}|) \\
&\quad + f(\sqrt{\pi} - |\Delta_m^{(1)}|)f(|\Delta_m^{(2)}|), & (5.4)
\end{aligned}
$$

respectively. By considering these likelihoods of the joint event and choosing the most likely candidate, we can reduce the decision error on the entire code word in the second logical-qubit level QEC. By contrast, in the conventional method, the two QECs are independently performed by the only logical-qubit level QEC. Although we focus on the

tracking QEC with the GKP qubits, we note that the tracking QEC with the discrete variables can be also performed, where the likelihoods are given by only Eqs. (5.1) and (5.3). In our method, we utilize analog QEC using Eqs. (5.2) and (5.4) to transform the QEC performance of the single-qubit level QEC into that of the approximately logical-qubit level QEC as shown in the numerical calculations.

We describe the details of the tracking QEC using the C_4/C_6 code with two QEC cycles. Fig. 5.2 shows the tracking QEC in the first cycle, that is, the single-qubit level QECs in the p and q quadratures, where the deviations of physical qubits composed of the logical data qubit are measured by ancilla qubits and corrected using the displacement operation independently. In the first cycle, we obtain the deviation values $\Delta_{p\mathrm{m}i}^{(1)}$ and $\Delta_{q\mathrm{m}i}^{(1)}$ for the i-th physical qubit in the q and p quadratures, respectively. In the second cycle, we obtain the bit values $k_{p\mathrm{m}i}$ and $k_{q\mathrm{m}i}$, and deviation values $\Delta_{p\mathrm{m}i}^{(2)}$ and $\Delta_{q\mathrm{m}i}^{(2)}$ in the p and q quadratures, respectively. We note that the displacement operation in the single-qubit level QEC is not necessarily for our method, since the displacement operation can be performed in the logical-qubit level QEC all at once.

As a simple example to describe the tracking QEC, we explain the QEC with concatenation level 1. As described in Chap. 3, we decide the logical bit value $M_{q,L=1}$ and $M_{p,L=1}$ by using the parity check operator obtained from the measurement outcome $k_{q\mathrm{m}i}$ and $k_{p\mathrm{m}i}$, respectively. When the measurement outcome $(k_{q\mathrm{m}1}, k_{q\mathrm{m}2}, k_{q\mathrm{m}3}, k_{q\mathrm{m}4})$ is $(0,0,1,0)$ in the q quadrature, we consider two error patterns as described in Chap. 3. Considering the two error patterns, where a single error on the third qubit and the triple errors on the physical qubits except for the third qubit, we then calculate the likelihood for the level-1 qubit pair $(0,0)$ $F_{0,0}$ with the analog QEC as

$$F_{0,0} = F_{\mathrm{in},1}^{\mathrm{ana}} F_{\mathrm{in},2}^{\mathrm{ana}} F_{\mathrm{corr},3}^{\mathrm{ana}} F_{\mathrm{in},4}^{\mathrm{ana}} + F_{\mathrm{corr},1}^{\mathrm{ana}} F_{\mathrm{corr},2}^{\mathrm{ana}} F_{\mathrm{in},3}^{\mathrm{ana}} F_{\mathrm{corr},4}^{\mathrm{ana}}. \tag{B1}$$

$F_{\mathrm{corr},i}^{\mathrm{ana}}$ is the likelihood of no error and double errors on the i-qubit in the single-qubit level and the logical-qubit level QECs, and described by

$$
\begin{aligned}
F_{\mathrm{corr},i}^{\mathrm{ana}} = {} & f(|\Delta_{q\mathrm{m}i}^{(1)}|) f(|\Delta_{q\mathrm{m}i}^{(2)}|) \\
& + f(\sqrt{\pi} - |\Delta_{q\mathrm{m}i}^{(1)}|) f(\sqrt{\pi} - |\Delta_{q\mathrm{m}i}^{(2)}|).
\end{aligned}
\tag{B2}
$$

$F_{\mathrm{in},i}^{\mathrm{ana}}$ is the likelihood of a single error on the i-qubit in one of the single-qubit level and
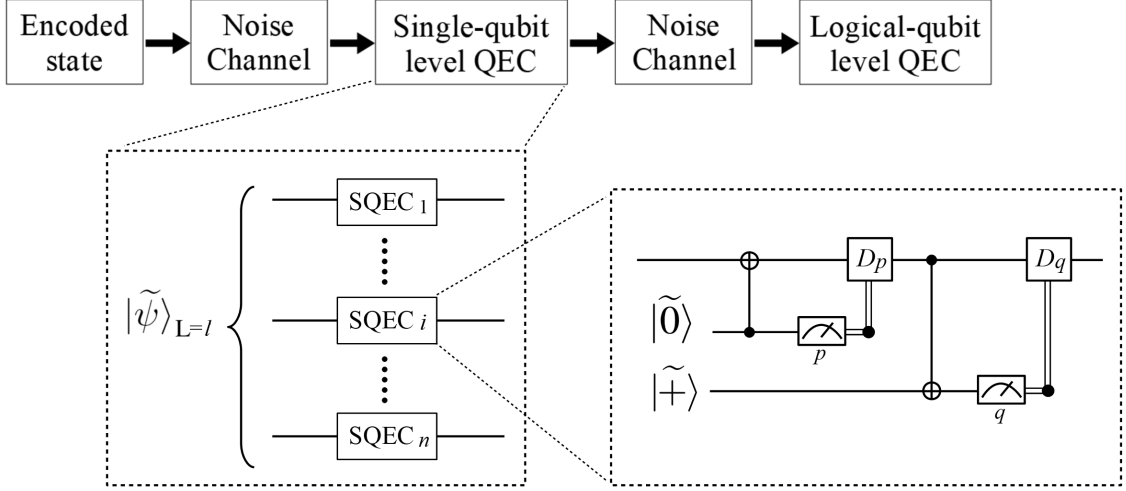
Figure 5.2: A quantum circuit for the tracking QEC for two QEC cycles. The logical data qubit $|\widetilde{\psi}\rangle_{\mathrm{L}=l}$ with the concatenation level l is composed of the $n = 4 \times 3^{l-1}$ physical qubits. SQEC_i ($i = 1, 2, \cdots, n$) denotes the single-qubit level QEC for the i-th qubit, where the single-qubit level QECs in the p and p quadratures are implemented by ancilla physical qubits $|\widetilde{0}\rangle$ and $|\widetilde{+}\rangle$, respectively.

the logical-qubit level QECs, and described by

$$
\begin{aligned}
F_{\mathrm{in},i}^{\mathrm{ana}} = {} & f(|\Delta_{q\mathrm{m}i}^{(1)}|) f(\sqrt{\pi} - |\Delta_{q\mathrm{m}i}^{(2)}|) \\
& + f(\sqrt{\pi} - |\Delta_{q\mathrm{m}i}^{(1)}|) f(|\Delta_{q\mathrm{m}i}^{(2)}|).
\end{aligned}
\tag{B3}
$$

We similarly calculate the $F_{0,1}, F_{1,0}$, and $F_{1,1}$ likelihood for the bit value of qubit pairs $(0,1)$, $(1,0)$, and $(1,1)$. In a similar manner of the logical-qubit level QEC, we determine the level-1 logical bit value $M_{q,L=1}$ in the q quadrature by comparing $F_{0,0} + F_{0,1}$ with $F_{1,0} + F_{1,1}$. In the tracking QEC without the analog QEC, likelihoods $F_{0,0}$, $F_{0,1}$, $F_{1,0}$, and $F_{1,1}$ are given by the same joint probability

$$
F_{\mathrm{corr}}^3 F_{\mathrm{in}} + F_{\mathrm{corr}} F_{\mathrm{in}}^3,
\tag{B4}
$$

where F_{corr} and F_{in} are defined by Eqs. (3.2) and (3.3) in Chap. 3, respectively. Therefore, the tracking QEC without the analog QEC is not error-correcting code but error-detecting code, whereas that with the analog QEC is the error-correcting code. The likelihood for the level-l ($l \geqq 2$) bit value can be calculated by the likelihood for the level-$(l - 1)$ bit value in a similar manner.

We here estimate the required number of physical qubits to implement the two QECs. In the C_4/C_6 code with the concatenation level l ($l \geq 1$), the logical qubit is composed

of the $4 \times 3^{l-1}$ physical qubits, and the preparation of the logical qubit and the logical Bell pair level l consumed $4 \times 12^{l-1}$ and $16 \times 12^{l-1}$, respectively [23, 19]. Therefore, the required number of physical qubits for the logical-qubit level QEC is $16 \times 12^{l-1}$, where the logical-qubit level QEC consumes the logical Bell pair. By contrast, the required number of physical qubits for the single-qubit level QEC is $2 \times 4 \times 3^{l-1}$, where each physical qubit composing the logical data qubit consumes two ancilla physical qubits to correct the small deviation in the q and p quadratures. In the case of the QEC process with the two-QEC cycle, the number of the physical qubits for the conventional method $R_{\mathrm{con}}^{(2,l)}$ and proposed method $R_{\mathrm{pro}}^{(2,l)}$ are

$$
\begin{aligned}
R_{\mathrm{con}}^{(2,l)} &= 2 \times 16 \times 12^{l-1}, & (5.5) \\
R_{\mathrm{pro}}^{(2,l)} &= 2 \times 4 \times 3^{l-1} + 16 \times 12^{l-1}, & (5.6)
\end{aligned}
$$

respectively. Hence, the proposed method for the two-QEC cycle reduces by $R_{\mathrm{con}}^{(2,l)} - R_{\mathrm{pro}}^{(2,l)}$ $= 16 \times 12^{l-1} - 8 \times 3^{l-1}$ physical qubits with the concatenation level l. Similarly, the conventional and proposed methods for the n-QEC cycle, consume the physical qubits $R_{\mathrm{con}}^{(n,l)}$ and $R_{\mathrm{con}}^{(n,l)}$ as

$$
\begin{aligned}
R_{\mathrm{con}}^{(n,l)} &= n \times 16 \times 12^{l-1}, & (5.7) \\
R_{\mathrm{pro}}^{(n,l)} &= 2(n-1)4 \times 3^{l-1} + 16 \times 12^{l-1}, & (5.8)
\end{aligned}
$$

respectively. Hence, the proposed method for the n-QEC cycle can reduce $R_{\mathrm{con}}^{(n,l)} - R_{\mathrm{pro}}^{(n,l)} = (n-1) \times \left\{ R_{\mathrm{con}}^{(2,l)} - R_{\mathrm{pro}}^{(2,l)} \right\}$ physical qubits, where the single- and logical-qubit level QECs are performed in the first $(n-1)$-QECs and the n-th QEC, respectively. Finally, we describe the reduction rate of the number of physical qubits per n-QEC cycle. For the n-QEC cycle using C_4/C_6 code with the level l, the reduction rate is obtained by

$$
\frac{R_{\mathrm{con}}^{(n,l)} - R_{\mathrm{pro}}^{(n,l)}}{R_{\mathrm{con}}^{(n,l)}} = \frac{2(n-1) \times 4^{l-1} - n + 1}{2n \times 4^{l-1}}. \tag{5.9}
$$

71

5.2 Numerical calculations

To validate the effectiveness of our proposed method, we calculate the failure probability of the QEC and the number of physical qubits required in the QEC using the Monte Carlo method. We examine the tracking QEC performance, taking the conventional logical-qubit level QEC without the analog QEC as a reference. We simulate the QEC after the Gaussian quantum channel is repeated twice as described in Sec. 5.1.2. In this simulation, we use the Knill's C_4/C_6 code [19] for the concatenation and assume that the encoded data qubit, encoded Bell state, and the physical qubits are prepared perfectly, and the variance of the GKP qubits of the encoded data qubit is increased to σ^2 only by the Gaussian quantum channel. In the noise channel of the Gaussian quantum channel with n-cycles, the logical-qubit suffers from each of n-noise channels independently by the same amount of the noise.

In Fig. 5.3, the failure probabilities for the q (p) quadrature up to level 5 of the concatenation are plotted as a function of the noise level as the standard deviation of the Gaussian quantum channel. The noise is given by the sum of the noise of the first and second QECs, where the encoded state suffers from the same amount of the noise in the first and second QECs. We here define the threshold for the two-QEC cycle as; if the sum of the noise of two cycles is below the threshold, the failure probability with the concatenation level l can be reduced super exponentially as l becomes large. Hence, all the lines plotted as a function of a noise level for various concatenation level l meet at a single point, indicating the threshold value. In Fig. 5.3, we have plotted the failure probabilities (a) without the analog QEC and (b) with the analog QEC for the conventional two logical-qubit level QECs and the proposed method, respectively. In the case of the Gaussian quantum channel, the displacement errors in the q and p quadrature occur independently. Considering the CSS code, where errors in the q and p quadrature can be treated separately, the failure probabilities for the q and p quadrature has the same value. As shown in Fig. 5.3, the conventional method without and with the analog QECs achieve the threshold values of the standard deviation values ~ 1.11 and ~ 1.21, respectively. These threshold values are identical to twice of those obtained for the single cycle of the logical-qubit level QEC ~ 0.555 and ~ 0.607 in Ref. [6], respectively. It results from the fact that the failure probability of the two-QEC cycle for the conventional method is calculated by $2 \times P(1-P)$, where the probability P is the failure probability of the sin-

gle cycle of the logical-qubit level QEC. This is because the sequential logical-qubit level QECs are performed independently after the each of two noise channels, and the event to fail in the logical-qubit level QEC occurs independently.

Fig. 5.3 (a) show that the tracking QEC degrades the threshold of the standard deviation by ~ 0.17 without the analog QEC. Fig. 5.3 (b) show that the tracking QEC also degrades the threshold of the standard deviation by ~ 0.07 with analog QEC. However, the degradation with the analog QEC is smaller than that without the analog QEC. More specifically, we compare the ratio of failure probabilities between the tracking QEC without and with the analog QEC at the same noise level of the standard deviation and the same concatenation level. For example, the ratio for the analog QEC with the concatenation level 1 is obtained by $0.00421/0.00375 \sim 1.1$, similarly the ratios with the concatenation level 2 and 3 are ~ 1.2 and ~ 1.4, respectively, by contrast, the ratios without the analog QEC with the concatenation level 1, 2 and 3 are ~ 1.8, ~ 3.7 and ~ 13.8, respectively. Hence, it is clear that the ratios of the proposed method with the analog QEC are greater than that without the analog QEC. In addition, it is remarkable that the tracking QEC with the analog QEC in Fig. 5.3 (b) suppresses errors more effectively than the conventional method without the analog QEC. Furthermore, it is also remarkable that the ratios of the tracking QEC with the analog QEC become greater as the noise level of the standard deviation become smaller, and the analog QEC makes the performances of the single-qubit level QEC almost identical to that of the logical-qubit level QEC in a low noise level. These results show the virtue of use of analog information. On the basis of these results, for the 2-QEC cycle, we can conclude that the proposed method with analog QEC in the practical noise level can achieve efficient resource reduction by $16 \times 12^{l-1} - 8 \times 3^{l-1}$ physical qubits with the concatenation level l with only a small impact on the QEC performance, where the reduction rate for the 2-QEC cycle is $(2 \times 4^{l-1} - 1)/(4 \times 4^{l-1}) = 1/2 - 1/(4 \times 4^{l-1})$. Hence, the reduction rate becomes close to 50 % for larger l, where the reduction rates are 25, 43.8, 48.4, 49.6 and 49.9 for the level 1, 2, 3, 4, and 5, respectively.

In the following, we consider admissible noise level of the Gaussian quantum channel for the tracking QEC. In practice, fault-tolerant quantum computation should be performed with a noise level smaller than the threshold value so as not to spend huge amounts of single qubits to prepare logical qubits with the required concatenation level l. To evaluate our proposed method, we assume that the single- and logical-qubit level QECs are

performed with one-tenth of the threshold value according to Refs. [62, 63]. For simplicity, we use the threshold value as the rate of the misidentifying the bit value of the GKP qubit. In the logical-qubit level QEC, the threshold of the noise level per cycle ~ 0.555 and ~ 0.607 for without and with analog QEC correspond to the error rate of the misidentifying the bit value ~ 11.0 % and ~ 14.3 %, respectively, where the error rate of the misidentifying is obtained by $1 - p_{\mathrm{corr}}$ given in Eq. (2.77) in Chap. 2. Therefore, we set the rate of the misidentifying the bit value as ~ 1.1 % and ~ 1.43 % which correspond to a noise level ~ 0.346 and ~ 0.362. As shown in Fig. 5.3 (a), there is a gap of failure probabilities between the conventional and proposed method with the set noise level of $\sim 2 \times 0.346 = 0.692$ without the analog QEC. By contrast, the failure probabilities of the proposed method with the analog QEC is almost same as that of the conventional method with the set noise level $\sim 2 \times 0.362 = 0.724$ as shown in Fig. 5.3 (b).

5.3 Discussion and conclusion

In this chapter, we have proposed the tracking QEC with analog QEC to reduce the number of qubits required for large scale quantum computation, bringing up the advantages of the GKP qubits in practical quantum computation. In the proposed method, the single-qubit level QEC is combined with the standard logical-qubit level QEC, in a way that a part of the logical-qubit level QEC is substituted by the single-qubit level QEC during the quantum computation. Furthermore, we propose to apply the analog QEC to the tracking QEC to improve the QEC performance. Regarding the possible experimental implementation, the proposed tracking QEC will be applicable to repeated quantum nondemolition measurements and adaptive control in a superconducting cavity resonator setup [64, 65, 66], which can be regarded as repeated single-qubit level QECs.

The numerical results for the two-QEC cycle showed that the proposed method with analog QEC reduces the required number of the qubits without degrading the QEC performance. The tracking QEC with analog QEC reduces the number of physical qubits required for the C_4/C_6 code by $16 \times 12^{l-1} - 8 \times 3^{l-1}$ for the 2-QEC cycle with the concatenation level l, and the reduction rate for is $1/2 - 1/(4 \times 4^{l-1})$, where the reduction rates are 25, 43.8, 48.4, 49.6 and 49.9 for the level 1, 2, 3, 4, and 5, respectively.

Furthermore, it has been shown that the analog QEC makes the performances of the single-qubit level QEC almost identical to those of the logical-qubit level QEC under the

condition of a practical noise level. To the best of our knowledge, this approach is the first practical attempt to utilize both the single- and standard logical-qubit level QECs to alleviate the requirement of the number of qubits. Hence, the proposed method has a great advantage in implementing fault-tolerant quantum computation with continuous variables and will open a new way to practical quantum computers.

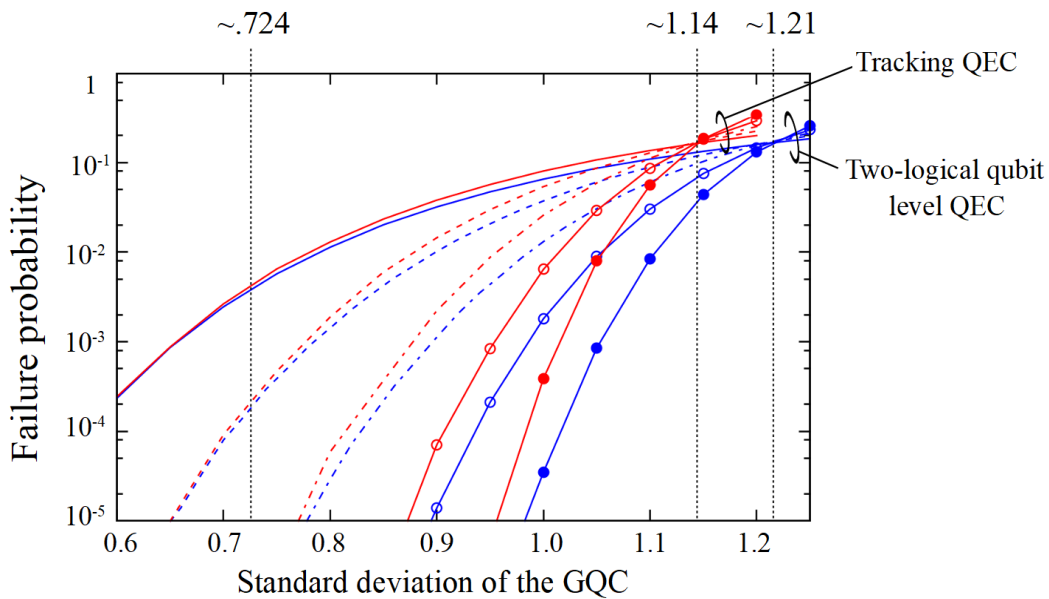## (a) Without the analog QEC
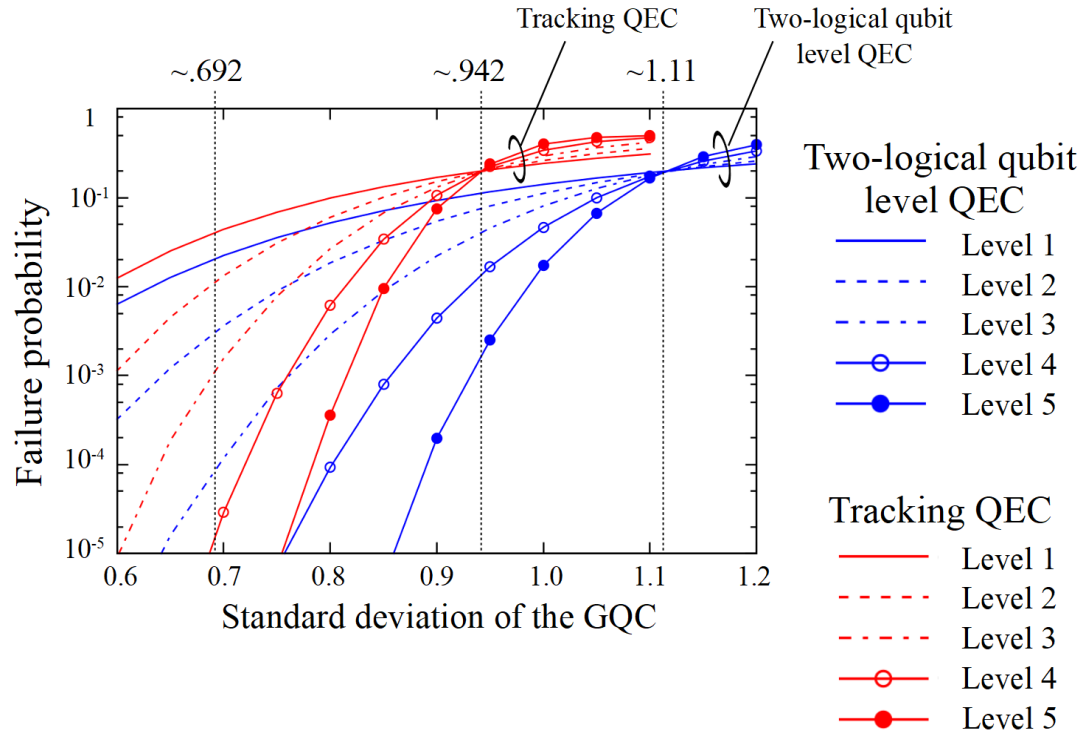
(b) With the analog QEC

Figure 5.3: Simulation results for the failure probabilities of the two QECs for the q (p) quadrature with the C_4/C_6 code using the conventional (blue line) and proposed method (red line). GQC describes the Gaussian quantum channel. The results without the analog QEC (a) and with the analog QEC (b) are represented for the concatenation level 1 (solid), level 2 (dashed), level 3 (dashed-dotted), level 4 (open circles), and level 5 (filled circles), respectively. The thresholds are indicated by the vertical dashed lines with ~ 1.11, ~ 0.942, ~ 1.21, and ~ 1.14. The vertical dashed lines with ~ 0.692 and ~ 0.724 indicate the standard deviation for the practical noise level defined in the main text.

Appendix for Chap. 5: Method to reduce the propagation error in the CZ gate

In the end of this chapter, we would like to introduce an another method to harness analog information to realize practical quantum computers, where the highly-reliable gate operation using the maximum-likelihood estimation reduces error propagation caused by the CZ gate between GKP qubits. In our method the ancilla qubits are put between the controlled and target qubits, and measured to estimate the deviations of the controlled and target qubits by using the maximum-likelihood estimation.

Method to reduce the error propagation

The maximum-likelihood estimation is an effective tool to estimate the values of parameters. In the proposed method, we apply the maximum-likelihood estimation to estimate the true deviation of the GKP qubit to reduce the error propagation cased by the CZ gate. In Fig.5.4 (a), we show a quantum circuit in which the true deviation of the qubit A is estimated using an ancilla qubit A1. After the CZ gate, the true deviation of the qubit A in q quadrature is projected onto the deviation of the qubit A1 in p quadrature as

$$\delta_{p,A1} \rightarrow \delta_{p,A1} - \delta_{q,A}. \tag{5.10}$$

By measurement of the qubit A in p quadrature, we obtain the value $\delta_{p,A1} - \delta_{q,A}$. Then, we can estimate the deviation value of the qubit A in q quadrature as $(\delta_{p,A1} - \delta_{q,A})/2$, considering the Gauss-Markov theorem in statistics. This is because the true deviation of the qubit A obeys posterior probability that is Gaussian distribution of mean $(\delta_{p,A1} - \delta_{q,A})/2$ with variance $\sigma^2/2$ after measurement of the qubit A1. After the displacement by $-(\delta_{p,A1} - \delta_{q,A})/2$ in the q quadrature, the variance of the qubit A in q quadrature reduces from σ^2 to $\sigma^2/2$, while the variance of the qubit A in p quadrature increase from σ^2 to $2\sigma^2$. This maximum-likelihood estimation is based on the fact that the measurement deviation values from the GKP qubits are obeyed the Gaussian distribution independently. Next, we consider estimating the deviation value $\delta_{q,A}$ using n ancilla qubits. Fig. 5.4 (b) shows a quantum circuit to estimate the deviation value $\delta_{q,A}$ using the n ancillae. By
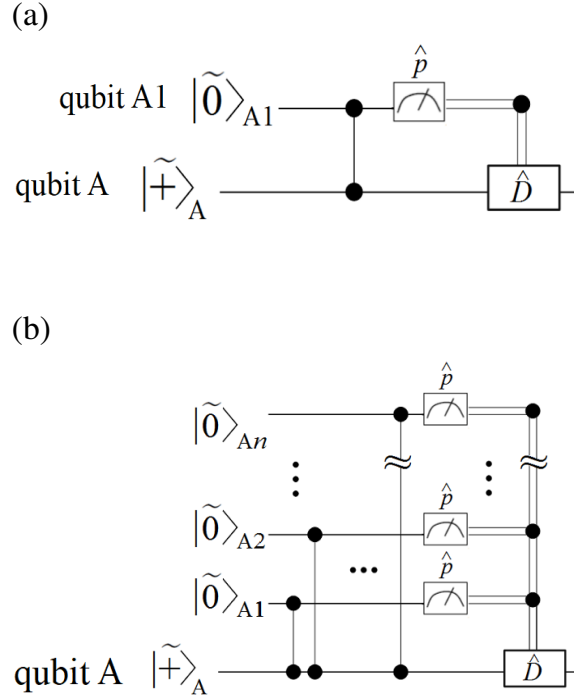
(a)

(b)

Figure 5.4: A quantum circuit for the maximum-likelihood estimation of the true deviation value of the qubit A. (a) A quantum circuit for the maximum-likelihood estimation using a single ancilla qubit A1. (b) A quantum circuit for the maximum-likelihood estimation using n ancilla qubits. $\hat{D}$ is a displacement operation to correct the deviation.

measurement of the qubit Ai in p quadrature, we obtain the deviation value $\delta_{p,Ai} - \delta_{q,A}$. Then, we can estimate the deviation value $\delta_{q,A}$ as

$$(\sum_{i=1}^{n} \delta_{p,Ai} - \delta_{q,A})/(n+1), \tag{5.11}$$

by using the maximum-likelihood estimation. Here we assumed the all variance are equal to σ^2. As a result, the variance of the qubit A in q quadrature reduces from σ^2 to $\sigma^2/(n+1)$, while the variance of the qubit A in p quadrature increases from σ^2 to $(n+1)\sigma^2$.

We propose a method to reduce the error propagation in the CZ gate by combining the highly-reliable measurement proposed in Sec. 4.3 and the maximum-likelihood estimation of the true deviation value of the GKP qubit. In Fig. 5.5, a quantum circuit for the proposed CZ gate is showed. In our method the controlled qubit C, $|\widetilde{\psi}\rangle_C$, and target qubit T, $|\widetilde{\Phi}\rangle_T$, are entangled using Bell measurement on the qubit A, $|\widetilde{+}\rangle_A$, and qubit B, $|\widetilde{+}\rangle_B$.

At step 1 in Fig. 5.5 the variances of the qubits A and B in q quadrature, which are propagated on the qubit C and T, are reduced using the maximum-likelihood estimation
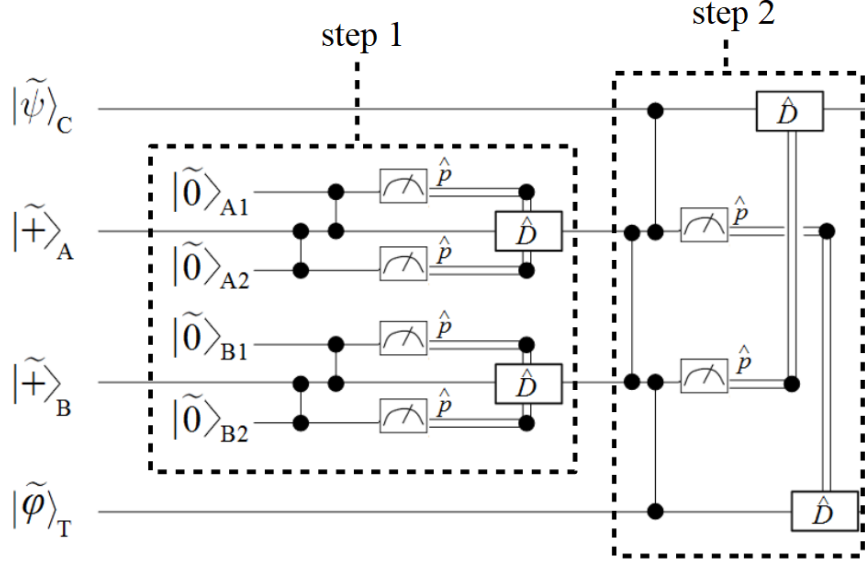
Figure 5.5: A quantum circuit for our method. Step 1 describes a quantum circuit for the maximum-likelihood estimation of the true deviation values of the qubit A and B. Step 2 describes the highly-reliable measurement for the qubit A and B in the p quadrature.

with ancilla qubits A_i and B_i, respectively. On the other hand the variances of qubits A and B in p quadrature are increased by error propagation. Here we assumed the all variances are equal to σ^2 before step 1. Then the variance of qubit A (B) in q and p quadrature are equal to $\sigma^2/(n+1)$ and $(n+1)\sigma^2$ after step 1, respectively. At step 2 we measure the qubits A and B in p quadrature and obtain the bit value for the qubits A and B, which is called as Bell measurement. Then, the feedforward operation according to the measurement result for the qubits A and B is performed on for the qubits T and A, respectively. If this feedforward operation is performed correctly, the CZ gate between qubits C and T is successfully implemented. As a result, the variance of the qubit C and T in p quadrature changes from σ^2 to $\sigma^2 + \sigma^2/(n+1)$ using our method, while the variance of the qubit C and T in p quadrature changes to $2\sigma^2$ using the conventional (direct) CZ gate. Therefore, our method can reduce the error propagation caused by the CZ gate, if the feedforward operation is performed correctly.
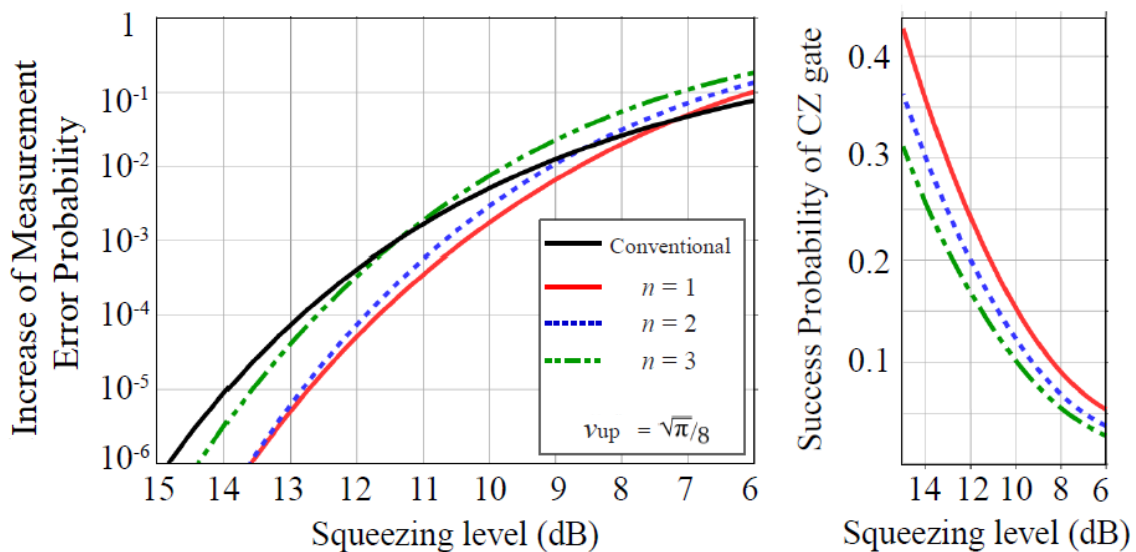
Numerical calculations

Figure 5.6: Simulation results for the measurement error probabilities of the CZ gate using the conventional and proposed method. The failure probabilities using the conventional method (bold line) and proposed method are represented for $n=1$ (solid), $n=2$ (dashed), $n=3$ (dot-dot-dashed) with the upper value $v_{th} = \sqrt{\pi}/8$ for the highly-reliable measurement.

To evaluate the effectiveness of our method, we compare the error propagation of conventional method using the direct CZ gate with that of our method using the maximum-likelihood estimation and the highly-reliable measurement. For the direct CZ gate, the error propagation increases the error probability E_{con} that the bit value in p quadrature is misidentified, since the variance of the qubit in p quadrature increases by σ^2 after the direct CZ gate. On the other hand, the error propagation in our method increases the error probability E_{pro} that the bit value in p quadrature is misidentified, since the variance of the qubit in p quadrature increases by $\sigma^2/(n+1)$. In addition to E_{pro}, we count the error probability E_{Bell} that the Bell measurement on qubit A and B is failure. Therefore, if $E_{pro} + E_{Bell} < E_{con}$, we consider that the proposed CZ gate is more error-tolerant than the conventional CZ gate.

To valid our method, we numerically calculated the error probability E_{con} and $E_{pro}+ E_{Bell}$ for the several number of ancilla qubits, n, assuming that all variances of the GKP qubit before the CZ gate are equal to σ^2. In the calculations, we set the upper limit value $v_{up} = \sqrt{\pi}/8$, because our method is saturated around $\sqrt{\pi}/8$ and can not improve the performance of our method further above $\sqrt{\pi}/8$. In Fig. 5.6, E_{con} for the conventional CZ gate and $E_{pro}+ E_{Bell}$ are plotted as a function of the squeezing level s of the GKP qubit for conventional (bold) and proposal with $n = 1$ (solid), 2 (dotted), and 3 (dashed-dotted),

80

where the squeezing level s is equal to $-10\log_{10}2\sigma^2$. Numerical results show that our method improves the error tolerance when the squeezing level s is more than 7.8 dB. In Fig. 5.6, the success probability of our method is plotted as a function of the squeezing level of the GKP qubit for conventional (bold) and proposal with $n = 1$ (solid), 2 (dotted), and 3 (dot-dot-dashed).

To reduce the required squeezing level for large-scale quantum computation, our method can applied to the method to implement FTQC proposed in chapter. 4, where the required squeezing level for FTQC is around 10 dB. By substituting the proposed CZ gate for the conventional CZ gate, the required squeezing level will be reduced. Considering the error probability of the direct CZ gate with 10 dB, it is estimated that our method with $n = 1$ and 2 can reduce the required squeezing level for FTQC by ~ 0.3 and ~ 0.8 dB, respectively. In future work, we will apply the proposed CZ gate to the method proposed in Chap. 4 to reduce the required squeezing level. In the work, we will show that our method of implementation of FTQC with the CZ gate proposed in this Appendix can reduce the required squeezing level to about 9 dB.

Chapter 6

Analog entanglement distillation

The entanglement distillation (purification) protocol is an essential tool to distribute the entangled states with a high-fidelity between a distant party, which is used to implement quantum information processing such as quantum key distribution, quantum communication based on quantum repeaters, teleportation, dense coding, distributed quantum computation, and so on. In this chapter, we focus on a so-called quantum privacy amplification protocol [67]. Firstly, we model the quantum privacy amplification protocol for ideal and approximate GKP qubits. Next, we propose the quantum privacy amplification protocol with the GKP qubit using analog information to improve the entanglement distillation performance. In the proposed method, the highly-reliable measurement is applied to the conventional entanglement distillation protocol. Finally, we numerically calculate the performance of the quantum privacy amplification protocol to valid our method.

6.1 Entanglement distillation

The performance of quantum information processing based on the entangled states depends on the fidelity of the entangled states. Since the entangled states with a high-fidelity is are essential for secure communication and quantum computation with a high-fidelity, the preparation of the high-fidelity entangled states sheared by a distant party is very important task. The entanglement distillation (purification) is a method to distribute high-fidelity entangled states to distant parties through a quantum channel even if the quantum channel is noisy. As a simple example to explain the entanglement distillation, we focus on a quantum privacy amplification protocol [67] that can be implemented by a sequence of local operations between distant parties, Alice and Bob, where the operations depend on the measurement results of the sheared entangled states and agreement using communication between them. In this section, we apply the GKP qubits to the quantum privacy amplification protocol. Firstly, we briefly describe the quantum privacy amplification pro-

tocol with discrete variables to compare that with GKP qubits. Secondly, we explain how to apply the GKP qubits to a quantum privacy amplification protocol.

6.1.1 Quantum privacy amplification with discrete variables

Fig. 6.1 shows a schematic diagram for the introduction of the quantum privacy amplification with discrete variables.

We briefly describe the quantum privacy amplification presented in Ref. [67]. Fig. 6.1 shows a schematic diagram for the introduction of a quantum privacy amplification with discrete variables. We assume that Alice and Bob receive the qubit pairs supplied through a quantum channel by Eve who prepares and sends the pure Bell state $|\Phi^+\rangle\langle\Phi^+|$ as shown in Fig. 6.1, where $|\Phi^+\rangle$ is described as

$$|\Phi^+\rangle = \frac{1}{\sqrt{2}}(|00\rangle + |11\rangle). \tag{6.1}$$

After the quantum channel, the pure Bell state is degraded as

$$
\begin{aligned}
|\Phi^+\rangle\langle\Phi^+| \to \rho &= a|\Phi^+\rangle\langle\Phi^+| + b|\Psi^-\rangle\langle\Psi^-| \\
&+ c|\Psi^+\rangle\langle\Psi^+| + d|\Phi^-\rangle\langle\Phi^-|,
\end{aligned}
\tag{6.2}
$$

where $|\Phi^\pm\rangle$ and $|\Psi^-\rangle$ are given as

$$|\Psi^\pm\rangle = \frac{1}{\sqrt{2}}(|01\rangle \pm |10\rangle), \tag{6.3}$$

$$|\Phi^-\rangle = \frac{1}{\sqrt{2}}(|00\rangle - |11\rangle), \tag{6.4}$$

respectively. Suppose that Alice and Bob share two qubit pairs represented by ρ_1 and ρ_2. Alice performs a unitary operation U_A on each of her two qubits, where U_A is described as

$$U_A = \frac{1}{\sqrt{2}}\begin{pmatrix} 1 & -i \\ -i & 1 \end{pmatrix}. \tag{6.5}$$

On the other hand, Bob performs a unitary operation U_B on each of their two qubits, where U_B is described as

$$U_B = \frac{1}{\sqrt{2}}\begin{pmatrix} 1 & i \\ i & 1 \end{pmatrix}. \tag{6.6}$$
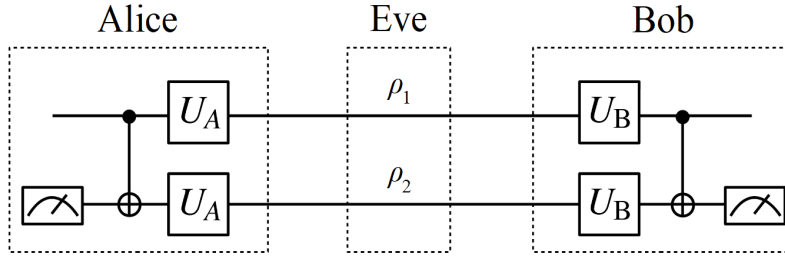
Figure 6.1: Introduction of a quantum privacy amplification with discrete variables. Alice and Bob share the Bell pairs ρ_1 and ρ_2 sent from Eve. After operations U_A, U_B, and CNOT gate, targeted qubits are measured in the computational basis.

Then Alice and Bob each perform the CNOT gate between each of his two qubits. After the CNOT gate, they measure the target qubits in the computational bases (Z basis). If two measurement outcomes of the bit value coincide, they keep the control qubits and the remaining pair ρ_1' is used for next round of the protocol. Otherwise, both pairs are discarded. We can see the effect of this protocol in comparison the diagonal element of ρ_1 with that of ρ_1'. Assuming the diagonal elements of ρ_1 is defined as $\{a,b,c,d\}$, those of ρ_1', $\{A,B,C,D\}$, are given by

$$A = \frac{a^2+b^2}{P}, \quad B = \frac{2cd}{P}, \quad C = \frac{c^2+d^2}{P}, \quad D = \frac{2ab}{P}, \tag{6.7}$$

where P is the probability that two measurement outcomes of the bit value coincide, and P is equal to $(a+b)^2 + (c+d)^2$. By using this procedure repeatedly, Alice and Bob can generate the Bell pair that is close to a pure Bell state, for example, in case where $a > 1/2$ and $b = c = d$. Accordingly, the aim of a quantum privacy amplification is to achieve a maximum value of the probability (fidelity) of the state $|\Phi^+\rangle\langle\Phi^+| \sim 1$

6.1.2 Quantum privacy amplification with ideal GKP qubits

We explain a quantum privacy amplification protocol with ideal GKP qubits in Fig. 6.2 (a), where the squeezing level of GKP qubits is degraded only by the Gaussian quantum channel, and initial and ancilla GKP qubits are ideal. In the case of ideal GKP qubits, Eve prepares and sends the Bell state of ideal GKP qubits described as

$$|\widetilde{\Phi}^+\rangle_{\text{ideal}} = \frac{1}{\sqrt{2}}(|\widetilde{00}\rangle_{\text{ideal}} + |\widetilde{11}\rangle_{\text{ideal}}). \tag{6.8}$$

84

After the Gaussian quantum channel with a noise level ξ^2, Alice and Bob are received the Bell state composed of GKP qubits with the finite squeezing level corresponding to $-10\log_{10}(2\xi^2)$. To recover the GKP qubits from degrading the squeezing level, Alice and Bob perform the single-qubit level QEC in the q and p quadratures on each of their two qubits as shown in Fig. 6.2 (b). When the single-qubit level QEC succeeds, the squeezing level of their GKP qubits recovers to be infinite. When the single-qubit level QEC fails, the qubit-level errors occur on the Bell state, although the squeezing level recovers to be infinite. For the failure of the single-qubit level QEC in the q quadrature on the qubit of one of Alice and Bob, $|\widetilde{\Phi}^+\rangle$ is degraded to $|\widetilde{\Psi}^+\rangle$. Hence, we can consider the degradation affected by the Gaussian quantum channel and the single-qubit level QEC as

$$
\begin{aligned}
|\widetilde{\Phi}^+\rangle_{\text{ideal}} \langle\widetilde{\Phi}^+| \quad \rightarrow \quad & p_a |\widetilde{\Phi}^+\rangle_{\text{ideal}} \langle\widetilde{\Phi}^+| + p_b |\widetilde{\Psi}^-\rangle_{\text{ideal}} \langle\widetilde{\Psi}^-| \\
+ \quad & p_c |\widetilde{\Psi}^+\rangle_{\text{ideal}} \langle\widetilde{\Psi}^+| + p_d |\widetilde{\Phi}^-\rangle_{\text{ideal}} \langle\widetilde{\Phi}^-|,
\end{aligned}
\tag{6.9}
$$

where the p_a, p_b, p_c, and p_d are the probabilities derived from the single-qubit level QEC operation for the q and p quadratures. These probabilities are given by

$$
\begin{aligned}
p_a &= 1 - p_b - p_c - p_d, &\tag{6.10} \\
p_b &= 4 \times E_{\xi^2}{}^2 (1 - E_{\xi^2})^2, &\tag{6.11} \\
p_c &= p_d = 2 \times E_{\xi^2}(1 - E_{\xi^2})^3 + 2 \times E_{\xi^2}{}^3(1 - E_{\xi^2}), &\tag{6.12}
\end{aligned}
$$

where the probability E_{ξ^2} with a noise level ξ^2 is calculated as

$$
E_{\sigma^2} = 1 - P_{\sigma^2},
\tag{6.13}
$$

where P_{σ^2} is obtained by Eq. (2.77) as

$$
P_{\sigma^2} = \int_{-\frac{\sqrt{\pi}}{2}}^{\frac{\sqrt{\pi}}{2}} dx \frac{1}{\sqrt{2\pi\sigma^2}} \exp(-x^2/2\sigma^2).
\tag{6.14}
$$

We assumed that the ancilla GKP qubits used for the single-qubit level QECs are ideal GKP qubits. Then, in the same way as the quantum privacy amplification with the discrete variables, Alice and Bob share two Bell states and perform unitary operations U_A and U_B, respectively. After the CNOT gate, measurement on their targeted qubits, and agreement using communication between them, the set of diagonal elements $\{p_a, p_b, p_c, p_d\}$ trans-

form to $\{p_A, p_B, p_C, p_D\}$ that are calculated by Eq. (6.7):

$$p_A = \frac{p_a^2 + p_b^2}{P}, \qquad p_B = \frac{2p_c p_d}{P}, \tag{6.15}$$

$$p_C = \frac{p_c^2 + p_d^2}{P}, \qquad p_D = \frac{2p_a p_b}{P}, \tag{6.16}$$

Consequently, the aim of the quantum privacy amplification for the GKP qubit is to improve the probability from p_a to $p_A = p_a^2/P$ after the quantum privacy amplification, where P is equal to $p_a^2 + p_b^2 + p_c^2 + p_d^2$.

For the next round of the protocol, we can calculate the set of diagonal elements $\{p_{A,2}, p_{B,2}, p_{C,2}, p_{D,2}\}$ as

$$p_{A,2} = \frac{p_A^2 + p_B^2}{P_2}, \qquad p_{B,2} = \frac{2p_C p_D}{P_2}, \tag{6.17}$$

$$p_{C,2} = \frac{p_C^2 + p_D^2}{P_2}, \qquad p_{D,2} = \frac{2p_A p_B}{P_2}, \tag{6.18}$$

respectively, where $P_2 = p_{A,2}^2 + p_{B,2}^2 + p_{C,2}^2 + p_{D,2}^2$. The set of diagonal elements for the nth-round of the protocol is recursively given by

$$p_{A,n} = \frac{p_{A,n-1}^2 + p_{B,n-1}^2}{P_n}, \tag{6.19}$$

$$p_{B,n} = \frac{2p_{C,n-1} p_{D,n-1}}{P_n}, \tag{6.20}$$

$$p_{C,n} = \frac{p_{C,n-1}^2 + p_{D,n-1}^2}{P_n}, \tag{6.21}$$

$$p_{D,n} = \frac{2p_{A,n-1} p_{B,n-1}}{P_n}, \tag{6.22}$$

respectively, where $P_n = p_{A,n-1}^2 + p_{B,n-1}^2 + p_{C,n-1}^2 + p_{D,n-1}^2$
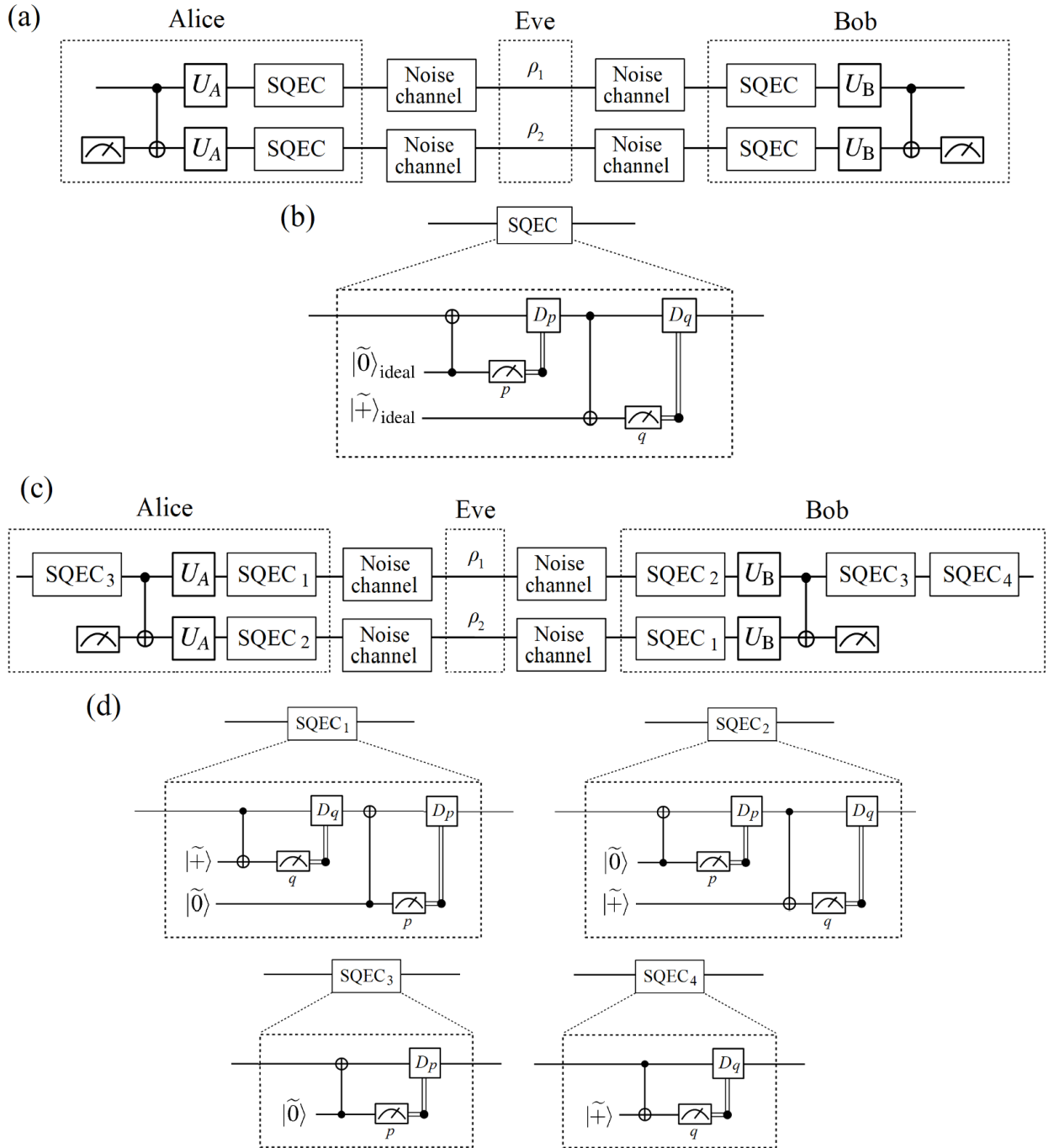
Figure 6.2: Introduction of a quantum privacy amplification with ideal GKP qubits (a) and approximate GKP qubits (c). The single-qubit level QEC (SQEC) is performed by the CNOT gate interacting between the qubit of thet Bell pair and ancilla qubit, and the feedforward (displacement) operation depending on the measurement outcome of the ancilla qubit. D_q and D_p represent the feedforward operations for the q and p quadratures, respectively.

6.1.3 Quantum privacy amplification with approximate GKP qubits

In the case of approximate GKP qubits, we need to consider the error probabilities derived from the initial finite squeezing level during the single-qubit level QEC, except for the Gaussian quantum channel. In the protocol with the approximate GKP qubits in Fig. 6.2 (c), Eve firstly prepares the GKP qubits with the variances (σ^2, σ^2) in the q and p quadratures, respectively. She, then, generates the Bell state by using the CNOT gate between the control qubit 2 and targeted qubit 1. After the CNOT gate, the variances of the qubit 1 and qubit 2 of the Bell state transform as

$$
\begin{pmatrix} \sigma^2 \\ \sigma^2 \end{pmatrix}_1 \rightarrow \begin{pmatrix} \sigma^2 \\ 2\sigma^2 \end{pmatrix}_1, \quad \begin{pmatrix} \sigma^2 \\ \sigma^2 \end{pmatrix}_2 \rightarrow \begin{pmatrix} 2\sigma^2 \\ \sigma^2 \end{pmatrix}_2. \tag{6.23}
$$

After the Gaussian quantum channel, Alice and Bob receive the Bell pair, where the variances of two GKP qubits are described as

$$
\begin{pmatrix} \sigma^2 \\ 2\sigma^2 \end{pmatrix}_1 \rightarrow \begin{pmatrix} \sigma^2 + \xi^2 \\ 2\sigma^2 + \xi^2 \end{pmatrix}_1, \tag{6.24}
$$

$$
\begin{pmatrix} 2\sigma^2 \\ \sigma^2 \end{pmatrix}_2 \rightarrow \begin{pmatrix} 2\sigma^2 + \xi^2 \\ \sigma^2 + \xi^2 \end{pmatrix}_2, \tag{6.25}
$$

respectively. Then, in the same way as the case of ideal GKP qubits $|\widetilde{\Psi}^+\rangle_{\text{ideal}}$, we consider the degradation affected by the Gaussian quantum channel and the single-qubit level QEC on the Bell state with the finite squeezing level, $|\widetilde{\Psi}^+\rangle$, as

$$
\begin{aligned}
|\widetilde{\Phi}^+\rangle\langle\widetilde{\Phi}^+| \;\rightarrow\; & p_{\text{a}}|\widetilde{\Phi}^+\rangle\langle\widetilde{\Phi}^+| + p_{\text{b}}|\widetilde{\Psi}^-\rangle\langle\widetilde{\Psi}^-| \\
& + \; p_{\text{c}}|\widetilde{\Psi}^+\rangle\langle\widetilde{\Psi}^+| + p_{\text{d}}|\widetilde{\Phi}^-\rangle\langle\widetilde{\Phi}^-|,
\end{aligned} \tag{6.26}
$$

where the p_{a}, p_{b}, p_{c}, and p_{d} are given by Eqs (6.10)-(6.12) up to replacing $E_{\sigma^2} \rightarrow E_{3\sigma^2+\xi^2}$. The probability $E_{3\sigma^2+\xi^2}$ with a noise level ξ^2 and the variance σ^2 is calculated by Eq. (6.13). We assumed that the variances of the ancilla qubits used for the single-qubit level QEC are σ^2 in the q and p quadratures, respectively. After the single-qubit lebel QEC as depicted as SQEC$_1$ and SQEC$_2$ in Fig.6.2 (c), Alice and Bob perform the CNOT gates on two noisy Bell states after unitary operations U_{A} and U_{B}, respectively.

After the CNOT gate, the variances of qubits 1, 2, 3, and 4 in the q and p quadratures transform as shown in Fig. 6.2 (c):

$$\begin{pmatrix} 2\sigma^2 \\ \sigma^2 \end{pmatrix}_1 \rightarrow \begin{pmatrix} 2\sigma^2 \\ 3\sigma^2 \end{pmatrix}_1, \quad \begin{pmatrix} \sigma^2 \\ 2\sigma^2 \end{pmatrix}_2 \rightarrow \begin{pmatrix} \sigma^2 \\ 3\sigma^2 \end{pmatrix}_2, \quad (6.27)$$

$$\begin{pmatrix} \sigma^2 \\ 2\sigma^2 \end{pmatrix}_3 \rightarrow \begin{pmatrix} 3\sigma^2 \\ 2\sigma^2 \end{pmatrix}_3, \quad \begin{pmatrix} 2\sigma^2 \\ \sigma^2 \end{pmatrix}_4 \rightarrow \begin{pmatrix} 3\sigma^2 \\ \sigma^2 \end{pmatrix}_4, \quad (6.28)$$

respectively. Then, they measure the target qubits (qubits 3 and 4) in the q quadrature. Unlike the case of ideal GKP qubits, there is the probability of the measurement error on the qubits with the variance $3\sigma^2$. If two measurement outcomes of the bit value coincide, they keep the control qubits (qubits 1 and 2) and perform the feedforward operation on control qubits depending on the measurement outcomes of target qubits, respectively. After the feedforward operation, the variances of the qubits 1 and 2 are described as

$$\begin{pmatrix} \sigma^2 \\ 3\sigma^2 \end{pmatrix}_1, \quad \begin{pmatrix} \sigma^2 \\ 3\sigma^2 \end{pmatrix}_2, \quad (6.29)$$

respectively. After agreement using communication between them, the set of diagonal elements $\{p_a, p_b, p_c, p_d\}$ transform to $\{p'_a, p'_b, p'_c, p'_d\}$ (up to normalization):

$$p'_a = \{(1 - E_{3\sigma^2})^2 + E_{3\sigma^2}^2\}(p_a^2 + p_b^2) + 2E_{3\sigma^2}(1 - E_{3\sigma^2})(p_a p_c + p_b p_d), \quad (6.30)$$

$$p'_b = 2\{(1 - E_{3\sigma^2})^2 + E_{3\sigma^2}^2\}p_c p_d + 2E_{3\sigma^2}(1 - E_{3\sigma^2})(p_b p_c + p_a p_d), \quad (6.31)$$

$$p'_c = \{(1 - E_{3\sigma^2})^2 + E_{3\sigma^2}^2\}(p_c^2 + p_d^2) + 2E_{3\sigma^2}(1 - E_{3\sigma^2})(p_a p_c + p_b p_d), \quad (6.32)$$

$$p'_d = 2\{(1 - E_{3\sigma^2})^2 + E_{3\sigma^2}^2\}p_a p_b + 2E_{3\sigma^2}(1 - E_{3\sigma^2})(p_a p_d + p_b p_c), \quad (6.33)$$

respectively. Then, to recover the variances to initial ones, Alice and Bob firstly perform the single-qubit level QECs depicted as $SQEC_3$ in Fig.6.2 (c). The variances of the qubits 1 and 2 transform as

$$\begin{pmatrix} \sigma^2 \\ 3\sigma^2 \end{pmatrix}_1 \rightarrow \begin{pmatrix} 2\sigma^2 \\ \sigma^2 \end{pmatrix}_1, \quad \begin{pmatrix} \sigma^2 \\ 3\sigma^2 \end{pmatrix}_2 \rightarrow \begin{pmatrix} 2\sigma^2 \\ \sigma^2 \end{pmatrix}_2, \quad (6.34)$$

respectively. The set of diagonal elements $\{p'_a, p'_b, p'_c, p'_d\}$ transform to $\{p''_a, p''_b, p''_c, p''_d\}$ (up to normalization):

$$
\begin{align}
p''_a &= \left\{(1-E_{4\sigma^2})^2 + E_{4\sigma^2}^2\right\}p'^2_a + 2E_{4\sigma^2}(1-E_{4\sigma^2})p'_d, \tag{6.35} \\
p''_b &= 2\left\{(1-E_{4\sigma^2})^2 + E_{4\sigma^2}^2\right\}p'_b + 2E_{4\sigma^2}(1-E_{4\sigma^2})p'_c, \tag{6.36} \\
p''_c &= \left\{(1-E_{4\sigma^2})^2 + E_{4\sigma^2}^2\right\}(p'^2_c + p'^2_d) + 2E_{4\sigma^2}(1-E_{4\sigma^2})p'_b, \tag{6.37} \\
p''_d &= 2\left\{(1-E_{4\sigma^2})^2 + E_{4\sigma^2}^2\right\}p'_d + 2E_{4\sigma^2}(1-E_{4\sigma^2})p'_a, \tag{6.38}
\end{align}
$$

respectively. Finally, one of Alice and Bob performs the single-qubit level QEC. Given Alice performs the single-qubit level QEC on her qubit 1 depicted as SQEC$_4$ in Fig. 6.2(c), the variance transforms as

$$
\begin{pmatrix} 2\sigma^2 \\ \sigma^2 \end{pmatrix}_1 \rightarrow \begin{pmatrix} \sigma^2 \\ 2\sigma^2 \end{pmatrix}_1. \tag{6.39}
$$

The set of diagonal elements $\{p''_a, p''_b, p''_c, p''_d\}$ transform to $\{p_A, p_B, p_C, p_D\}$ (up to normalization):

$$
\begin{align}
p_A &= (1-E_{3\sigma^2})p''^2_a + E_{3\sigma^2}p''_c, \tag{6.40} \\
p_B &= (1-E_{3\sigma^2})p''^2_b + E_{3\sigma^2}p''_d, \tag{6.41} \\
p_C &= (1-E_{3\sigma^2})p''^2_c + E_{3\sigma^2}p''_a, \tag{6.42} \\
p_D &= (1-E_{3\sigma^2})p''^2_d + E_{3\sigma^2}p''_b, \tag{6.43}
\end{align}
$$

respectively. Consequently, we can implement the quantum privacy amplification with approximate GKP qubits to improve the probability from p_a to p_A/P, where P is equal to $p_A + p_B + p_C + p_D$. For the next round of the protocol, we can calculate the set of diagonal elements $\{p_{A,2}, p_{B,2}, p_{C,2}, p_{D,2}\}$ by replacing $p_a \rightarrow p_A$, $p_b \rightarrow p_B$, $p_c \rightarrow p_C$, and $p_d \rightarrow p_D$ in Eq. (6.26). Similarly, the set of diagonal elements for the nth-round $\{p_{A,n}, p_{B,n}, p_{C,n}, p_{D,n}\}$ of the protocol is recursively calculated.
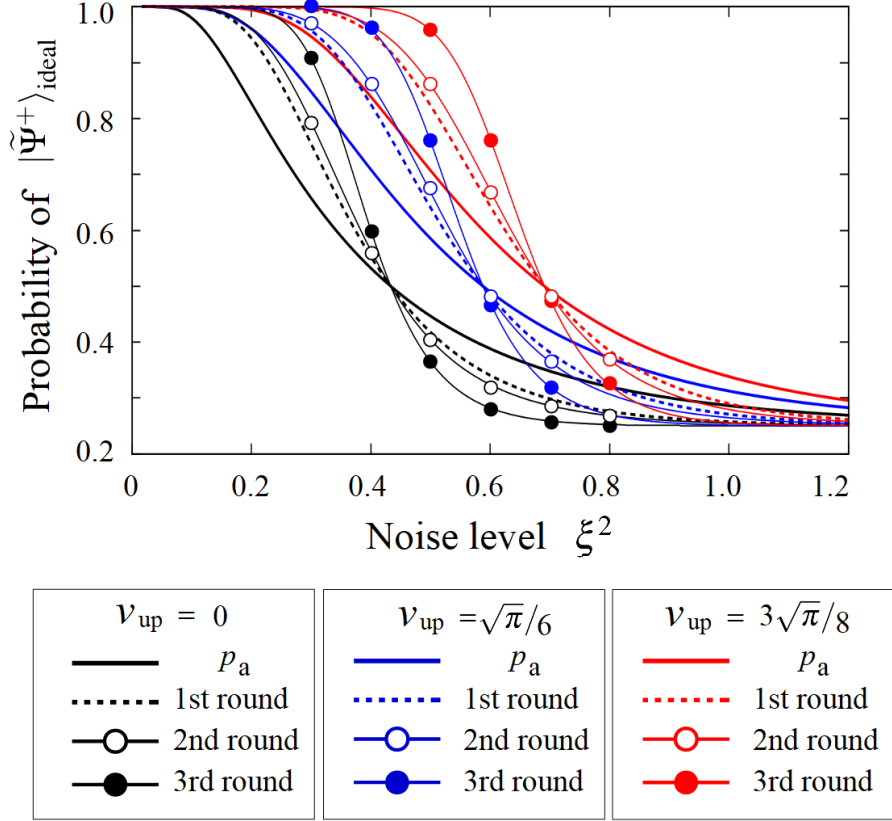
Figure 6.3: Numerical results for the probabilities p_a and p_A using the conventional and proposed methods with ideal GKP qubits. The probabilities are plotted as a function of a noise level ξ^2 of the Gaussian quantum channel for several upper limit $v_{up} = 0$ (black line), $\sqrt{\pi}/6$ (blue line), and $3\sqrt{\pi}/8$ (red line) for p_a (solid), p_A for 1st-round (dashed), $p_{A,2}$ for 2nd-round (open circles, and $p_{A,3}$ for 3rd-round (filled circles), respectively.

6.2 Proposed quantum privacy amplification using the highly-reliable measurement

In our method, we apply the highly-reliable measurement to the quantum privacy amplification protocol to improve the performance of the quantum privacy amplification at the cost of the success probability of the measurement. For the protocols with ideal and approximate GKP qubits, we can reduce the measurement error of the bit value by discarding when we obtain the amplitude of the measurement deviation value bounded by v_{up}. In the protocol with ideal GKP qubits described in Sec. 6.1.2, the highly-reliable measurement is utilized for the single-qubit level QEC to reduce the measurement error E_{ξ^2}. Accordingly, the probability p_A described in Eq. (6.15) increases by using the highly-reliable measurement. In the protocol with approximate GKP qubits described in

91

Sec. 6.1.3, the highly-reliable measurement is utilized to reduce the measurement error in the single-qubit level QEC, $E_{3\sigma^2+\xi^2}$, the measurement error of the qubits 3 and 4 after the CNOT gate, $E_{3\sigma^2}$, and the measurement error in the single-qubit level QEC on qubit 1 and 2, $E_{4\sigma^2}$ and $E_{3\sigma^2}$. Accordingly, the probability p_A described in Eq. (6.40) increases by using the highly-reliable measurement. In the next section, we will numerically show the improvement of the probabilities p_A. Strictly speaking, we might consider the correlated errors on the Bell pair in the case of approximate GKP qubits. This is because the displacement errors on the control and targeted qubits are propagated each other through the CNOT gate in the preparation of the Bell pair. As a result, this correlated errors prevent us from briefly describing the measurement error probabilities E_{σ^2}. However, as shown in Appendix for this chapter, we show that it is reasonable to ignore the effect of the correlated errors on a quantum privacy amplification with GKP qubits by using numerical calculations.

6.3 Numerical calculations

To confirm validity of our quantum privacy amplification protocol, we numerically calculate the error probabilities p_i ($i =$ a, b, c, d), p_j ($j =$ A, B, C, D), and $p_{j,n}$ for ideal and approximate GKP qubits. Then, we evaluate the performance of our method by comparing between p_a, p_A, and $p_{A,n}$ for the nth-round of the conventional method with that of the proposed method. We note that the quantum privacy amplification protocol works, if $p_{A,n}$ is greater than p_a in a noise level more than a threshold value. In Fig. 6.3, the error probabilities p_a and $p_{A,n}$ ($n = 2, 3$) using the conventional and proposed methods with ideal GKP qubits are plotted as a function of a variance of a noise level ξ^2 of the Gaussian quantum channel for several rounds for 1st-round (dashed), $p_{a,2}$ for 2nd-round (open circles), $p_{a,3}$ for 3rd-round 3 (filled circles). We assume that the squeezing levels of the GKP qubits used to prepare the Bell state and perform the single-qubit level QEC are 7 dB (a) 10 dB (b) 15 dB (c), and the upper limits v_{up} for the highly-reliable measurement are $v_{up} = 0$ (black line), $\sqrt{\pi}/6$ (blue line), and $3\sqrt{\pi}/8$ (red line). The results in Fig. 6.3 show that our method can improve the performance of the quantum privacy amplification with ideal GKP qubits, since the threshold values of a noise level are improved by using the highly-reliable measurement as v_{up} increases, where the threshold value with the conventional method is ~ 0.42. In Figs. 6.4(a), (b), and (c), the error probabilities using the

conventional and proposed methods with approximate GKP qubits are plotted. In the calculations, we assumed that the squeezing level of approximated GKP qubits prepared by Alice, Bob, and Eve is same. Fig. 6.4 show that our method improves the performance of the quantum privacy amplification with approximate GKP qubits, since the threshold values of a noise level are improved by our method. It is remarkable that our method works even with the initial squeezing level 7 dB as shown in Fig. 6.4 (a). Furthermore, a noteworthy fact in Fig. 6.4 (b) is that our method achieves the maximum probability (fidelity) $p_{\text{A},n} \sim 1.0$ by contrast with the conventional method that achieves the $p_{\text{A},n} \sim 0.88$.

6.4 Discussion and conclusion

In this work, we have presented analog-assisted quantum privacy amplification protocol with GKP qubits by using the highly-reliable measurement proposed that reduces the probability of misidentifying the bit value of the GKP qubit. We firstly have modeled a quantum privacy amplification protocol with ideal and approximate GKP qubits. Then, we applied the highly-reliable measurement to the protocol to improve the performance of the quantum privacy amplification protocol. The numerical results have showed that the proposed method has a great advantage in enhancing the performance of a quantum privacy amplification even with a very noisy channel, where the conventional method can not work. Hence, our method will bring up virtue of the highly-reliable measurements with continuous variables in quantum communication with continuous variables, and open up a promising avenue to quantum communication with continuous variables.
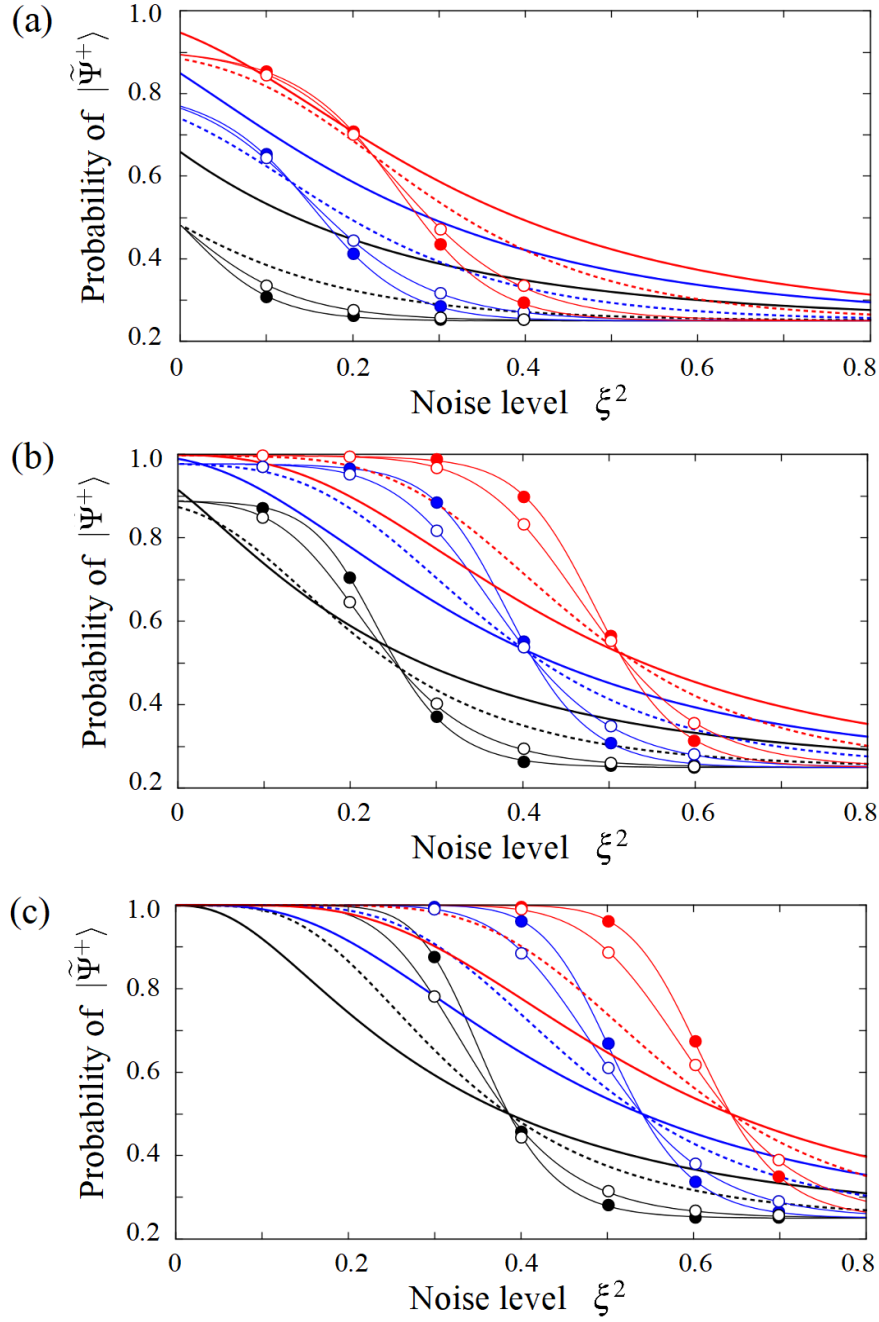
Figure 6.4: Numerical results for the probabilities p_a and p_A using the conventional and proposed methods with approximate GKP for the initial squeezing level of the single GKP qubit prepared, 7 dB (a) 10 dB (b) 15 dB (c). The probabilities are plotted as a function of a noise level ξ^2 of the Gaussian quantum channel for several upper limit $v_{up} = 0$ (black line), $\sqrt{\pi}/6$ (blue line), and $3\sqrt{\pi}/8$ (red line) for p_a (solid), p_A for 1st-round (dashed), $p_{A,2}$ for 2nd-round (open circles, and $p_{A,3}$ for 3rd-round (filled circles), respectively.

Appendix for Chap. 6: Effect of correlated errors

In Sec. 6.1.3, we explain the quantum privacy amplification protocol with approximate GKP qubits, ignoring the effect of the correlated error. In this appendix, we investigate the effect of the correlated error. In the case of approximate GKP qubits, the deviations of the control and targeted qubits are propagated between the two qubits through the CNOT gate. For example, we consider the preparation of the Bell pair by using the CNOT gate on the control qubit C and the targeted qubit T. The CNOT gate transforms the true deviation of two qubits in the q and p quadratures as

$$\overline{\Delta}_{q,\mathrm{C}} \;\rightarrow\; \overline{\Delta}'_{q,\mathrm{C}} = \overline{\Delta}_{q,\mathrm{C}}, \tag{A1}$$

$$\overline{\Delta}_{p,\mathrm{C}} \;\rightarrow\; \overline{\Delta}'_{p,\mathrm{C}} = \overline{\Delta}_{p,\mathrm{C}} - \overline{\Delta}_{p,\mathrm{T}}, \tag{A2}$$

$$\overline{\Delta}_{q,\mathrm{T}} \;\rightarrow\; \overline{\Delta}'_{q,\mathrm{T}} = \overline{\Delta}_{q,\mathrm{T}} + \overline{\Delta}_{q,\mathrm{C}}, \tag{A3}$$

$$\overline{\Delta}_{p,\mathrm{T}} \;\rightarrow\; \overline{\Delta}'_{p,\mathrm{T}} = \overline{\Delta}_{p,\mathrm{T}}, \tag{A4}$$

where $\overline{\Delta}_{q,\mathrm{C}}$ ($\overline{\Delta}_{p,\mathrm{C}}$) and $\overline{\Delta}_{q,\mathrm{T}}$ ($\overline{\Delta}_{p,\mathrm{T}}$) are the true deviation values of qubits C and T in the q and p quadratures, respectively. Assuming that the true deviations $\overline{\Delta}_{q,\mathrm{C}}$, $\overline{\Delta}_{p,\mathrm{C}}$, $\overline{\Delta}_{q,\mathrm{D}}$, and $\overline{\Delta}_{p,\mathrm{D}}$ obey the Gaussian distribution with the variance σ^2, the $\overline{\Delta}'_{p,\mathrm{C}}$ and $\overline{\Delta}'_{q,\mathrm{T}}$ obey the Gaussian distribution with the variance $2\sigma^2$. We here note that the two variables $\overline{\Delta}'_{q,\mathrm{C}}$ and $\overline{\Delta}'_{q,\mathrm{T}}$ have a particular correlation with each other, since the variable $\overline{\Delta}'_{q,\mathrm{T}}$ includes the variable $\overline{\Delta}'_{q,\mathrm{C}}$. Similarly, the two variables $\overline{\Delta}'_{p,\mathrm{C}}$ and $\overline{\Delta}'_{p,\mathrm{T}}$ have a correlation with each other. Hence, we can not describe independently each of the measurement error derived from $\overline{\Delta}'_{q,\mathrm{C}}$ and that derived from $\overline{\Delta}'_{q,\mathrm{T}}$. Accordingly, the correlated errors prevent us from briefly describing the probabilities p_{i} ($i = \mathrm{a,b,c,d,A,B,C,D}$) by using E_{σ^2}.

To investigate an effect of the correlated errors on the quantum privacy amplification protocol, we numerically simulate the probability p_{a} described in Eq.(6.26) by using Monte Carlo method. In the simulation, the Bell pair is prepared from the two qubits with the finite squeezing level, and the Gaussian quantum channel independently adds the deviation to the variables of the two qubits. In the single-qubit level QEC, ancilla qubits with the finite squeezing level are interacted with the qubits of the Bell pair, and measured. In Fig. 6.5, the error probabilities p_{a} for several squeezing level of initial GKP
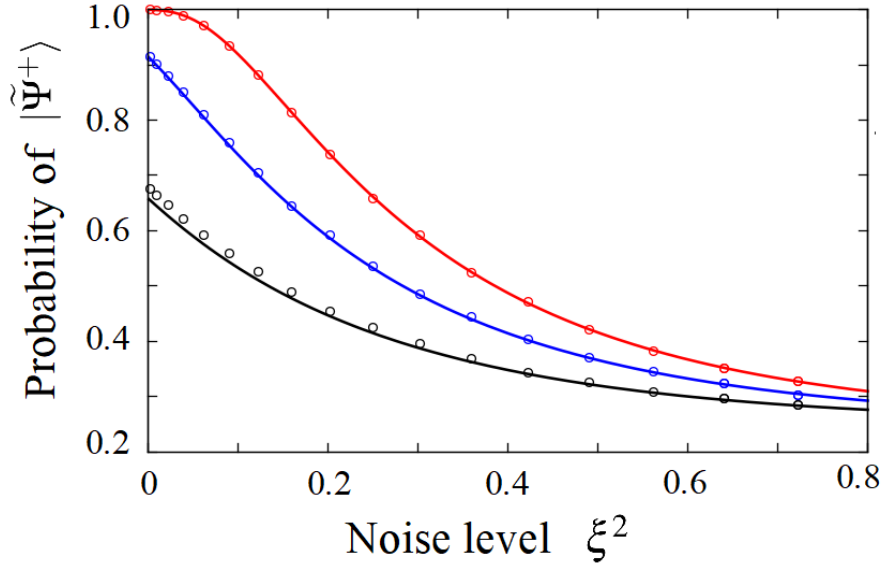
Figure 6.5: The effect of the correlated errors. The probabilities p_a are plotted as a function of a noise level ξ^2 of the Gaussian quantum channel for the initial squeezing level of the single GKP qubit 7 dB (black) (a) 10 dB (blue) (b) 15 dB (red) (c). The numerical results plotted as a solid line are calculated by Eq. (6.26), and open circles are simulated by using Monte-Carlo method.

qubits are plotted as a function of a noise level ξ^2 of the Gaussian quantum channel. Numerical results showed that the correlated error does not affect the probabilties p_a in a practical squeezing and a noise level, where the proposed method works well. Hence, we can ignore the correlated error in our numerical calculations.

Chapter 7

Quantum communication with the GKP qubits

Besides implementing continuous variable fault-tolerant quantum computation, the GKP qubits will be recognized as an important technological element to implement the continuous variable long-distance quantum communication, which is an important ingredient of the secure quantum internet [68] to implement secure communications [69, 70], distributed quantum cryptographic protocols, and so on. This is because the GKP qubit has a superb error tolerance against the disturbance of a noise channel, comparing with the other continuous variable code such as the cat code and the binomial code. In fact, we have shown that the GKP qubit can provide an optimal performance against the Gaussian quantum channel [6]. Furthermore, in Ref. [71], the GKP qubit can significantly outperform all other continuous variable codes, with respect to the bosonic pure-loss channel (i.e. photon loss channel) after the optimal recovery operation.

Toward long-distance quantum communication with continuous variables, a quantum repeater is indispensable element, where quantum repeaters between the sender Alice and the receiver Bob are needed to achieve the polynomial scaling of the efficiency with the total distance between Alice and Bob. In this chapter, we propose the method to implement resource-efficient quantum repeater protocol by harnessing analog information contained in the GKP qubit. In the proposed method, we apply the GKP qubit with the high-reliable measurement to "all photonic quantum repeater protocol" [72] in order to investigate the potential for quantum communication with the GKP qubit. Furthermore, we apply the analog QEC [6] to the encoded measurement to improve the performance of our protocol.

7.1 Quantum communication and quantum repeater

We briefly describe the concept of quantum communication. Quantum communication is a method to generate a secure network by transmitting either quantum or classical signals over distances using the quantum mechanics. Such a secure network enable us to implement cryptography, communication complexity, quantum bit-string commitment, large-scale distributed quantum computation, etc. One of the most advanced technological field using quantum communication is quantum key distribution (QKD). QKD establishes a secret key between the two distant parties named the sender Alice and the receiver Bob, where light pulses are generally transmitted through an optical fiber. A number of practical studies have already been demonstrated. If these parties are far beyond the attenuation length of the channel between parties, errors induced by the channel attenuation become a major barrier for efficient quantum communication over continental scales. In such a situation quantum repeaters are likely to be needed and work by dividing the long-distance link into a number of segments with a repeater at each station.

7.2 Idea of quantum repeater with with the GKP qubit using analog information

In this section, we briefly explain the quantum repeaters protocol with the highly-reliable measurement. Fig. 7.1 shows a schematic drawing of the proposed protocol, where there are four steps. In step 1, each of nodes prepares the "binding "cluster state (Fig. 7.1 (a)). The binding cluster state is composed of the leaf qubits and the encoded qubits, and is used to generate the entanglement between the neighboring repeaters. In this protocol, we assumed that the encoded qubit is encoded by varnava's code [73]which is used for "All photonic quantum repeaters" [72]. As an example, we here consider the binding cluster state with the ten leaf qubits. The binding cluster state is prepared by using the entanglement generation with the highly-reliable measurement described in chapter 4 (see also subsection 5.1.3).

7.3 Proposed quantum repeater protocol

In this section, we explain the method to implement quantum repeater protocol with the GKP qubit in detail, where analog information contained in the GKP qubit is utilized to improve the performance of quantum communication. Fig. 7.1 shows the schematic description of our protocol, consisting of Alice, Bob, the senders, and the repeaters. The proposed method consists of four steps. We will briefly describe each step of the proposed method in the following.

Step 1 Preparing and sending the encoded states

In step 1, firstly, each of nodes prepares the encoded cluster states composed by the GKP qubits, which is referred to as the "binding" cluster state in this work (Fig. 7.1 (a)). The binding cluster state is composed of the leaf qubits and the encoded qubits. To safely generate the entanglement between the neighboring repeaters, the binding cluster state is encoded by the Varnava's code [73], which has been used for "All photonic quantum repeaters" [72] based on photon qubits. As an example, we here consider the binding cluster state with the ten-leaf qubits (Fig. 7.1(a)). The binding cluster state is prepared using the fusion gate with the highly-reliable measurement to prevent decreasing in the squeezing level and reducing the probability of the misidentifying the bit value (see also Appendix A for the construction of the binding cluster). The reducing probability of the misidentification of the bit value leads to reduce the qubit-level error caused by the feedforward operation according to the outcome of the Bell measurement in the fusion gate.

Secondly, each of nodes sends the binding cluster state to neighboring repeaters as shown in Fig. 7.1 (b). After the transmission loss channel $\mathscr{L}$, the variances of the GKP qubit in the q and p quadrature decrease as depicted in Sec. 2. In this work, we assume that the GKP qubits suffer from the same amount of the photon loss channel $\mathscr{L}$ after the transmission.

Step 2 Fusion gate with the highly-reliable measurement on leaf qubits

In the step 2, each of repeaters receives the binding cluster states and implements the

fusion gate between the leaf qubits with the highly-reliable measurement to reduce the accumulation of the error as shown in Fig. 7.1(c). In the fusion gate, firstly, the 50:50 beam splitter transforms the variables in the q and p quadrature

$$\sqrt{\eta}\hat{q}_{ai} \rightarrow \sqrt{\eta/2}(\hat{q}_{ai} + \hat{p}_{bi}), \tag{7.1}$$

$$\sqrt{\eta}\hat{p}_{ai} \rightarrow \sqrt{\eta/2}(\hat{p}_{ai} + \hat{q}_{bi}), \tag{7.2}$$

$$\sqrt{\eta}\hat{q}_{bi} \rightarrow \sqrt{\eta/2}(\hat{q}_{ai} - \hat{p}_{bi}), \tag{7.3}$$

$$\sqrt{\eta}\hat{p}_{bi} \rightarrow \sqrt{\eta/2}(\hat{p}_{ai} - \hat{q}_{bi}), \tag{7.4}$$

where $\hat{q}_{ai}$ ($\hat{q}_{bi}$) and $\hat{p}_{ai}$ ($\hat{p}_{bi}$) the variables of the qubit $ai(bi)$ ($i = 1, 2, 3, 4, 5$) in the q and p quadrature, respectively (Fig. 7.1(c)).

Secondly, each of repeaters measures the leaf qubit ai and qubit bi in the p quadrature using homodyne detector. The measurement outcome of the leaf qubits $\sqrt{\eta/2}q_{mi}$ and $\sqrt{\eta/2}q_{mi}$ in the q and p quadrature are rescaled to q_{mi} and p_{mi} by multiplying the measurement outcome by $\sqrt{2/\eta}$ in a post-process, respectively. We here mention the transformation of the variances of the leaf qubits. After the coupling by the 50:50 beam splitter, the variances of the leaf qubits a_i and b_i in the q and p quadrature changes as

$$\sigma^2_{\text{out},qai} \rightarrow (\sigma^2_{\text{out},qai} + \sigma^2_{\text{out},pbi})/2, \tag{7.5}$$

$$\sigma^2_{\text{out},pai} \rightarrow (\sigma^2_{\text{out},pai} + \sigma^2_{\text{out},qbi})/2, \tag{7.6}$$

$$\sigma^2_{\text{out},qbi} \rightarrow (\sigma^2_{\text{out},qai} + \sigma^2_{\text{out},pbi})/2, \tag{7.7}$$

$$\sigma^2_{\text{out},pbi} \rightarrow (\sigma^2_{\text{out},pai} + \sigma^2_{\text{out},qbi})/2, \tag{7.8}$$

respectively. After the rescaling by multiplying the measurement outcome by $\sqrt{2/\eta}$ in a post-process, the variances transform

$$(\sigma^2_{\text{out},qai} + \sigma^2_{\text{out},pbi})/2 \rightarrow (\sigma^2_{\text{out},qai} + \sigma^2_{\text{out},pbi})/\eta, \tag{7.9}$$

$$(\sigma^2_{\text{out},pai} + \sigma^2_{\text{out},qbi})/2 \rightarrow (\sigma^2_{\text{out},pai} + \sigma^2_{\text{out},qbi})/\eta, \tag{7.10}$$

respectively.

Thirdly, each of repeaters applies the highly-reliable measurement to measurement outcome of the leaf qubits, and determines whether the highly-reliable measurement succeeds or not. In the highly-reliable measurement, if both the measurement deviations are

less than upper limit v_{up}, each of repeaters decides that the fusion gate with the highly-reliable measurement is succeeds. On the other hand, if both the measurement deviations are more than the upper limit v_{up}, or either of one of the two deviations is more than v_{up}, each of repeaters decides that the fusion gate with the highly-reliable measurement fails. By using the highly-reliable measurement, the qubit level error of misidentifying the bit value in p quadrature, which accumulates on the encoded qubit, can be reduced.

Step 3 Encoded measurement without the highly-reliable measurement

In step3, if the fusion gate with the highly-reliable measurement is succeeds, each of repeaters measures the encoded qubit, which is entangled with the successful leaf qubits, in the p quadrature to keep the entanglement between neighboring repeaters as shown in Fig. 7.1(d). In the encoded measurement in p quadrature, the error probability of misidentifying the bit value can be reduced by using the Varnava's code [73]. On the other hand, if the fusion gate with the highly-reliable measurement fails, each of repeaters measures the encoded qubit in the q quadrature to discard the entanglement as shown in Fig. 7.1(d). In the case of the failed fusion gate, the probability of misidentifying the bit value will be high, which occurs the qubit-level error on Alice and Bob after feedforward operation according to the measurement outcome. To reduce this qubit level error, the encoded measurement qubits are measured in the q quadrature (see also Appendix for Chap.7 C for the details of the measurement on the encoded qubits).

Step 4 Entanglement generation between Alice-Bob

In the last step of the proposed protocol, each of repeaters sends the measurement results to Alice and Bob. The number of the leaf qubits and the upper limit v_{up} need to be determined so that the entanglement between Alice and Bob generates almost deterministically. Then, Alice and Bob implement the feedforward operation according to the measurement results from all repeaters, and the entanglement between Alice and Bob is finally generated (Fig.7.1 (e)).
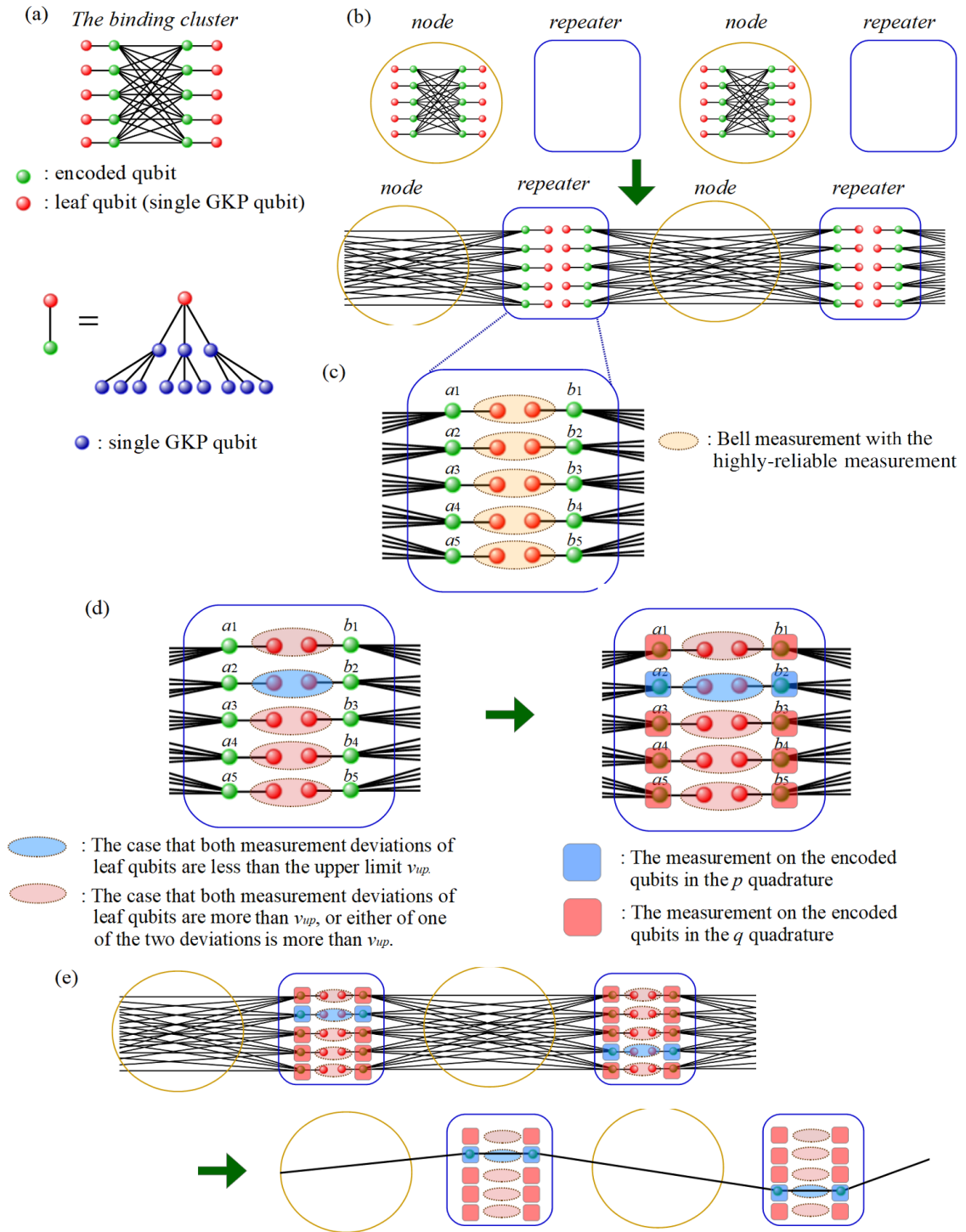
Figure 7.1: A schematic drawing of the GKP quantum repeater protocol with the highly-reliable measurement. (a) The "binding" cluster state. (b) Each of nodes sends the binding cluster state to neighboring repeaters. (c) The implementation of the fusion gate on the leaf qubits with the highly-reliable measurement. (d) The measurement on the encoded qubits. (e) The entanglement generation between the neighboring node, and Alice and Bob finally obtain the entanglement after feedforward operation.

102

7.4 Analysis

To evaluate the proposed protocol, we calculate the error probability in the q (p) quadrature, which is accumulated on the entanglement generated between Alice and Bob, E_{AB}^X (E_{AB}^Z). To obtain the E_{AB}^X (E_{AB}^Z), we calculate the average of the error probability in the p quadrature on each of repeaters,E_R^Z. The E_R^Z results from four causes, which correspond to the unheralded error originated from the unheralded errors during the construction of the binding cluster E_{Acc}, misidentifying the bit value of the leaf qubit with the highly-reliable measurement E_{PS}^{leaf}, the unheralded errors during the encoded measurement in the q quadrature E_{Enc}^X, and the unheralded errors during the encoded measurement in the p quadrature E_{Enc}^Z. The unheralded error E_{Acc} in the leading order is given by

$$E_{Acc} = 17 \times E_{\mathrm{PS}}(4\sigma^2) + 13 \times E_{\mathrm{PS}}(3\sigma^2), \tag{7.11}$$

where the unheralded error $E_{PS}(4\sigma^2)$ and $E_{PS}(3\sigma^2)$ are given by $P_{\mathrm{ps}}^{cor}/(P_{\mathrm{ps}}^{cor} + P_{\mathrm{ps}}^{in})$ with the variance in the p quadrature $4\sigma^2$ and $3\sigma^2$. The unheralded error E_{PS}^{leaf} occurs, when the fusion gate with the highly-reliable measurement fails. E_{PS}^{leaf} is given by E_{PS} with the variance

$$2(\sigma^2_{\mathrm{out},qai} + \sigma^2_{\mathrm{out},pbi})/\eta \tag{7.12}$$

described in Eq.(15). The unheralded error E_{Enc}^X occurs, when the encoded measurement encoded by the Varnava's code in the p quadrature fails. The unheralded errors E_{Enc}^X and E_{Enc}^Z are calculated by

$$\begin{aligned} E_{Enc}^X &= 3 \times (e_x + 3 \times e_z)^2, &(7.13)\\ E_{Enc}^Z &= 3 \times (3 \times e_x{}^2), &(7.14) \end{aligned}$$

where e_x and e_z are the probability of misidentifying the bit value of the GKP qubit with the variances σ_x^2 and σ_z^2, respectively. The probability e_x (e_z) is given by

$$e_{x(z)} = \int_{-\frac{\sqrt{\pi}}{2}}^{\frac{\sqrt{\pi}}{2}} dx \frac{1}{\sqrt{2\pi\sigma_{x(z)}^2}} \exp(-x^2/2\sigma_{x(z)}^2). \tag{7.15}$$
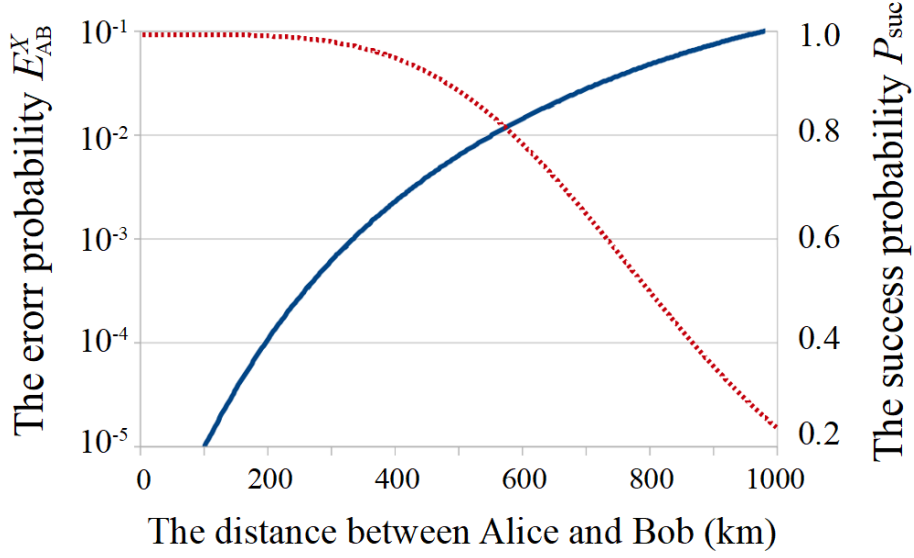
103

Figure 7.2: The probability of X and Z error. The probability E^X_{AB} (blue solid line) and the success probability of the entanglement generation between Alice and Bob P_{suc} (red dotted line) are plotted as a function of a distance between Alice and Bob L_{AB} for the binding cluster state with the ten laef qubits, the initial squeezing level 15 dB, and the number of repeaters 129.

Then, the error probability E^Z_R is calculated by

$$E^Z_R = E^{leaf}_{PS} + E_{Acc} + E^X_{Enc} + 4 \times E^Z_{Enc} \tag{7.16}$$

(see also Appendix for Chap. 7. B for the detailed calculation). Hence, the error probability E^X_{AB}, E^Z_{AB}, and E^Y_{AB} which occur on the entanglement between Alice and Bob is calculated as

$$E^X_{AB} = E^Z_{AB} = \frac{1}{4}\{1 - (1 - 2E_R)^{N_R/2}\}, \tag{7.17}$$

$$E^Y_{AB} = E^X_{AB} \times E^Z_{AB}, \tag{7.18}$$

where N_R is the number of repeaters.

To evaluate our method based on the GKP qubit, we compare our method with the method based on photon qubit such as Azuma $et\ al.$'s method [72]. In Fig. , the probability E^X_{AB} and the success probability of the entanglement generation between Alice and Bob P_{suc} are plotted as a function of a distance between Alice and Bob L_{AB} by using the binding cluster state with the ten laef qubits for the initial squeezing level 15 dB and the

number of repeaters 129. In this calculation, we assume that the variances of the initial single GKP qubit in q and p quadrature $\sigma^2 = \mathrm{e}^{-2r}/2$ in each of nodes has a variance, and the transmittance η is equal to $10^{-(l\times0.17)/10}$. L_{AB} is equal to $(2N_R+3)\times l$, where l is a distance between two neighboring repeaters. Numerical results showed that our method can achieve the value $(L_{\mathrm{AB}}, E_{AB}^X, P_{\mathrm{suc}}, N_{\mathrm{qubit}}) = (800$ km, 4.7%, 49%, $130)$ for the upper limit v_{up}=0.214 $\sqrt{\pi}$, where N_{qubit} is the number of photons prepared at each node for each blind cluster state, respectively. By contrast, Azuma *et al.*'s method achieve the value $(L_{\mathrm{AB}}, E_{AB}^X, P_{\mathrm{suc}}, N_{\mathrm{qubit}}) = (800$ km, 4.1%, 60%, $24{,}440)$. Therefore, our method can achieve the comparative performance with Azuma *et al.*'s method, and it is also remarkable that the number of the GKP qubits required for our method is several orders of magnitude less than the number of the photon qubits required for Azuma *et al.*'s method.

Furthermore, we apply the analog QEC [6] to the encoded measurement to improve the performance of our method (see also Appendix for Cap. 7. C for the explanation of the analog QEC for the Varnava's code). In this calculation, we numerically simulated the QEC for the Varnava's code using the Monte Carlo method. From the numerical calculation, we obtained the results that the analog QEC can reduce the E_{Enc}^X and E_{Enc}^Z by several orders of magnitude.

7.5 Discussion and conclusion

In this chapter, we propose the resource-efficient quantum repeater protocol toward long-distance quantum communication with the GKP qubits. Numerical results show that our method can achieve the comparative performance with the conventional methods based on photon qubits. Furthermore, our method can reduce the number of the GKP qubits required for quantum communication by several orders of magnitude less than the conventional method. In addition, we have obtained the results that our analog quantum error correction can improve the performance of our method. Furthermore, our method can be not limited to the GKP qubit but widely applicable to improve the performance of the quantum repeater protocols, which can incorporate with GKP qubit, cat code, and other various codes used to digitize continuous variable states. Hence, we believe the proposed method will open up a new approach to quantum repeater protocol with digitized continuous variable states, which will be indispensable to construct quantum communication with continuous variables.

Appendix for Chap. 7 A: Construction of the binding cluster

We apply the highly-reliable measurement to a large-cluster state construction to prevent the deviation of the GKP qubit from propagating during the entanglement generation, which can lead to preventing the squeezing level from decreasing during the construction of a large-cluster state. We explain how to apply the highly-reliable measurement to the construction of the binding cluster state composed of the ten leaf qubits as shown in Fig. 7.1 (a). In the proposed method, there are four steps. In step 1, we prepare the 3-tree cluster composed of a node qubit and two ancilla qubits by using the CZ gate (7.3. 5 (a)). The CZ gate, which corresponds to the operator $\exp(-i\hat{q}_C\hat{q}_T)$, transforms

$$\hat{q}_C \to \hat{q}_C, \ \hat{p}_C \to \hat{p}_C - \hat{q}_T \ , \tag{7.19}$$

$$\hat{q}_T \to \hat{q}_T, \ \hat{p}_T \to \hat{p}_T - \hat{q}_C, \tag{7.20}$$

where $\hat{q}_C$ ($\hat{q}_T$) and $\hat{p}_C$ ($\hat{p}_T$) are the q and p quadrature operators of the controlled (target) qubit, respectively. In terms of the deviation, we here consider the error propagation caused by the CZ gate operation. The CZ gate operation displaces the deviation for the q and p quadrature as

$$\overline{\Delta}_{q,C} \to \overline{\Delta}_{q,C}, \ \ \overline{\Delta}_{p,C} \to \overline{\Delta}_{p,C} - \overline{\Delta}_{q,T}, \tag{7.21}$$

$$\overline{\Delta}_{q,T} \to \overline{\Delta}_{q,T}, \ \ \overline{\Delta}_{p,T} \to \overline{\Delta}_{p,T} - \overline{\Delta}_{q,C}, \tag{7.22}$$

where $\overline{\Delta}_{q,C}$ ($\overline{\Delta}_{q,T}$) and $\overline{\Delta}_{p,C}$ ($\overline{\Delta}_{p,T}$) are true deviation values in the q and p quadrature of the controlled and target qubit, respectively. Since the true deviation is obeyed Gaussian distribution randomly and independently, the variance of the controlled qubit and target qubit in p quadrature changes as

$$\sigma_{p,C}^2 \to \sigma_{p,C}^2 + \sigma_{q,T}^2, \tag{7.23}$$

$$\sigma_{p,T}^2 \to \sigma_{p,T}^2 + \sigma_{q,C}^2, \tag{7.24}$$

where $\sigma_{q,C}^2$ ($\sigma_{q,T}^2$) and $\sigma_{p,C}^2$ ($\sigma_{p,T}^2$) are the variance of the controlled and target qubit in the q and p quadrature, respectively. On the other hand, the variance in the q quadrature does not change. Therefore, the CZ gate causes the increase in probability of misidentifying of

the bit value in p quadrature. For the 3-tree cluster state, the variance of the node qubit and the ancilla qubits in the p quadrature increase from σ^2 to $3\sigma^2$ and $2\sigma^2$ after the CZ gate, respectively. We assumed that the variance of the initial single GKP qubit is σ^2 in the q and p quadrature.

In step 2, we generate the 4-tree cluster state from the two 3-tree cluster states by using the Bell measurement on the ancilla qubit and the node qubit with the highly-reliable measurement (7.3 (b)). After the feedforward operation according to the Bell measurement outcome, the 4-tree cluster state is generated. This entanglement generation by using the Bell measurement can avoid the deviation of the qubit from propagating, and prevent the variances of the qubits from increasing. Moreover the highly-reliable measurement can reduce the measurement error which leads to bit level error on the node and ancilla qubits in the p quadrature after feedforward operation. We can obtain the 4-tree cluster state composed of the node qubits whose variance in the q and p quadrature are σ^2 and $3\sigma^2$, respectively. On the other hand, in conventional method, where the 4-tree cluster state is generated by using only the CZ gate, the variance and squeezing level of node qubits in the q and p quadrature are σ^2 and $4\sigma^2$, respectively. As a result, our method can prevent the squeezing level from decreasing. Hence, iteration of the entanglement generation by using the Bell measurement with the highly-reliable measurement offers a substantially lower error probabilities in constructing a large-cluster state. Following Ref. [52], in this note, we call this entanglement generation with the highly-reliable measurement as the fusion gate. Similarly, we generate the 5- and 6-tree cluster states as shown in Fig. 7.3 (c). The 5-tree cluster states is generated from the 3- and 4-tree cluster states. The 6-tree cluster states is generated from the two 4-tree cluster states.

In step 3, we generate the (3,3)-tree cluster state from the three 5-tree cluster states and the 6-tree cluster state as shown in Fig. 7.3 (d). Then, we generate the (5,3,3)-tree cluster state from the five (3,3)-tree cluster states and the 6-tree cluster state (Fig. 7.3 (e)). In step 4, we obtain the binding cluster state from the two (5,3,3)-tree cluster states as shown in Fig. 5 (f). After the construction of the binding cluster state, the variances of the node the q and p is σ^2 and $3\sigma^2$, respectively. Therefore, the fusion gate with highly-reliable measurement can avoid the degradation of the squeezing level during the construction of the binding cluster state. This can considerably reduce the measurement error probability. By contrast, the conventional method, where the fusion gate with the highly-reliable measurement is not used and the binding cluster state is generated by using only the CZ

gate, larger variance than proposal.

Appendix for Chap. 7 B: The encoded measurement

We describe the encoded measurement on the binding cluster in the q and p quadrature, which allow us to safely generate the entanglement. We explain the encoded measurement in the q quadrature to generate the entanglement between the nodes. Let $N_{\mathrm{A}i}$ be the set of qubits coneected to the qubit Ai. If we would like to reduce the error of misidentifying the bit value of qubit Ai, we implement a majority voting among the measurement outcomes from any qubit B$j \in N_{\mathrm{A}i}$. This is because the qubit Ai and Bj are stabilized by operator $\hat{Z}_{\mathrm{A}i}\,\hat{X}_{\mathrm{B}j}$. Hence, in the case of the binding cluster states as shown in Fig. 7.1(a), the encode measurement on the qubit Ai $(i = 1, 2, 3)$ is encoded by the three-qubit bit-flip code. Considering the three qubits A1, A2, and A3, the error probability E_{Enc}^{Z} is calculated by $E_{Enc}^{Z} = 3 \times (3 \times e_x{}^2)$. In the encoded measurement in the p quadrature, we implement the majority voting among the measurement outcomes from three logical qubits $\mathrm{A}_{\mathrm{L}i}$ $(i = 1, 2, 3)$. The measurement outcome of the logical qubit $\mathrm{A}_{\mathrm{L}i}$ is obtained by $X_{\mathrm{A}i}\prod_{\mathrm{B}j \in N_{\mathrm{A}i}} Z_{\mathrm{B}j}$ $(j = 1, 2, 3)$, where $X_{\mathrm{A}i}$ and $Z_{\mathrm{B}j}$ are the measurement outcomes of the qubit Ai and Bj in the p and q quadrature, respectively. Hence, the error probability E_{Enc}^{X} is calculated by $E_{Enc}^{X} = 3 \times (e_x + 3 \times e_z)$.

Appendix for Chap. 7 C: Analog quantum error correction for the Varnava's code

We briefly explain how to apply the analog QEC to the Varnava's code. As a simple example, we describe the encoded measurement in the q quadrature, where the encode measurement on the qubit Ai $(i = 1, 2, 3)$ is encoded by the three-qubit bit-flip code. Specifically, when we obtain the measurement outcome of the bit value $X_{\mathrm{B}j}$ and the deviation values $\Delta_{X_{\mathrm{B}j}}$ for the j-th physical GKP qubit $(j = 1, 2, 3)$, we implement a majority voting among the measurement outcomes $X_{\mathrm{B}j}$. If the result of a majority voting is ± 1, we

decide that the the encode measurement outcome on the qubit Ai is ± 1. Therefore, we can apply the analog QEC to the encode measurement to reduce the decision error of the encode measurement outcome (see also Ref. [6]). If the measurement outcomes of the physical GKP qubits X_{B1}, X_{B2}, and X_{B3} are $(1,0,0)$, then we consider two error patterns, considering that the outcomes without qubit-level error should be $(0,0,0)$ or $(1,1,1)$. The first pattern is a single error on the physical qubit B1 and the second pattern is the double errors on the physical qubits B2 and B3. We then calculate the likelihoods for the first F_1 and second pattern F_2 as

$$F_1 = f(\sqrt{\pi} - |\Delta_{X_{B1}}|)f(|\Delta_{X_{B2}}|)f(|\Delta_{X_{B3}}|), \tag{7.25}$$

$$F_2 = f(|\Delta_{X_{B1}}|)f(\sqrt{\pi} - |\Delta_{X_{B2}}|)f(\sqrt{\pi} - |\Delta_{X_{B3}}|), \tag{7.26}$$

respectively, where likelihood function $f(|\Delta_{X_{Bj}}|)$ is given by

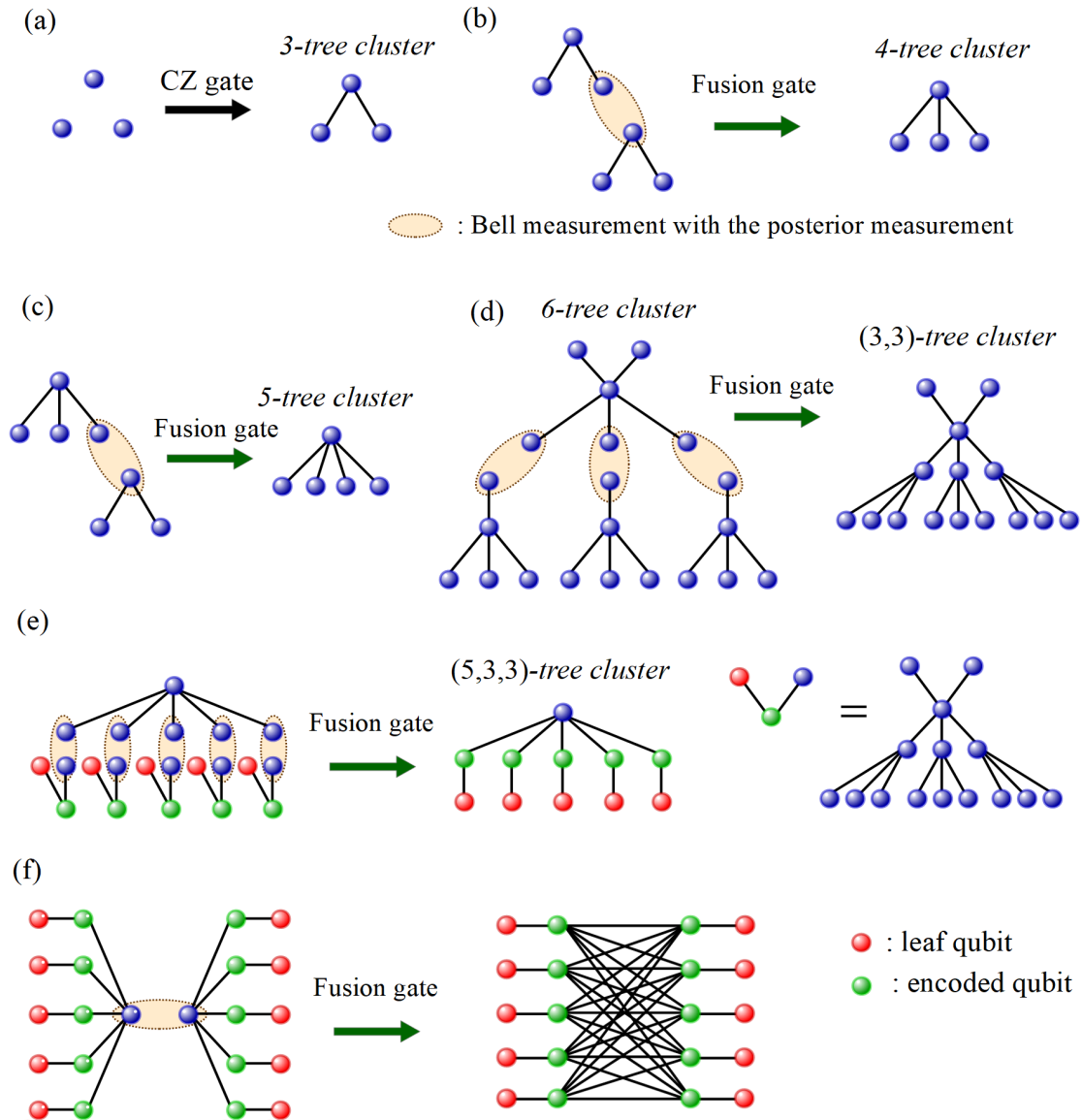$$f(|\Delta_{X_{Bj}}|) = \frac{1}{\sqrt{2\pi\sigma^2}}\exp(-|\Delta_{X_{Bj}}|^2/(2\sigma^2)). \tag{7.27}$$

Figure 7.3: The construction of the binding cluster state with the highly-reliable measurement. (a) The preparation of the 3-tree cluster state by using the CZ gate. (b) The generation of the 4-tree cluater state from the two 3-tree cluster states by using the Bell measurement with the highly-reliable measurement. (c) The construction of the 5-tree cluater state. (d) The construction of the (3,3)-tree cluater state. (e) The construction of the (5,3,3)-tree cluater state. (e) The construction of the binding cluster state.

Chapter 8

Summary and conclusions

In this thesis we have investigated fault-tolerant quantum computation, and quantum communication with GKP qubits. We have presented several methods to implement quantum computation and quantum communication that offer various novel and practical futures.

In Chap. 3, we have proposed the analog QEC and numerically demonstrated the improvement of QEC performance using the several quantum error correcting codes such as the three-qubit flip code, the Knill's C_4/C_6 code, a surface code. Numerical results have shown that the analog QEC with the C_4/C_6 code and a surface code provides an optimal performance against Gaussian quantum channel.

In Chap. 4, we have presented a method to implement large-scale quantum computation, which consists of two parts. One is to apply analog QEC [6] to a surface code. The other is a construction of the cluster state for the topologically protected measurement based quantum computation [9, 10, 11, 12] with a low error accumulation. By achieving the requirement of the squeezing level around 10 dB, the proposed method can considerably take a step closer to the realization of large-scale quantum computation.

In Chap. 5, to reduce the number of qubits required for the QEC during large-scale quantum computation, the tracking QEC has been presented, where the logical-qubit level QEC is partially substituted with the single-qubit level QEC.

In Chap. 6, to improve the entanglement distillation performance, we have proposed the entanglement distillation protocol with the GKP qubit using highly-reliable measurement. In the proposed method, we have applied the highly-reliable measurement to a quantum privacy amplification protocol with the ideal and approximate GKP qubit.

In Chap. 7, we have presented a method to implement a long-distance and resource-efficient quantum communication with GKP qubits. In the proposed method, the highly-reliable measurement has been used to enhance tolerance against photon loss through an optical fiber.

These presented methods offer the way of secure and high-fidelity quantum compu-

tation and quantum communication. Although the technologies required to build a large-scale quantum computer remain daunting, the proposed methods are motivation enough for researchers in the world to to focus resources into funding the technologies to realize large-scale quantum computation and long-distance quantum communication.

Bibliography

[1] P. W. Shor. SIAM J. Comp. **26**, 1484 (1997) .

[2] L. K. Grover. Phys. Rev. Lett. **79**, 325 (1997).

[3] J. Yoshikawa, S. Yokoyama, T. Kaji, C. Sornphiphatphong, Y. Shiozawa, K. Makino, and A. Furusawa. APLPhotonics **1** 060801 (2016) .

[4] N. C. Menicucci. Phys. Rev. Lett. **112**, 120504 (2014) .

[5] D. Gottesman, A. Kitaev, and J. Preskill. Phys. Rev. A **64**, 012310 (2001).

[6] K. Fukui, A. Tomita, and A. Okamoto. Phys. Rev. Lett. 119, 180507 (2017).

[7] K. Fukui, A. Tomita, A. Okamoto, and K. Fujii. Phys. Rev. X. **8**, 021054 (2018).

[8] K. Fukui, A. Tomita, and A. Okamoto. ArXiv e-prints arXiv:1804.04509 .

[9] A. Y. Kitaev. Ann. Phys. **303**, 2 (2003).

[10] R. Raussendorf and J. Harrington. Phys. Rev. Lett. **98**, 190504 (2007) .

[11] R. Raussendorf, J. Harrington, and K. Goyal. New J. Phys. **9**, 199 (2007) .

[12] R. Raussendorf, J. Harrington, and K. Goyal. *A fault-tolerant one-way quantum computer,* Annals of Physics **321**, 2242 (2006) .

[13] D. Gottesman. quant-ph/9807006 (1998).

[14] D. Gottesman. Ph.D. thesis, California Institute of Technology (1997).

[15] A. Y. Kitaev. Russ. Math. Surv. **52**, 1191 (1997) .

[16] J. Harrington and J. Preskill. Phys. Rev. A **64**, 062301 (2001).

[17] E. Knill, R. Laflamme, and W. H. Zurek. Proc. R. Soc. A **454**, 365 (1998) .

[18] J. Preskill. Proc. R. Soc. A **454**, 385 (1998).

[19] E. Knill. Nature, **434**, 39-44 (2005) .

[20] K. Fujii and K. Yamamoto. Phys. Rev. A **82**, 060301 (2010) .

[21] K. Fujii and K. Yamamoto. Phys. Rev. A **81**, 042324 (2010) .

[22] D. Poulin. Phys. Rev. A **74**, 052333 (2006) .

[23] H. Goto and H. Uchikawa. Sci. Rep. **3**, 2044 (2013 .

[24] J. Edmonds. Canadian Journal of mathematics **17**, 449 (1965).

[25] V. Kolmogorov. Mathematical Programming Computation**1**, 43 (2009) .

[26] K. Fujii and Y. Tokunaga. Phys. Rev. A **86**, 020303(R) (2010) .

[27] C. Wang, J. Harrington, and J. Preskill. Ann. Phys. **303**, 31 (2003) .

[28] K. Fujii and M. Hayashi. Phys. Rev. A **96**, 030301(R) (2017) .

[29] K. Fujii. *Quantum Computation with Topological Codes: From Qubit to Topological Fault-Tolerance*, Springer Briefs in Mathematical Physics Vol. 8 (Springer, Berlin, 2015) .

[30] T. Kailath. IEEE Transactions on Automatic Control, vol. 13, **6**, 646-655, (1968) .

[31] B. D'Anjou and W. A. Coish. Phys. Rev. Lett. **113**, 230402 (2014).

[32] B. D'Anjou, L. Kuret, L. Childress, and W. A. Coish. Phys. Rev. X **6**, 011017 (2016).

[33] H. Bombin and M. A. Mrtin-Delgado. Phys. Rev. Lett. **97**, 180501 (2006).

[34] A. M. Steane. Phys. Rev. Lett. **77**, 793 (1996) .

[35] D. Bacon. Phys. Rev. A **73**, 012340 (2006).

[36] H. M. Vasconcelos, L. Sanz, and S. Glancy. Opt. Lett. **35**, 3261 (2010).

[37] B. M. Terhal and D. Weigand. Phys. Rev. A **93**, 012315 (2016).

[38] K. R. Motes, B. Q. Baragiola, A. Gilchrist, and N. C. Menicucci. Phys. Rev. A **95**, 053819 (2017) .

[39] B. C. Travaglione and G. J. Milburn. Phys. Rev. A **66**, 052322 (2002) .

[40] P. Brooks, A. Kitaev, and J. Preskill. Phys. Rev. A **87**, 052306 (2013) .

[41] S. Pirandola, S. Mancini, D. Vitali, and P. Tombesi. Eur. Phys. J. D **37**, 283-290 (2006) .

[42] R. Barends, J. Kelly, A. Megrant, A. Veitia, D. Sank, E. Jeffrey, T. C. White, J. Mutus, A. G. Fowler, B. Campbell, Y. Chen, Z. Chen, B. Chiaro, A. Dunsworth, C. Neill, P. O'Malley, P. Roushan, A. Vainsencher, J. Wenner, A. N. Korotkov, A. N. Cleland, and J. M. Martinis. Nature **508**, 500-503 (2014).

[43] H. Vahlbruch, M. Mehmet, K. Danzmann, and R. Schnabel. Phys. Rev. Lett **117**, 110801 (2016) .

[44] N. C. Menicucci, X. Ma, and T. C. Ralph. Phys. Rev. Lett. **104**, 250503 (2010) .

[45] N. C. Menicucci. Phys. Rev. A **84**, 062314 (2011) .

[46] M. Ohliger, K. Kieling, and J. Eisert. Phys. Rev. A **82**, 042336 (2010).

[47] M. Ohliger and J. Eisert. Phys. Rev. A **85**, 062318 (2012) .

[48] N. C. Menicucci, P. van Loock, M. Gu, C. Weedbrook, T. C. Ralph, and M. A. Nielsen. Phys. Rev. Lett. **97**, 110501 (2006).

[49] S. Takeda and A. Furusawa. Phys. Rev. Lett. **119**, 120504 (2017).

[50] R. N. Alexander, S. Yokoyama, A. Furusawa, and N. C. Menicucci. arXiv: 1711.08782 (2017).

[51] M. A. Castellanos-Beltran, K. D. Irwin, G. C. Hilton, L. R. Vale, and K. W. Lehnert. Nat. Physics **4**, 929-931 (2008) .

[52] D. E. Brown and T. Rudolph. Phys. Rev. Lett. **95**, 01501 (2005) .

[53] M. A. Nielsen. Phys. Rev. Lett. **93**, 040503 (2004) .

[54] C. M. Dawson, H. L. Haselgrove, and M. A. Nielsen. Phys. Rev. Lett. **96**, 020501 (2006) .

[55] S. Glancy and E. Knill. Phys. Rev. A **73**, 012325 (2006) .

[56] A. M. Steane. Phys. Rev. Lett. **78**, 2252 (1997) .

[57] T. Ohno, G. Arakawa, I. Ichinose, and T. Matsui. Nucl.Phys. B**697**, 462 (2004).

[58] D. J. Weigand and B. M. Terhal. arXiv: 1709.08580 (2017) .

[59] M.Gimeno-Segovia, P. Shadbolt, D. E. Browne, and T. Rudolph. Phys. Rev. Lett. **115**, 020502 (2015) .

[60] Y. Li, P. C. Humphreys, G. J. Mendoza, and S. C. Benjamin. Phys. Rev. X **5**, 041007 (2015) .

[61] K. Fujii and Y. Tokunaga. Phys. Rev. Lett. **105**, 250503 (2010).

[62] S. J. Devitt, A. G. Fowler, A. M. Stephens, A. D. Greentree, L. C. Hollenberg, W. J. Munro, and K. Nemoto. New J. Phys. **11** 083032 (2009).

[63] N. C. Jones, R. V. Meter, A. G. Fowler, P. L. McMahon, J. Kim, T. D. Ladd, and Y. Yamamoto. Phys. Rev. X **2**, 031007 (2012).

[64] R.W. Heeres, P. Reinhold, N. Ofek, L. Frunzio, L. Jiang, M. Devoret, and R. Schoelkopf. Nature Communications, **8** , 94 (2017).

[65] C. Shen, K. Noh, V. V. Albert, S. Krastanov, M. H. Devoret, R. J. Schoelkopf, S. M. Girvin, and L. Jiang. Phy. Rev. B **95**, 134501 (2017).

[66] L. Li, C. L. Zou, V. V. Albert, S. Muralidharan, S. M. Girvin, and L. Jiang. Phys. Rev. Lett. **119**, 030502 (2017).

[67] D. Deutsch, A. Ekert, R. Jozsa, C. Macchiavello, S. Popescu, and A. Sanpera. Phys. Rev. Lett. **77**, 2818 (1998) .

[68] H. J. Kimble. Nature **453**, 1023 (2008).

[69] C. H. Bennett and G. Brassard. in *Proceeding of the IEEE International Conference on Computers, Systems,and Signal Processing, Bangalore, India* 175-179 (IEEE,New York, 1984).

[70] A. K. Ekert. Phys. Rev. Lett. **67**, 661 (1991).

[71] V. V. Albert, K. Noh, K. Duivenvoorden, R. T. Brierley, P. Reinhold, C. Vuillot, L. Li, C. Shen, S. M. Girvin, B. M. Terhal, and L. Jiang. arXiv: 1708.05010 (2017) .

[72] K. Azuma, K. Tamaki, and H-K. Lo. Nat.Commu. **6**, 6787 (2015).

[73] M. Varnava, D. E. Browne, and T. Rudolph. Phys. Rev. Lett. **97**, 120501 (2006).